

UC Berkeley

UC Berkeley Electronic Theses and Dissertations

Title

Advancing Electrophoretic Assays for Protein Analysis through Mass Spectrometry Imaging, Microfluidic Methods, and Hydrogel Engineering

Permalink

<https://escholarship.org/uc/item/0x45h9mt>

Author

Lomeli, Gabriela

Publication Date

2023

Peer reviewed|Thesis/dissertation

Advancing Electrophoretic Assays for Protein Analysis through Mass Spectrometry
Imaging, Microfluidic Methods, and Hydrogel Engineering

by

Gabriela Lomeli

A dissertation submitted in partial satisfaction of the

requirements for the degree of

Joint Doctor of Philosophy
with the University of California, San Francisco

in

Bioengineering

in the

Graduate Division

of the

University of California, Berkeley

Committee in charge:

Professor Amy E. Herr, Chair
Professor Gerard Marriott
Professor Bo Huang

Summer 2023

Advancing Electrophoretic Assays for Protein Analysis through Mass Spectrometry
Imaging, Microfluidic Methods, and Hydrogel Engineering

Copyright 2023
by
Gabriela Lomeli

Abstract

Advancing Electrophoretic Assays for Protein Analysis through Mass Spectrometry
Imaging, Microfluidic Methods, and Hydrogel Engineering

by

Gabriela Lomeli

Joint Doctor of Philosophy
with the University of California, San Francisco in Bioengineering

University of California, Berkeley

Professor Amy E. Herr, Chair

Proteoforms, highly related proteins, play critical roles in disease processes such as cancer. However, studying proteoforms is challenging due to their high homology and low abundance. Electrophoretic assays are capable of elucidating proteoforms, which are often indistinguishable with canonical antibody-based protein assays and mass spectrometry. This dissertation presents advancements in microfluidic, material, and mass spectrometry imaging approaches towards improved multiplexing, proteoform specificity, and sensitivity of electrophoretic assays.

First, the integration of mass spectrometry imaging and proteoform separation tools paves the way for highly multiplexed single-cell proteomics. Single-cell immunoblotting (scIB) offers proteoform detection specificity but often relies on fluorescence-based readout, limiting its multiplexing capability. Among the rising multiplexed imaging methods is multiplexed ion beam imaging by time-of-flight (MIBI-TOF), a mass spectrometry imaging technology. MIBI-TOF employs metal-tagged antibodies that do not suffer from spectral overlap to the same degree as fluorophore-tagged antibodies. We report for the first time MIBI-TOF of single-cell immunoblotting (scIB-MIBI-TOF). The scIB assay subjects single-cell lysate to protein immunoblotting on a microscale device consisting of a 50- to 75- μm thick hydrated polyacrylamide (PA) gel matrix for protein immobilization before in-gel immunoprobng. We confirm antibody-protein binding in the PA gel with indirect fluorescence readout of metal-tagged antibodies. Since MIBI-TOF is a layer-by-layer imaging technique, and our protein target is immobilized within a 3D PA gel layer, we characterize the protein distribution throughout the PA gel depth by fluorescence confocal microscopy and confirm that the highest signal-to-noise ratio is achieved by imaging the entirety of the PA gel depth. Accordingly, we report the required MIBI-TOF ion dose strength needed to image varying PA gel depths. Lastly, by imaging 42% of the PA gel depth with MIBI-TOF, we detect two

isoelectrically separated TurboGFP (tGFP) proteoforms from individual glioblastoma cells, demonstrating that highly multiplexed mass spectrometry-based readout is compatible with scIB.

Next, a polydimethylsiloxane (PDMS)-based device miniaturizes the isoelectric focusing (IEF) assay, enabling the specific measurement of proteoforms on a chip the size of a microscope slide. Microfluidic IEF assays have made it possible to assay proteoforms from low starting cell numbers, yet these often rely on carrier ampholytes (CAs) to establish a pH gradient for protein separation, and CAs have major limitations, including lack of pH gradient tunability and stability. Immobilized pH gradient (IPG) gels have been developed to overcome these limitations, but efforts to implement IPGs at the microscale have been limited to difficult-to-manufacture glass devices and require proteins to be labeled before analysis, precluding complex samples such as cell lysate. Here, we introduce the first PDMS-based IPG microfluidic device (μ IPG). First, we establish a pH gradient by introducing acidic and basic gel precursors at two reservoirs flanking a separation channel and allow diffusion to establish a linear pH gradient within the separation channel. We introduce a 2-step photopolymerization procedure to create a composite gel with two functions: 1) IEF protein separation via the IPG gel component, and 2) protein capture for downstream immunoprobing via a photoactive gel component. Therefore, μ IPG is suitable for the analysis of unlabeled, complex samples, which we demonstrate by immunoprobing green fluorescent protein (GFP) from GFP-expressing breast cancer cells. Moreover, we show that the pH gradient in the PDMS-based μ IPG is stable for at least 30 minutes, and we are able to resolve proteoforms differing by about 0.1 isoelectric point.

Furthermore, we continue developing gradient hydrogel technology to engineer a pore-size gradient gel for single-cell 3D projection electrophoresis. Single-cell 3D projection electrophoresis was developed by our group to increase throughput over planar (2D) single-cell western blotting and to provide the option to preserve spatial context in the analysis of intact tissue. However, it can be difficult to achieve adequate protein separation in the short separation distance (1 mm) employed by 3D projection electrophoresis. Conventional western blots have employed a gradient pore size in the axis of separation to improve separation efficiency. We describe the development of a gel slab for 3D projection electrophoresis with a gradient pore-size in the z-direction (axis of separation).

Lastly, an enclosed single-cell electrophoretic assay for native electrophoresis is developed. Single-cell electrophoresis (scEP) is a powerful method for separating proteoforms based on size and charge within individual cells. However, the current implementation of scEP is limited to open microfluidic devices, which precludes its integration with enclosed microfluidic formats (e.g., for microchannel electrophoresis), which could introduce additional performance improvements and separation modalities to scEP. We present an enclosed microfluidic scEP device that combines hydrodynamic cell trapping, electrical lysis, and protein electrophoresis for the first time. The device incorporates a PDMS-hydrogel hydrodynamic cell trapping component that also functions as an electrical lysis component. With electrical

cell lysis, rapid (<1 second) and non-denaturing lysis of proteins is achieved, preserving their native state during both lysis and electrophoresis. The microfluidic scEP device we introduce here demonstrates the feasibility and challenges of employing an enclosed microfluidic design for scEP.

By integrating diverse electrophoretic and mass spectrometry imaging tools in a miniaturized format, this dissertation expands the toolkit for proteoform analysis.

Para mi familia.

Contents

Contents	ii
List of Figures	iv
List of Tables	vi
1 Introduction	1
1.1 Role of heterogeneity at the molecular and cellular level	1
1.2 Overview of state-of-the-art in single-cell proteomics	2
1.3 Single-cell electrophoretic assays	3
1.4 Isoelectric focusing	7
1.5 Multiplexed ion beam imaging	9
1.6 Dissertation overview	10
References	11
2 Multiplexed Ion Beam Imaging Readout of Single-Cell Immunoblotting	15
2.1 Abstract	15
2.2 Introduction	16
2.3 Materials and Methods	18
2.4 Results and Discussion	21
2.5 Conclusions	31
References	32
3 Detecting Proteoforms using Isoelectric Focusing in On-Chip Immobilized pH Gradient Gels	34
3.1 Abstract	34
3.2 Introduction	35
3.3 Materials and Methods	37
3.4 Results and Discussion	42
3.5 Conclusions	53
References	54
4 Towards Pore-Size Gradient Gels for Projection Electrophoresis	57

4.1	Abstract	57
4.2	Introduction	57
4.3	Materials and Methods	58
4.4	Results and Discussion	61
4.5	Conclusions	67
	References	71
5	Combining Hydrodynamic Trapping and Electrical Lysis for Single-Cell Electrophoresis	72
5.1	Abstract	72
5.2	Introduction	72
5.3	Materials and Methods	74
5.4	Results and Discussion	78
5.5	Conclusions	90
	References	91
6	Conclusions and Future Directions	94
	References	95

List of Figures

1.1	Schematic of the heterogeneity present at the molecular and cellular level. . . .	2
2.1	scIB-MIBI-TOF combines single-cell protein separation assays with multiplexed mass spectrometry detection.	22
2.2	Metal-tagged antibody performance in scWB and scIEF.	23
2.3	Background signal for metal-tagged antibodies.	25
2.4	Protein signal is concentrated toward the bottom of the PA gel in scIB.	26
2.5	PA gel on glass slide is dehydrated before MIBI-TOF.	28
2.6	PA gel depth rasterized can be tuned by modulating ion dose.	29
2.7	MIBI-TOF of scIEF resolves tGFP proteoforms from single cells.	30
3.1	μ IPG device enables separation of proteoforms by isoelectric point.	35
3.2	Both UV irradiation and the benzophenone coating are necessary for PA gel polymerization in the PDMS device.	43
3.3	Concept and fabrication of the μ IPG device.	45
3.4	IEF of pI markers in μ IPG device confirms a linear pH gradient.	46
3.5	Anodic and cathodic drift is eliminated in μ IPG device.	48
3.6	μ IPG device resolves GFP proteoforms from MCF7 cell lysate.	49
3.7	Delamination of PDMS from glass to expose μ IPG for immunoprobng.	51
3.8	Immunoprobng μ IPG device.	52
4.1	Proposed workflow for using pore-size gradient gel for high-throughput single-cell projection electrophoresis.	59
4.2	Fluorescence intensity profile of rhodamine B as an indicator of gel density does not yield quantifiable results.	62
4.3	FITC and rhodamine B do not exhibit spectral overlap.	63
4.4	Example of how ratiometric imaging improves the quality of intensity image alone for a more quantitative assessment of pore-size (proportional to %T).	65
4.5	“Sandwich” method for creating z-direction pore-size gradient gels.	67
4.6	Oxygen-inhibited polymerization facilitates pore-size patterning.	68
4.7	Use of oxygen to modulate polymerization efficiency to create oxygen gradient-driven pore-size gradient gel.	70

5.1	Overview of enclosed single-cell electrophoresis device design.	75
5.2	Overview of microfluidic device fabrication.	76
5.3	DDevice combines hydrodynamic trapping and electrical lysis for single-cell protein electrophoresis.	79
5.4	Simulation of hydrodynamic cell trapping.	82
5.5	Experimental results of hydrodynamic trapping.	83
5.6	Simulation of electric field in cell trapping region and microchannels.	86
5.7	Variability in electrical cell lysis behavior in hydrodynamic cell traps.	89
5.8	Time lapse of electrical lysis and electrophoresis after hydrodynamic trapping of GFP-expressing MCF7 cell.	90

List of Tables

2.1	Composition of IEF lid gel.	20
2.2	Imaging conditions and depth rasterized data.	29
3.1	Recipes of PA gel precursors.	39
3.2	Anode inlet and cathode inlet sample components for all isoelectric focusing experiments.	41
4.1	Recipes for the various gel conditions.	60
5.1	R_{flow} obtained for the first cell trap for various geometries.	81

Acknowledgments

Picking a doctoral program can be a challenging decision for many, and I was no exception. To help me make the choice, I decided to call Prof. Amy Herr, whom I had previously had an informational Skype call with even before I'd decided to apply to the UC Berkeley-UCSF Program in Bioengineering. As I spoke to Amy on the phone, it dawned on me that she was the professor I trusted most to provide objective advice out of all the professors I'd met during graduate school visits. Perhaps that could be a clue as to which institution I should select. In January 2019, I joined Amy's group, and I am immensely grateful for the opportunity to work with her. She inspired me daily to pursue world-class research with the utmost integrity and dedication. For a Ph.D. filled with unprecedented times, thank you, Amy, for being an unprecedented leader.

I was extremely fortunate to receive guidance from professors across three Bay Area universities. Thank you to my dissertation committee members, Prof. Bo Huang from UCSF and Prof. Gerard Marriott from UC Berkeley, as well as Prof. Phillip Messersmith and Prof. Steve Connolly from my qualifying exam committee. An additional thank you is warranted for Prof. Connolly for going above and beyond in his role as Head Graduate Adviser. You taught me so much about resiliency, radical empathy, and compromise. Thank you to my collaborators at Stanford University, Prof. Mike Angelo, Prof. Sean Bendall, and Dr. Marc Bosse, with whom I had the privilege of writing my first paper.

I am also grateful for the people I saw on a day-to-day basis, my fellow lab mates both past and present. At the time of joining the lab, I had no lack of outstanding graduate students and postdocs to look up to. I was particularly inspired by Herr Lab alumni Dr. Samantha Grist and Dr. Shaheen Jeeawoody, who were my amazing mentors during my first year in the lab. From the early days of thoughtful discussions with Anjali, Alisha, Ali, Andoni, and Alden to boba runs today with Ana, Trinh, Anna, and Maya, I am proud to be a member of the Herrd.

Thank you to Dr. Noé Lozano for introducing me to the concept of a Ph.D. during the Stanford Summer Engineering Academy (SSEA). SSEA not only changed the trajectory of my life, but it is also where I met some of my best friends to this day. Thank you to Meltem Erol for championing DEI at UC Berkeley and making the initial introduction between me and Amy. Thank you to my fellow LAGSES and BEAST Officers for giving me the opportunity to be a part of the wider UC Berkeley Engineering community.

Countless individuals were indispensable in making this dissertation possible. Thank you, Catherine Dea, Kris Thompson, Thom Opal, and the rest of the staff at Stanley Hall. Thank you, Paul Lum and Naima Azgui of the QB3-Berkeley Biomolecular Nanotechnology Center, for running such an important facility for microfluidics work.

I was also fortunate to receive funding from several sources, including the National Science Foundation Graduate Research Fellowship and the Tom & Stacey Siebel Foundation Siebel Scholarship, as well as departmental awards, including the Brodie Scholar in Bioengineering Award (2020) and Lloyd Scholar in Bioengineering Award (2021).

Thank you to my amazing friends. Kristine Tan and Louise Hansen were more than just lab mates. Thank you for the spontaneous beach trips, food adventures, and being there to troubleshoot life and science with me every step of the way. Thank you, Gigi, for the daily phone calls and unhinged shenanigans that make life worth living. Thank you, Alejandra, for the countless dinners and movie nights. Thank you, Lysha, for going alongside me on the Ph.D. journey. And to my boyfriend, Andy, life with you is like surfing the most perfect Waikīkī wave. Thank you for being my surf partner, personal chef, and letting me commandeer your office to write this dissertation.

Thank you to my extended family, both here and in Mexico. To my sisters from other sisters, the world could never be a lonely place with you all by my side. Thank you to my grandparents, aunts, and uncles for the endless support. Thank you to my angels, my Tía Güera and Nina Chenta, who both passed away from stage 4 cancer during my time as a Ph.D. student. You give me all the more reason to continue pursuing my passion for biomedical research. You are dearly missed.

Finally, the appropriate words escape me to properly thank my family. I am grateful to have the most wonderful brother, Cristian, who has grown up to be the kindest and gentlest human. Needless to say, I would not be here without my mom and dad, who sacrificed so deeply so that Cristian and I could have a better life. I love you.

Chapter 1

Introduction

Descriptions of single-cell electrophoretic assays are reproduced with permission from:

Hansen, L.L., **Lomeli, G.**, Vlassakis, J., Herr, A.E. (2022). Single-Cell Resolution Immunoblotting. In: Sweedler, J.V., Eberwine, J., Fraser, S.E. (eds) Single Cell ‘Omics of Neuronal Cells. *Neuromethods*, vol 184. Humana, New York, NY. https://doi.org/10.1007/978-1-0716-2525-5_7.

1.1 Role of heterogeneity at the molecular and cellular level

To achieve a thorough understanding of the biological functions of cells, it is essential to acknowledge the existence of diversity at both the molecular and cellular level within living organisms. Contributing to cell-to-cell heterogeneity is the multitude of cell types and cell states that make up tissues, the immune system, cancer, and a variety of other normal and diseased biological systems [1, 2]. Additionally, the proteins within these cells exist in diverse protein states, called proteoforms, which are a result of transcriptional and post translational modifications and widely expand the kind of functions that a single gene can ultimately perform [3, 4]. To stand a chance in understanding the complex processes governing diseases such as cancer, we need tools that have the single-cell resolution, proteoform specificity, and multiplexing ability to provide critical data at these two layers of heterogeneity (Figure 1.1). Unfortunately, with existing technologies, we are largely blind to the proteoform state of single cells.

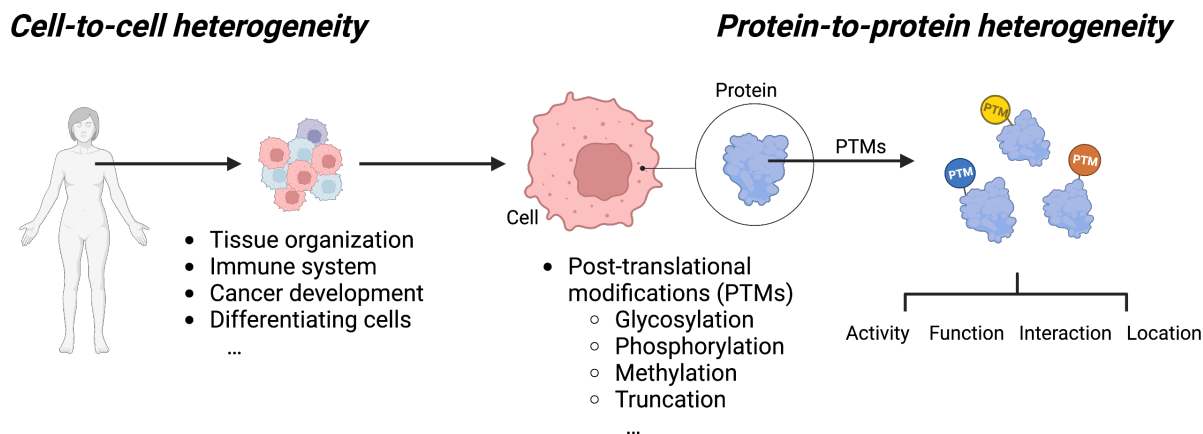


Figure 1.1: Schematic of the heterogeneity present at the molecular and cellular level.

1.2 Overview of state-of-the-art in single-cell proteomics

This section provides an overview of the current state of single-cell proteomic tools with special emphasis on why coupling the two key design criteria of proteoform specificity and multiplexing remains a challenge.

Mass spectrometry has been the workhorse of proteomics [5]. Single-cell mass spectrometry has been achieved by digesting proteins and then directly quantifying the peptides [6]. While superb multiplexing (>1000 proteins) has been achieved with this technique [7], proteoform specificity is hampered by the digestion step which makes it difficult to reconstruct proteoforms from the peptides [3].

Antibody based immunoassays, such as immunohistochemistry and flow cytometry, are the most commonly used techniques for single cell protein analysis. However, to differentiate between proteoforms, immunoassays require proteoform-specific antibodies that aren't prone to cross-reactivity with other proteoforms or with other molecules in the system. Proteoform-specific antibodies aren't always available [8]. For example, the phospho-ERK antibody is unable to differentiate the mono-phosphorylated or inactive proteoform from the diphosphorylated or active proteoform [9, 10]. Another salient example where current single-cell protein assays fall short is for the measurement of the oncoprotein, human epidermal growth factor receptor 2 (HER2). In breast cancer tumors expressing HER2, the presence of truncated HER2 proteoforms could be a possible mechanism for resistance to anti-HER2 antibody therapies in some patients [11]. However, identification of proteoforms with single-cell immunoassays, such as immunohistochemistry (IHC) of intact tissue slices, is difficult due to the lack of antibodies specific to all the truncated HER2 proteoforms [12].

Increasing multiplexing in single cell protein assays is a major challenge in analytical

chemistry. Multiplexed protein analysis provides a key advantage in identifying cell subpopulations [13]. The heterogeneous environment of breast cancer tumors is made up of stromal, tumor, and immune cells [14]. Categorizing and studying the diversity present in the immune cells is a challenge on its own. In polychromatic flow cytometry, at least 8 parameters are needed to perform basic phenotyping of a T-cell population [13]. If there are additional cell populations or proteins of interest for a given tumor study, conventional fluorescence-based techniques quickly become overwhelmed.

Immunoassays with fluorescence-based readout are limited in multiplexing (~ 3) due to spectral overlap between different channels [15]. To achieve higher multiplexing (~ 90), immunoassays employ serial staining immunofluorescence methods, which have several disadvantages such as incomplete signal removal and perturbation of antigens between cycles [16]. Among rising multiplexed imaging methods is multiplexed ion beam imaging by time-of-flight (MIBI-TOF), a mass cytometry imaging technology. MIBI-TOF has been used to perform simultaneous imaging of 36 protein targets in fixed tissue by employing metal-tagged antibodies [17]. However, MIBI-TOF of intact tissue sections is inherently an immunoassay and therefore still requires proteoform-specific antibodies that aren't prone to cross-reactivity.

Moreover, the fact that proteins exist as proteoforms further motivates the need for multiplexing. Not only are proteoform-specific antibodies sometimes unavailable given the vast quantity of proteoform species possible [3], but they require an additional channel in what is an already crowded multiplexed antibody panel. Therefore, there is a need for improved single-cell resolution, proteoform specific, multiplexed measurement tools.

1.3 Single-cell electrophoretic assays

To address the challenge of limited availability of proteoform-specific antibodies, researchers have turned to electrophoretic assays. Electrophoretic assays separate proteins based on their physicochemical properties before a readout, often immunoreagent-based, is performed [18]. Electrophoretic assays, such as Sodium Dodecyl Sulfate Polyacrylamide Gel Electrophoresis (SDS-PAGE), Capillary Electrophoresis (CE), Isoelectric Focusing (IEF), and Two-Dimensional Gel Electrophoresis (2D-PAGE), offer excellent proteoform specificity. However, they typically require high amounts of starting samples, rendering single-cell analysis on conventional gel and capillary electrophoresis systems unfeasible [19, 20].

Microanalytical tools open new avenues for biological and biochemical inquiry [21]. With the miniaturization of bulk methods, analytical methods with greater sensitivity and throughput have become possible. Our lab has introduced several single-cell electrophoretic assays, including the single-cell western blot (scWB) [22, 23] and single-cell isoelectric focusing (scIEF) [24] to enable single-cell proteoform analysis.

An early example of scIEF highlights the utility and role of single-cell electrophoretic assays within biology. After the initial discovery of tubulin proteoforms from bulk brain tissue lysate, it was unclear whether these diverse tubulins were attributed to cell-to-cell heterogeneity or proteoform heterogeneity at the single-cell level [25]. With a version of

scIEF in conjunction with radioactive labeling, multiple tubulin proteoforms were found to exist in single neuron cells [25, 26].

The major steps of scIEF and scWB are summarized as follows: (1) immunoblot hydrogel fabrication, (2) sample preparation and introduction of cells, (3) polyacrylamide gel electrophoresis, (4) immunoprobng, and (5) data analysis. Each step presents a series of design considerations and points of optimization for proper protein separation.

Separating Protein Targets by Size (scWB)

The governing principles of scWB are analogous to those of bulk western blots. Electrophoresis is the migration of charged particles under an applied electric field. Electrophoretic separations are conducted in a wide range of separation media, including free solution and sieving matrix. Given the pore size of polyacrylamide gel and the characteristic dimension of most proteins, polyacrylamide gel electrophoresis (PAGE) is well suited to resolve protein targets. During PAGE, protein species electromigrate through a porous polyacrylamide hydrogel matrix under the applied electric field. The porous matrix differentially impedes protein electromigration on the basis of size and structure of each protein molecule.

In a sieving matrix, particles migrate with a velocity related to particle size, as described by Ferguson [27]:

$$\log(\mu_{EP,gel}) = \log(\mu_{EP,fs}) - K_r T \quad (1.1)$$

where $\mu_{EP,gel}$ is the electrophoretic mobility of the particle through the gel; $\mu_{EP,fs}$ is the electrophoretic mobility of the particle in free solution; K_r is the empirically determined retardation coefficient that describes how much the sieving matrix reduces the electrophoretic mobility of the particle; and T is the percentage (w/v) of total monomer in solution (acrylamide and bis).

Protein sizing is PAGE analysis of denatured, reduced proteins coated with the anionic detergent sodium dodecyl sulfate (SDS). Also called SDS-PAGE, protein sizing relies on the uniform mass to-charge ratio coating of SDS that linearizes proteins and gives all proteins the same free solution electrophoretic mobility ($\mu_{EP,fs}$), making K_r dependent only on protein length [28, 29]. In this way, the electrophoretic mobility of protein targets in SDS-PAGE is related to the molecular mass of the proteins with a log-linear relationship. In comparison, non-denaturing conditions (e.g., native PAGE) result in electromigration proportional to the zeta potential ($\mu_{EP,fs}$) and the retardation coefficient [30, 31]. The quaternary structures of proteins affect retardation in native PAGE, making protein identification by migration distance more confounding than when using a protein sizing mechanism. SDS-PAGE is the most common type of gel electrophoresis used in western blotting and scWB. The electrophoretic separation of denatured proteins by molecular mass is particularly well suited for interrogation of truncated protein isoforms that can make antibody-based distinction of

different isoforms challenging without the added selectivity of a size-based separation [12].

Separating Protein Targets by Isoelectric Point (scIEF)

scIEF miniaturizes the fundamental principles governing bulk IEF. IEF is a technique used in analytical and preparative chemistry to separate proteins based on their isoelectric point (pI). The pI is the pH at which a particular molecule (i.e., a protein) carries zero net electrical charge. The pI of a given protein is dictated by both the amino acid sequence and any post-translational modifications [32, 33]. Proteins rich in amino acids with acidic side chains will have a lower pI than proteins with a higher proportion of amino acids with basic side chains. To accomplish a charge-based protein separation, a stable pH gradient is established. The pH boundary conditions define the pH gradient (slope, range) and, thus, determine which proteins will be resolved. For example, a pH 4–7 gradient would be unsuitable for analysis of proteins that are more acidic (pI < 4) or more basic (pI > 7). Although alternative methods exist for creating a pH gradient (see section 1.4 below), scIEF utilizes a series of commercially available carrier ampholytes that stack in the presence of an applied electric potential to create a pH gradient [24]. Due to the use of carrier ampholytes for IEF, the pH gradient in scIEF is subject to cathodic drift of $21 \pm 3 \mu\text{m}/\text{min}$ [34]. When proteins electromigrate into the pH gradient region from a boundary, the biomolecules traverse the pH gradient according to protein charge which is impacted by dynamic protonation and deprotonation. Migration halts when proteins reach a region in the gradient where a net-zero charge is achieved (where pH = pI). While the pH gradient is stable, the focused proteins will be in dynamic equilibrium in their focused position, as diffusion causes proteins to migrate away from pH = pI, and electrophoretic force returns the proteins back to pH = pI [32]. In scIEF, this focusing effect keeps proteins from single-cell lysate highly concentrated even across several millimeters of separation lane [24].

One area for improvement in scIEF is throughput. scIEF has a throughput suitable for rare-cell analysis, but not well suited to analysis of large populations of cells. A scIEF chip houses ~ 50 microwells, which reduces the number of analyzed cells to ~ 10 after cell settling and quality control losses. Another throughput limitation of scIEF is assay run time. The lid gel must be made fresh for each experimental run, which leads to a run time per microdevice of ~ 2.5 h.

Diffusive protein losses during single-cell immunoassays

scWB has an estimated limit of detection of 27,000 molecules using purified EGFP [22]. scIEF has an approximate lower limit of detection of 42,000 molecules [24]. Given that the median protein copy number in a mammalian cell is about 170,000 molecules per cell [35], current single-cell electrophoretic technologies are potentially incapable of detecting most of the lower half of the proteome. One of the major limitations to sensitivity in single-cell electrophoretic assays is diffusive protein loss during the cell lysis and electrophoresis stages.

Single-cell immunoblot (scIB) microdevices are “open microfluidic” devices, composed

of a thin polyacrylamide (PA) gel layer affixed to a glass slide (or other planar support). Anywhere between tens (for scIEF) to thousands of microwells (for scWB) decorate the PA gel surface, enabling the isolation of individual cells for subsequent analysis. Moreover, with the recent development of 3D projection electrophoresis for scIB, the microwell density of scIB was increased from 2 microwells/mm² to 25 microwells/mm² to further increase throughput [36].

Immediately after cell isolation in microwells, in-well chemical lysis and protein solubilization is initiated by the rapid introduction of a bifunctional lysis/electrophoresis buffer. Previous quantification of diffusive protein losses during cell lysis have determined that approximately 40% of the protein sample is lost during cell lysis alone [22].

Moreover, Joule heating in the lysis/electrophoresis buffer during electrophoresis further increases diffusivity and diffusive losses of the proteins out of the microwell and gel, resulting in lower separation performance and sensitivity [37]. As a result, microwell spacing in the direction orthogonal to the electric field is constrained by the spreading and crossover of adjacent protein peaks as a result of lateral diffusion.

Immunoblot hydrogel chemistry

The chemical and physical properties of the PA gel are highly tunable, which supports the extended applications of scIB assays. A standard PA gel precursor contains the following basic components: the primary monomer (acrylamide), the crosslinker (e.g., bis-acrylamide), and the polymerization initiators [38]. While the PA gel is composed primarily of acrylamide monomers, additional properties can be achieved by incorporating copolymers [39]. The following PA gel features will be especially relevant in the context of this Dissertation:

- *Protein photo-capture*: A key additive for scIB assays is the inclusion of a photo-capture molecule to immobilize proteins in the 3D PA gel, replacing the transfer and blotting of proteins to a separate membrane in conventional western blotting. A range of photo-capture molecules are available, including N-[3-[(3-benzoylphenyl)-formamido]propyl] methacrylamide (BPMAC), tetrazole [40], and diazirine [41–43]. Conventionally, scWB and scIEF use BPMAC for UV capture of proteins within the PA gel after electrophoresis. BPMAC is added to the gel precursor and is polymerized into the PA gel backbone through its methacrylamide reactive group.
- *Pore size*: PA gel pore size is an important variable in electrophoretic assays, impacting separation resolution, limit of detection, and immunoprobng efficiency. In general, a smaller pore-size (higher total acrylamide concentration) PA gel improves separation resolution [44], but small gel pores decrease immunoprobng efficiency due to size exclusion of antibody probes from the PA gel [45]. Like conventional bulk westerns, single-cell protein sizing can be performed in PA gel of either uniform pore size or gradient pore size. For uniform pore-size PA gel, the final acrylamide and crosslinker concentration is adjusted to the desired concentration, and chemical polymerization is

typically used. While more laborious to make, gradient pore-size PA gel offers greater separation resolution over a large range of protein masses compared to uniform gels. Multiple back-to-back pore gradients can be created in PA gel with photoinitiated polymerization through a grayscale mask [46]. The grayscale mask modulates the UV dose for photopolymerization, leading to faster polymerization and therefore smaller pores in lighter regions and vice versa. The inclusion of an acid-labile crosslinker in the PA gel allows the gradient-pore PA gel to be reverted to a uniform PA gel for even immunoprobings [46]. In scIEF, the PA gel serves as an anti-convective and immobilization medium. The pore size does not play as important a role in separation resolution as in the size-based separations of scWB.

1.4 Isoelectric focusing

Comparison of carrier ampholyte and immobilized pH gradient methods

The use of carrier ampholytes (CAs) and immobilized pH gradients (IPGs) are two different methods to create a pH gradient for isoelectric focusing (IEF). IEF with CAs or IPGs is defined as CA-IEF or IPG-IEF, respectively.

Carrier Ampholytes: CAs are a mixture of small amphoteric molecules with different pI values. They are typically added to the gel or sample buffer to generate a pH gradient upon the application of an electric potential. The amphoteric nature of CAs allows CAs to reach a steady state position along the pH gradient during IEF. CAs migrate alongside the protein sample during IEF [32]. Some features of CA-IEF include [47–50]:

- CAs are compatible with a more diverse array of gel types compared to IPG gels (since the Immobiline molecules must be-copolymerized with the gel).
- The distribution/ migration pattern of CAs during IEF may fluctuate run-to-run, leading to increased technical variation.
- The pH range of CAs can be adjusted by selecting specific ampholyte mixtures, but there are less pH gradient ranges available than for IPG-IEF.
- Scaling up CA-IEF challenging due to difficulties maintaining consistent CA distribution and migration during large-scale separations.
- Cathodic drift, or the tendency for molecules to move toward the cathode during electrophoresis, is pronounced in CA-IEF.
- CAs can interact with the sample in ways deleterious to sample analysis.

Immobilized pH Gradient: An IPG is a stable, pre-formed pH gradient that is covalently immobilized within the gel separation matrix. IPGs are prepared by polymerizing acrylamide

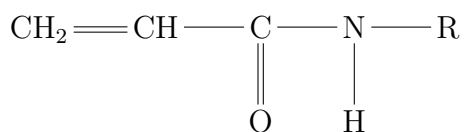
monomers together with pH gradient-forming compounds called Immobilines. Therefore, the pH gradient is established during the gel fabrication process and remains fixed within the gel during IEF [47]. Some features of IPG-IEF include [47, 48, 51, 52]:

- The pH gradient within an IPG gel is well-defined and remains consistent across multiple runs, resulting in better reproducibility of protein separation.
- IPGs are easy to use once separation gel is fabricated.
- IPGs are easily amenable to pH gradient engineering.
- IPGs can be easily scaled up for high-throughput separations. Multiple IPG strips or gels can be run in parallel, and the pH gradient remains stable and reproducible across all of the gels.
- There is no cathodic drift in IPG-IEF.
- It is more complex to fabricate IPG gels compared to gels for CA-IEF.

It is also possible to combine both CAs and IPG in what is called IEF with mixed-bed CA/IPG gels, where a primary, stationary, Immobiline driven pH gradient coexists with a secondary, soluble, CA driven, gradient [53]. The key advantage of mixed-bed CA/IPG gels over IPG gels alone is improved solubility of proteins, especially membrane proteins [47].

Immobilized pH gradient theory

In an IPG gel, the pH of the gel is determined by the presence and concentration of several Immobilines, which are the compounds taking part in protolytic equilibria [54]. Immobilines have the following general formula:



where R is either a carboxyl or tertiary amino group. The Immobiline is a weak acid or base defined by its pK value.

An important feature of an IPG gel is its buffering capacity. Buffer solutions contain a high concentration of a weak acid and its conjugate base (or a weak base and its conjugate acid). Because these components neutralize added H⁺ or OH⁻, buffers are highly resistant to changes in pH. This “buffer” behavior is highly desired during IEF, where a pH gradient must be maintained in a dynamic environment (as proteins migrate toward the pH at which they are isoelectric).

To be able to buffer at a precise pH value, both an acid and base Immobiline are necessary. The underlying principle is an acid base titration, and the pH value is defined by the

Henderson-Hasselback equation. Below is the modified Henderson-Hasselback equation for the case in which the buffer is an acidic Immobiline and the basic Immobiline is fully ionized (titrant) [47].

$$pH = pK_A + \log[C_B/(C_A - C_B)] \quad (1.2)$$

where C_A is the molarity of the acidic Immobiline with $pK = pK_A$ and C_B is the molarity of the basic Immobiline. Buffers are most effective when $pH = pK_A$ of the buffering species, but there is a broad range of pH in a gradient, by definition, so it is important to ensure even buffering throughout a wide gradient. The jump from narrow and ultranarrow pH gradients to wide pH gradients (≥ 2 pH units) was not trivial and required the introduction of new Immobiline species (to provide simultaneous buffering over wider pH ranges) as well as complex algorithms to optimize Immobiline recipes that would yield linear pH ranges with relatively constant buffering capacity and ionic strength, since the Henderson-Hasselback equation above is not sufficient for pH calculation of complex mixtures. For ease of IPG technology distribution, Immobiline recipe tables exist for a wide range of desired gradients [47].

1.5 Multiplexed ion beam imaging

Multiplexed ion beam imaging by time-of-flight (MIBI-TOF) is an emerging multiplexed imaging method. MIBI-TOF was developed for multiplexed measurement of proteins from tissue sections [17, 55]. MIBI-TOF uses secondary ion mass spectrometry (SIMS). SIMS is a technique used to analyze the composition of solid surfaces and thin films by sputtering the surface of the specimen with a focused primary ion beam and collecting and analyzing ejected secondary ions [56]. MIBI-TOF improved on the prior NanoSIMS 50L system. Previously, NanoSIMS 50/50L was state-of-the-art in the field of mass spectrometry imaging [57].

The following terms and concepts are useful when speaking about SIMS instruments (i.e., MIBI-TOF) [17, 56, 57]:

- *Surface elemental analysis technique*: Historically, SIMS belongs to a class of surface elemental analysis techniques. SIMS is an elemental technique because molecular information is rarely captured in SIMS. In fact, the MIBI-TOF instrument is specifically designed to filter out polyatomics from analysis.
- *Sputtering*: The basis of SIMS is the sputtering process. Dynamic SIMS instruments, like MIBI-TOF and NanoSIMS 50 L, continuously sputter the sample with a primary beam that, in turn, produces a continuous stream of secondary ions. Changing the incidence angle of primary ion beam affects the sputtering yield (amount of secondary ions released).
- *Sample charging*: In general, the SIMS ion beam will cause the sample to charge positively because the primary beam is usually positive (including in MIBI-TOF) and the

primary ion current is significantly larger than the secondary ion current. The ejection of secondary electrons from the sample surface also causes an increase in positive charge. Sample charging can have deleterious effects on analysis so the following are methods for charge compensation: adding a conductive coating on the sample, adding a conductive grid on the sample, and electron beam neutralization.

SIMS data are typically presented in three formats: mass spectra, depth profiles, and images:

- Mass spectra display secondary ion intensity as a function of mass to charge ratio.
- Depth profiles show secondary ion intensity as a function of depth into the sample.
- Ion images display secondary ion lateral distribution. This is the type of image commonly employed to display MIBI-TOF micrograph images.

With an introduction of SIMS fundamentals, we can now summarize the major steps of MIBI-TOF as follows [17]: (1) The first step is to mount the sample (typically a tissue slice) on a standard sized glass slide coated in gold. (2) The second step is to label tissue sections with upwards of 40 metal-tagged antibodies. (3) Then, an oxygen duoplasmatron primary ion beam atomizes and ionizes the tissue layer-by-layer, and the sputtered secondary ions are fed into a time-of-flight mass spectrometer. (4) A mass spectrum is generated for each image spot which can be used to produce a high dimensional image based on the abundance of each metal isotope. The 40 targets can be captured simultaneously because metal-tagged antibodies do not suffer from spectral overlap to the same degree that fluorescently-tagged antibodies do. These images can look and function very similar to conventional fluorescence microscopy images.

1.6 Dissertation overview

The underlying fundamental goal of the work presented in this dissertation is to engineer the tools to power the rise of a new field: single-cell proteoform analysis. This dissertation introduces enabling technologies to all major areas of the electrophoretic assay workflow, including a new active cell settling technique for single-cell electrophoresis, alternative hydrogels for both western blotting and isoelectric focusing, and a novel multiplexed imaging modality for single-cell electrophoresis.

In Chapter 2, we report our work towards MIBI-TOF of single-cell immunoblotting. Specifically, we scrutinize the impact metal-tagging has on antibody probe transport and performance in polyacrylamide gel. We also investigate the efficient release of metal-tagged antibodies from polyacrylamide gel for mass spectrometry detection. Our demonstration of MIBI-TOF detection of proteoforms separated by charge is a key step towards a single-cell resolution, multiplexed, and proteoform specific measurement tool.

In Chapter 3, we present the first polydimethylsiloxane (PDMS)-based, immunoprobed, microfluidic IPG-IEF device to our knowledge. IPG-IEF overcomes the limitations of carrier ampholyte IEF, such as pH gradient instability and lack of pH gradient tunability. We demonstrate separation performance on par with our single-cell IEF device, including resolving analytes differing by only 0.1 pH.

In Chapter 4, we explore strategies to create gradient pore size gels for 3D projection electrophoresis. Gradient pore size gels offer several advantages over uniform pore size gels typically used for 3D projection electrophoresis (i.e., separate a larger range of molecular weight proteins over the same distance). In this chapter, we will introduce two methods for producing gradient pore size hydrogels: (1) we modulate the concentration of gel precursor components across the hydrogel to modulate pore size, and (2) we modulate the concentration of oxygen across the hydrogel to selectively inhibit polymerization and therefore modulate pore size.

The focus of Chapter 5 is on the design of a microfluidic scWB device that, for the first time, couples hydrodynamic cell trapping, electrical lysis, and protein electrophoresis. We harness the geometry of the hydrodynamic cell trap for a dual purpose: electrical cell lysis for native PAGE.

In Chapter 6, we summarize the advancements and technologies introduced in this dissertation and provide suggestions for interesting and impactful future directions in the field of single-cell proteoform analysis.

References

- (1) Wang, D.; Bodovitz, S. *Trends in Biotechnology* **2010**, *28*, 281–290.
- (2) Keren, L.; Angelo, M. *Nature Cancer* **2020**, *1*, 156–157.
- (3) Aebersold, R. et al. *Nature Chemical Biology* **2018**, *14*, 206–214.
- (4) Smith, L. M.; Kelleher, N. L. *Nature Methods* **2013**, *10*, 186–187.
- (5) Levy, E.; Slavov, N. *Essays in Biochemistry* **2018**, *62*, 595–605.
- (6) Slavov, N. *Current Opinion in Chemical Biology* **2021**, *60*, 1–9.
- (7) Budnik, B.; Levy, E.; Harmange, G.; Slavov, N. *Genome Biology* **2018**, *19*, 161.
- (8) Regnier, F. E.; Kim, J. *Analytical chemistry* **2018**, *90*, 361–373.
- (9) Wortzel, I.; Seger, R. *Genes & Cancer* **2011**, *2*, 195–209.
- (10) Shi, T. et al. *Analytical chemistry* **2015**, *87*, 1103–1110.
- (11) Arribas, J.; Baselga, J.; Pedersen, K.; Parra-Palau, J. L. *Cancer Research* **2011**, *71*, 1515–1519.
- (12) Kang, C.-C.; Ward, T. M.; Bockhorn, J.; Schiffman, C.; Huang, H.; Pegram, M. D.; Herr, A. E. *npj Precision Oncology* **2018**, *2*, 1–10.

- (13) Chattopadhyay, P. K.; Roederer, M. *Methods* **2012**, *57*, 251–258.
- (14) Jackson, H. W.; Fischer, J. R.; Zanotelli, V. R. T.; Ali, H. R.; Mechera, R.; Soysal, S. D.; Moch, H.; Muenst, S.; Varga, Z.; Weber, W. P.; Bodenmiller, B. *Nature* **2020**, *578*, 615–620.
- (15) Dickinson, M.; Bearman, G.; Tille, S.; Lansford, R.; Fraser, S. *BioTechniques* **2001**, *31*, 1272–1278.
- (16) Yang, L.; George, J.; Wang, J. *PROTEOMICS* **2020**, *20*, 1900226.
- (17) Keren, L. et al. *Science Advances* **2019**, *5*, eaax5851.
- (18) Moritz, C. P. *Journal of Proteomics* **2020**, *212*, 103575.
- (19) *Protein Electrophoresis: Methods and Protocols*; Kurien, B. T., Scofield, R. H., Eds.; Methods in Molecular Biology, Vol. 869; Humana Press: Totowa, NJ, 2012.
- (20) Hughes, A. J.; Lin, R. K. C.; Peehl, D. M.; Herr, A. E. *Proceedings of the National Academy of Sciences* **2012**, *109*, 5972–5977.
- (21) Duncombe, T. A.; Tentori, A. M.; Herr, A. E. *Nature Reviews Molecular Cell Biology* **2015**, *16*, 554–567.
- (22) Hughes, A. J.; Spelke, D. P.; Xu, Z.; Kang, C.-C.; Schaffer, D. V.; Herr, A. E. *Nature Methods* **2014**, *11*, 749–755.
- (23) Kang, C.-C.; Yamauchi, K. A.; Vlassakis, J.; Sinkala, E.; Duncombe, T. A.; Herr, A. E. *Nature Protocols* **2016**, *11*, 1508–1530.
- (24) Tentori, A. M.; Yamauchi, K. A.; Herr, A. E. *Angewandte Chemie International Edition* **2016**, *55*, 12431–12435.
- (25) Gozes, I.; Ivashko-Pachima, Y.; Kapitansky, O.; Sayas, C. L.; Iram, T. *Journal of Neuroscience Methods* **2019**, *323*, Publisher: Elsevier B.V., 119–124.
- (26) Gozes, I.; Sweadner, K. J. *Nature* **1981**, *294*, 477–480.
- (27) Ferguson, K. A. *Metabolism* **1964**, *13*, 985–1002.
- (28) Burnette, W. N. *Analytical Biochemistry* **1981**, *112*, 195–203.
- (29) Bischoff, K. M.; Shi, L.; Kennelly, P. J. *Analytical Biochemistry* **1998**, *260*, 1–17.
- (30) Blattler, D. P.; Reithel, F. J. *Journal of Chromatography A* **1970**, *46*, 286–292.
- (31) Schagger, H.; Cramer, W. A.; Vonjagow, G. *Analytical Biochemistry* **1994**, *217*, 220–230.
- (32) Righetti, P., *Isoelectric Focusing: Theory, Methodology and Applications*; Elsevier: Amsterdam, 1983.
- (33) Kahle, J.; Wätzig, H. *ELECTROPHORESIS* **2018**, *39*, 2492–2511.
- (34) Yamauchi, K. A.; Tentori, A. M.; Herr, A. E. *ELECTROPHORESIS* **2018**, *39*, 1040–1047.

- (35) Li, J. J.; Bickel, P. J.; Biggin, M. D. *PeerJ* **2014**, *2014*, 1–26.
- (36) Grist, S. M.; Mourdoukoutas, A. P.; Herr, A. E. *Nature Communications* **2020**, *11*, 6237.
- (37) Vlassakis, J.; Herr, A. E. *Analytical Chemistry* **2017**, *89*, 12787–12796.
- (38) Menter, P. Acrylamide Polymerization — A Practical Approach, en, 2000.
- (39) Neira, H. D.; Jeeawoody, S.; Herr, A. E. *Advanced Functional Materials* **2020**, *30*, 2005010.
- (40) Zhang, T.; Li, S.; Warden, A. R.; Ghalandari, B.; Li, H.; Zhi, X.; Xie, H.; Ding, X. *Advanced Functional Materials* **2020**, *30*, 1910739–1910739.
- (41) Dorman, G.; Prestwich, G. D. *Biochemistry* **1994**, *33*, 5661–5673.
- (42) Blawas, A. S.; Reichert, W. M. *Biomaterials* **1998**, *19*, 595–609.
- (43) Tan, K. Y.; Desai, S.; Raja, E.; Etienne, C.; Webb, B.; Herr, A. E. *Analyst* **2021**.
- (44) Kang, C.-C.; Lin, J.-M. G.; Xu, Z.; Kumar, S.; Herr, A. E. *Analytical Chemistry* **2014**, *86*, 10429–10436.
- (45) Su, A.; Smith, B. E.; Herr, A. E. *Analytical Chemistry* **2020**, *92*, 875–883.
- (46) Duncombe, T. A.; Kang, C.-C.; Maity, S.; Ward, T. M.; Pegram, M. D.; Murthy, N.; Herr, A. E. *Advanced Materials* **2016**, *28*, 327–334.
- (47) Righetti, P. G., *Immobilized PH Gradients: Theory and Methodology*; Elsevier: 1990.
- (48) Xia, L.; Lin, F.; Wu, X.; Liu, C.; Wang, J.; Tang, Q.; Yu, S.; Huang, K.; Deng, Y.; Geng, L. *Journal of Separation Science* **2014**, *37*, 3174–3180.
- (49) Xie, S.-F.; Gao, H.; Niu, L.-L.; Xie, Z.-S.; Fang, F.; Wu, Z.-Y.; Yang, F.-Q. *Journal of Separation Science* **2018**, *41*, 2085–2091.
- (50) Thormann, W.; Mosher, R. A. *ELECTROPHORESIS* **2021**, *42*, 814–833.
- (51) Görg, A.; Weiss, W.; Dunn, M. J. *PROTEOMICS* **2004**, *4*, 3665–3685.
- (52) Guo, C.-G.; Li, S.; Wang, H.-Y.; Zhang, D.; Li, G.-Q.; Zhang, J.; Fan, L.-Y.; Cao, C.-X. *Talanta* **2013**, *111*, 20–27.
- (53) Rabilloud, T.; Barzaghi, B.; Giorgi Righetti, P. *Journal of Biochemical and Biophysical Methods* **1988**, *16*, 237–241.
- (54) Bjellqvist, B.; Ek, K.; Giorgio Righetti, P.; Gianazza, E.; Görg, A.; Westermeier, R.; Postel, W. *Journal of Biochemical and Biophysical Methods* **1982**, *6*, 317–339.
- (55) Angelo, M.; Bendall, S. C.; Finck, R.; Hale, M. B.; Hitzman, C.; Borowsky, A. D.; Levenson, R. M.; Lowe, J. B.; Liu, S. D.; Zhao, S.; Natkunam, Y.; Nolan, G. P. *Nature Medicine* **2014**, *20*, 436–442.
- (56) Stevie, F., *Secondary Ion Mass Spectrometry: Applications for Depth Profiling and Surface Characterization*; Momentum Press: 2015.

(57) Nuñez, J.; Renslow, R.; Cliff, J. B.; Anderton, C. R. *Biointerphases* **2017**, *13*, 03B301.

Chapter 2

Multiplexed Ion Beam Imaging Readout of Single-Cell Immunoblotting

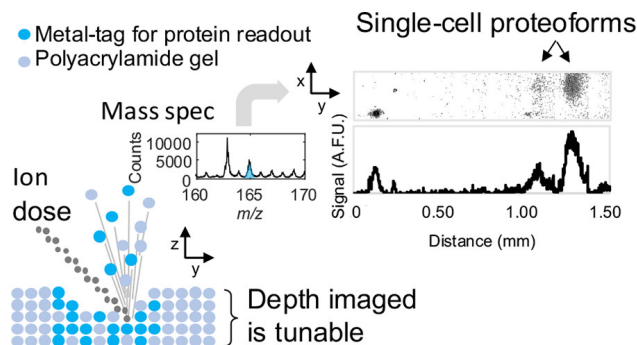
Reproduced with permission from:

Lomeli, G., Bosse, M., Bendall, S.C., Angelo, M., and Herr, A.E. Multiplexed Ion Beam Imaging Readout of Single-Cell Immunoblotting. *Anal Chem* **93**, 24 (2021).
<https://doi.org/10.1021/acs.analchem.1c01050>

2.1 Abstract

Improvements in single-cell protein analysis are required to study the cell-to-cell variation inherent to diseases, including cancer. Single-cell immunoblotting (scIB) offers proteoform detection specificity, but often relies on fluorescence-based readout and is therefore limited in multiplexing capability. Among rising multiplexed imaging methods is multiplexed ion beam imaging by time-of-flight (MIBI-TOF), a mass spectrometry imaging technology. MIBI-TOF employs metal-tagged antibodies that do not suffer from spectral overlap to the same degree as fluorophore-tagged antibodies. We report for the first-time MIBI-TOF of single-cell immunoblotting (scIB-MIBI-TOF). The scIB assay subjects single-cell lysate to protein immunoblotting on a microscale device consisting of a 50- to 75- μm thick hydrated polyacrylamide (PA) gel matrix for protein immobilization prior to in-gel immunoprobng. We confirm antibodyprotein binding in the PA gel with indirect fluorescence readout of metal-tagged antibodies. Since MIBI-TOF is a layer-by-layer imaging technique, and our protein target is immobilized within a 3D PA gel layer, we characterize the protein distribution throughout the PA gel depth by fluorescence confocal microscopy and confirm that the highest signal-to-noise ratio is achieved by imaging the entirety of the PA gel depth. Accordingly, we report the required MIBI-TOF ion dose strength needed to image varying

PA gel depths. Lastly, by imaging $\sim 42\%$ of PA gel depth with MIBI-TOF, we detect two isoelectrically separated TurboGFP (tGFP) proteoforms from individual glioblastoma cells, demonstrating that highly multiplexed mass spectrometry-based readout is compatible with scIB.



2.2 Introduction

Single-cell analysis tools tease apart the cell-to-cell variability driving many important biological processes, such as cancer and drug resistance [1]. Underlying cellular heterogeneity is differential protein expression in individual cells; this molecular heterogeneity includes differential proteoform expression. Proteoforms are highly similar–yet chemically distinct–proteins originating from a single gene. Proteoforms often have unique functions [2, 3]. For instance, in breast cancer tumors expressing human epidermal growth factor receptor 2 (HER2), the presence of truncated HER2 proteoforms has been connected to a decrease in the effectiveness of antibody therapy [4]. Moreover, despite the importance of measuring multiple proteins from single cells (i.e., to interrogate molecular circuits [5] or categorize cell types [6]), target multiplexing in single-cell protein assays remains a major challenge in analytical chemistry [5].

Current single-cell proteomic tools lack the capability to provide both proteoform specificity and high target multiplexing. Identification of proteoforms with conventional immunoassays, such as immunohistochemistry (IHC) and flow cytometry, requires proteoform-specific antibodies. Given the diversity of proteoform species possible, proteoform-specific antibodies are sometimes unavailable [7]. Further, each new target-specific probe requires an additional detection channel in what is usually an already crowded multiplexed antibody panel. Moreover, immunoassay methods typically rely on fluorescence detection as a readout, which has limited multiplexing ability due to the spectral overlap of fluorophores [8]. Mass spectrometry has directly detected >1000 protein types with single-cell resolution, but existing single-cell mass spectrometry has low throughput [1], which makes identification of rare-cell types difficult. Moreover, current single-cell mass spectrometry utilizes a “bottom-up” approach, and proteoforms are often not distinguishable with bottom-up mass spectrometry due to measurement of peptides, not intact proteins [2]. Thus, an unmet need

remains for a single-cell protein analysis tool that provides proteoform specificity and is amenable to multiplexed protein-target detection.

Multiplexed ion beam imaging by time-of-flight (MIBI-TOF) is a mass spectrometry imaging technique especially designed for multiplexing and has been used to simultaneously image dozens of protein targets from fixed tissue [9]. For MIBI-TOF, the sample of interest, typically a tissue slice, is first immunoprobed with metal-isotope-tagged antibodies with each metal-isotope providing a distinct detection channel for target multiplexing. Then, MIBI-TOF uses secondary ion mass spectrometry (SIMS) to rasterize the sample with a primary ion beam, which sputters elements from both the metal-tagged antibodies and the sample to a time-of-flight spectrometer, generating a high parameter image comprised of the mass spectrum of each pixel. Although powerful in terms of target multiplexing and single-cell resolution, MIBI-TOF of intact tissue slices requires proteoform-specific antibodies for proteoform detection, and finding reproducible and specific antibody probes for mass spectrometry imaging is a challenge [10].

Single-cell immunoblotting (scIB) provides proteoform specificity by first separating proteins by size (single-cell Western blot [scWB] [11]) or charge (single-cell isoelectric focusing [scIEF] [12]), which relaxes the requirement of proteoform-specific antibodies since proteoforms are spatially separated prior to immunoprobing. Multiplexing to 12 protein targets in single cells has been reported in scIB by using an antibody stripping and reprobing approach in which 13 protein targets are imaged at a time with immunofluorescence, followed by a chemical stripping step, and the strip and reprobe process is cyclically repeated for additional targets [13]. However, there is a $\sim 75\%$ drop in immunoprobed signal after just one round of stripping [14]. Such signal losses create a challenge to target multiplexing that requires multiple stripping rounds, especially for the detection of low abundance proteins. The primary mechanism of signal decrease during stripping and reprobing is loss of $\sim 50\%$ of immobilized protein during the first round of stripping [14]; therefore, it is of great interest to eliminate the need for stripping altogether to achieve higher multiplexing.

To this end, here we introduce scIB with a MIBI-TOF readout. We report the characterization and validation steps taken toward realizing this technology. This work aims to understand the physics governing both metal-tagged probe introduction and extraction from a polyacrylamide (PA) gel matrix for mass spectrometry detection, using the model protein TurboGFP (tGFP). Since metal-tagging increases antibody probe size, which could lead to increased size exclusion from the PA hydrogel matrix, we verify that metal-tagged antibodies can bind to their target in a scIB assay. Then, we characterize the depth distribution of signal in the 3D hydrogel matrix used by scIB assays in order to determine the percentage of the sample depth that should be imaged with MIBI-TOF, since physical removal of the substrate is needed for detection. In SIMS, the number of sputtered ions, and therefore thickness of the sample that is rasterized away, is related to the ion dose delivered to the sample per unit area (referred to as ion dose, hereafter) [15]. Accordingly, we measure the gel depth rasterized with varying ion doses. Finally, we image isoelectrically focused tGFP proteoforms from single cells with both a fluorescence microarray scanner and MIBITOF, utilizing an ion dose that rasterized approximately 42% of the gel depth, to demonstrate

that scIB assays are compatible with MIBI-TOF detection.

2.3 Materials and Methods

Chemicals/Reagents. PA gels were cast on silicon wafers (WaferPro C04009) microfabricated with SU8 3050 photoresist (MicroChem Y311075) using custom in-house-designed masks (CAD/ART Services) and coated with dichlorodimethylsilane (Sigma 440272). An Ultrapure Millipore filtration system provided deionized water (18.2 M Ω). 3-(Trimethoxysilyl)propyl methacrylate (Sigma 440159), methanol (VWR BDH1135), and glacial acetic acid (Fisher Scientific A38S) were used for silanization of standard glass slides (VWR 48300-048) to covalently graft the PA gel to the microscope slide. 30%T 29:1 acrylamide/bis-acrylamide solution (Sigma A3574), 1.5 M pH 8.8 TrisHCl (TekNova T1588), N-[3-[(3-benzoylphenyl)-formamido]propyl] methacrylamide (BPMAC, custom synthesized by PharmAgra Laboratories), ammonium persulfate (APS, Sigma A3678), and N,N,N,N-tetramethylethylenediamine (TEMED, Sigma T9281) were used for microwell PA gel polymerization used in both scWB and scIEF. scWB was conducted using sodium deoxycholate (Sigma D6750), sodium dodecyl sulfate (SDS, Sigma L3771), TritonX-100 detergent (Sigma X100), and premixed 10 \times Tris/glycine electrophoresis buffer (25 mM Tris, pH 8.3; 192 mM glycine, BioRad 1610734) for the cell lysis buffer. scIEF was conducted using the Immobiline pKa 3.6 and pKa 9.3 acrylamido buffers (Sigma 01716, 01738), ZOOM Carrier Ampholytes pH 47 (Thermo Fischer Scientific ZM0022), 40%T 29:1 acrylamide/bis-acrylamide solution (Sigma A7802), urea (Sigma U5378), thiourea (Sigma T8656), 3-[(3-Cholamidopropyl)dimethylammonio]-1-propanesulfonate (CHAPS, Sigma RES1300C), digitonin (Sigma D141), UV photoinitiator 2,2-Azobis(2-methyl-N-(2-hydroxyethyl) propionamide) (VA086, Wako Chemicals 01319342), an ABS electrophoresis device designed and printed in-house, graphite electrodes (Bio-Rad 1702980), GelSlick (Lonza 50640), borosilicate glass sheets (McMaster-Carr 8476K62), and 0.5 mm gel spacers (CBS Scientific MVS0510- R). The antibody probes used were primary rabbit anti-tGFP antibody (Pierce PA5-22688) and secondary polyclonal antibody AlexaFluor-647-labeled donkey anti-rabbit (Invitrogen A-31573). Bovine serum albumin (BSA, A7030) was purchased from Sigma-Aldrich. Tris-buffered saline with Tween-20 (TBS-T, Cell Signaling Technologies 9997S) was used for gel incubation and wash steps.

Antibody Conjugation. Holmium (Ho)-tagged (metal-tagged) primary rabbit-anti-tGFP antibody was prepared using the MIBItag Conjugation Kit (Ho) (Ionpath 600165), which includes diethylenetriaminepentaacetic acid (DTPA) polymer preloaded with Holmium for conjugation to the antibody. Following labeling, antibodies were diluted in Candor PBS Antibody Stabilization solution (Candor Bioscience GmbH, Wangen, Germany) to 0.2 mg/mL and stored long-term at 4 $^{\circ}$ C.

Cell Culture. Glioblastoma U251-tGFP cells (a misidentified U251 line determined to be genetically identical to U373 by the ATCC; tGFP introduced by lentiviral transfection with multiplicity of 10, generously provided by S. Kumar's Lab) were authenticated by short tandem repeat analysis and tested negative for mycoplasma. The U251-tGFP cells

were maintained in a humidified 37 °C incubator kept at 5% CO₂ with DMEM + Glutamax media (ThermoFisher 10566016) supplemented with 1× MEM nonessential amino acids (11140050, Life Technologies), 1% penicillin/streptomycin (15140122, Invitrogen), 1 mM sodium pyruvate (11360-070, Life Technologies), and 10% Fetal Bovine Serum (FBS, Gemini Bio-Products, 100-106). Cells were detached with 0.05% Trypsin-EDTA (ThermoFisher 25300-120) and resuspended in 4 °C 1× phosphate-buffered saline (PBS, ThermoFisher Scientific 10010023) to generate cell suspensions used for scWB and scIEF.

Single-Cell Western Blots. The scWBs were performed as previously described [11] with a few modifications. The microwell PA gel was created by chemically polymerizing with APS and TEMED an 8%T, 3.3%C, 3 mM BPMAC PA gel precursor solution on an SU-8 mold with microposts (32 μm diameter, ~75 μm height; 1 mm spacing along electrophoretic separation axis, 400 μm spacing between separation lanes) sandwiched to a silanized glass microscope slide. A U251-tGFP cell suspension (~500,000 cells/mL in 1× PBS, 4 °C) was introduced to the PA gel surface, cells were settled by gravity into the microwells (10 min), and excess cells were washed off the gel with PBS. Microwells were visually inspected under brightfield to ensure the majority of wells with cells had single-cell occupancy. Cells were lysed (30 s) within the wells in a 55 °C lysis/electrophoresis buffer (1× RIPA: 0.5% SDS, 0.25% sodium deoxycholate, 0.1% Triton X-100, 0.5× Tris-glycine, as previously reported [11]), and the proteins were electrophoresed into the gel at 40 V/cm (20 s) in a custom electrophoresis chamber. Protein photoimmobilization was induced by application of UV at 100% intensity for 45 s with the Hamamatsu LC8 (Hamamatsu Photonics K.K.). Then, gels were rinsed in TBS-T for 30 min to remove uncaptured species.

Single-Cell Isoelectric Focusing. scIEF under denaturing conditions was performed as previously described [12] with a few modifications. The microwell PA gel was created by chemically polymerizing with APS and TEMED a 6%T, 3.3%C, 3 mM BPMAC PA gel precursor solution on an SU-8 mold with microposts (32 μm diameter, ~50 μm height; single row of microwells positioned at a 2.25 mm distance from the acid region within the 9 mm focusing region, 500 μm spacing between separation lanes) sandwiched to a silanized glass microscope slide. Cell settling was performed as in the scWB. During cell settling, a three-component IEF lid gel was fabricated containing an acidic, focusing, and basic region. Table 2.1 lists the components of the lid gel, which was polymerized for 4 min for each region at 20 mW/cm² light intensity using a 390 nm UV long-pass filter (Edmund Optics) on an OAI model 30 collimated UV light source. The PA gel and lid gel were assembled in the ABS electrophoresis device as previously described [12]. After a 30 s delay for the lysis/focusing reagents in the focusing lid gel to diffuse into the microwell PA gel, IEF was conducted by applying 600 V for 6 min. Then, protein photoimmobilization and gel rinsing were performed as in the scWB.

Immunoprobings. The gels were immunoprobed for tGFP as previously described [16]. Briefly, gels were exposed to 40 μL (scWB) or 12 μL (scIEF) of 33 μg/mL primary rabbit antiGFP antibody in 2% BSA/TBS-T (metal-tagged or untagged, depending on the experiment) for 2 h, washed with TBS-T 2× for 30 min, exposed to 67 μg/mL secondary polyclonal antibody AlexaFluor-647-labeled donkey anti-rabbit in 2% BSA/TBS-T, and washed with

Table 2.1: Composition of IEF lid gel. Components of the 3-part lid gel used for lysis and electrophoresis in the scIEF assay.

Lid gel components	pH 4 anolyte boundary boundary	Focusing region	pH 10 catholyte boundary condition
Polyacrylamide gel	<ul style="list-style-type: none"> • 15 %T • 3.3 %C • 0.2 %VA-086 	<ul style="list-style-type: none"> • 15 %T • 3.3 %C • 0.2 %VA-086 	<ul style="list-style-type: none"> • 15 %T • 3.3 %C • 0.2 %VA-086
IEF reagents and detergents		<ul style="list-style-type: none"> • 1% final ZOOM™ Carrier Ampholytes pH 4-7 • 1% (v/v) TritonX-100 • 3.6% (w/v) CHAPS • 0.0125% (w/v) digitonin • 7 M urea • 2 M thiourea 	
Boundary conditions	<ul style="list-style-type: none"> • 13.6 mM pKa 3.6 immobiline • 6.4 mM pKa 9.3 immobiline 		<ul style="list-style-type: none"> • 5.6 mM pKa 3.6 immobiline • 14.4 mM pKa 9.3 immobiline

TBS-T 2× for 30 min. The gels were then rinsed briefly in DI water to remove salts and gently blow-dried with a nitrogen stream for 1 min before imaging. A gentle nitrogen stream ensures that the integrity of the gel is not damaged.

Fluorescence Microarray Scanner Micrograph Acquisition. Gels were imaged on the GenePix 4300A microarray scanner (Molecular Devices) for expressed tGFP fluorescence with the 488-filter set and immunoprobed fluorescence signal with the 647-filter set.

Confocal Micrograph Acquisition. Confocal imaging was used to measure the tGFP protein depth distribution in scWB protein bands. After scWB, a no. 1.5H glass coverslip (Ibidi 0107999097) was placed on top of the hydrated PA gel and placed coverslip side down onto the microscope stage. Confocal imaging experiments were conducted on an inverted Zeiss LSM 710 AxioObserver at the CRL Molecular Imaging Center. Images were acquired at room temperature using a 40× water immersion objective (LD C-Apochromat 40 × /1.1 NA W Corr M27, Zeiss). tGFP was imaged using a 488 nm laser at 100% power, using the MBS488/561/633 beam splitter and the Zen 2010 software (Zeiss) to collect fluorescence image stacks (field of view: 212.55 μm × 212.55 μm; cubic voxels: 1.66 μm × 1.66 μm × 1.30 μm).

MIBI-TOF Micrograph Acquisition. To increase sample conductivity, the scIEF slide was coated with 15-nm gold (99.999% purity) using a sputter coater. The custom built

MIBI-TOF tissue analyzer was operated as previously described [9].

Profilometry. Gel height was assessed with a Veeco Dektak 8M Stylus Profilometer. The PA gel was dehydrated at the time of measurement.

Image/Micrograph Analysis and Quantitation. scIB micrographs were analyzed using in-house ImageJ and Matlab (R2019b, MathWorks) scripts as previously described [16]. Area under the curve (A.U.C.) fluorescence was calculated by curve-fitting the scWB bands (both the detection antibody and expressed tGFP fluorescence bands) to a Gaussian function and summing the intensity values between four standard deviations of the peak center. A.U.C. was only reported for scWB bands with a Gaussian fit R-squared value >0.7 , for accurate selection of peak boundaries. The signal-to-noise ratio (SNR) for scIB bands was calculated by dividing signal peak height by the standard deviation of the background signal. Statistical analysis was carried out with custom and existing Matlab functions. Analysis of confocal data is described as follows: We calculated a normalized SNR of increasingly summed confocal slices to investigate the relationship between percent of gel depth imaged and SNR, since percent of gel depth imaged is a tunable parameter in MIBI-TOF. With an in-house Matlab script, we performed the following: (1) From each confocal z-stack of a single scIB lane with n slices, we summed slices 1, 1-2, 1-3, 1-4...1- n with slice 1 being the top layer of the gel and slice n being the bottom layer of the gel (gel-microscope slide interface). The result was n images with the first image being just the top layer of the gel and the n th image being the sum of the entirety of the gel over its depth. (2) For each of the n images, we performed background subtraction, Gaussian fitting, and calculated SNR as previously described [16]. Images with protein bands with $\text{SNR} < 3$ were disregarded. (3) Since cell-to-cell variation resulted in large differences in absolute SNR values, we normalized each SNR value by the maximum SNR within the n images for each cell, which allowed improved side-by-side comparison of the biological replicates. Analysis of MIBI-TOF data to produce images of scIEF, including background subtraction and denoising, was performed as previously described [17].

2.4 Results and Discussion

Metal-tagged antibody probes are compatible with in-gel single-cell immunoassays. We first sought to investigate whether and to what extent metal-tagging affects antibody performance in in-gel immunoassays. For mass spectrometry imaging approaches (e.g., MIBI-TOF) the first step is to stain the sample with a panel of metal-tagged probes [18, 19]. Therefore, to use MIBI-TOF as a detection method for single-cell immunoblotting assays such as scWB and scIEF, immunoprobng needs to be performed with metal-tagged primary antibodies instead of the conventional untagged primary and fluorophore-tagged secondary antibody probe duo. We hypothesized that metal-tagging may impact the physiochemical properties of an antibody molecule to the detriment of in-gel immunoassay performance. While previous studies have validated metal-tagged antibodies perform qualitatively similar to untagged antibody probes in fixed tissue [20, 21], the impact metal-tagging has on antibody probe

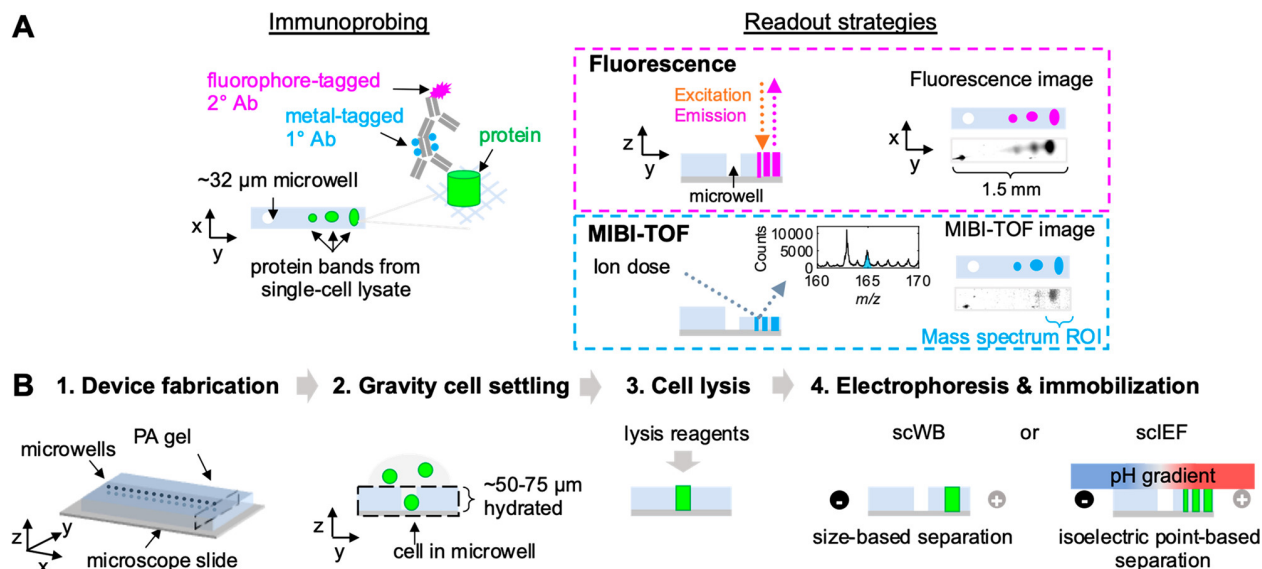


Figure 2.1: scIB-MIBI-TOF combines single-cell protein separation assays with multiplexed mass spectrometry detection. (A) During the immunoprobings step, the scIB sample is incubated with metal-tagged primary antibody (1° Ab), followed by fluorophore-tagged secondary antibody (2° Ab). The scIB sample is then imaged by both fluorescence and MIBI-TOF. In MIBI-TOF inset, mass spectrum is from summed counts from region indicated by the blue brace. (B) scIB is performed via the following steps: (1) microwell patterned PA gel is grafted to a microscope slide, (2) individual cells are settled on the hydrated PA gel matrix, (3) lysis reagents are introduced, and (4) an electric field is applied for electrophoresis and UV light is applied to activate a photoactive moiety in the PA gel backbone in order to covalently attach proteins to the PA gel (immobilization). A lid gel is introduced in scIEF to establish a pH gradient to separate proteins based on isoelectric point differences.

performance in PA gel has not been studied.

To understand the performance of untagged versus metal-tagged anti-tGFP antibodies in scIB, we performed indirect detection of the primary anti-tGFP antibody with a fluorophore-tagged secondary antibody. While fluorescence readout lacks the multiplexing capability of MIBI-TOF, we use fluorescence readout here as validation of immunoprobings of scIB with metal-tagged antibodies (Figure 2.1A). The basic steps of scIB are described in Figure 2.1B. We incubated scWB chips with either untagged rabbit anti-tGFP primary antibody or with Holmium-tagged rabbit anti-tGFP primary antibody (Figure 2.2A). Since the same polymer chemistry can be used for a large swath of metal isotopes, we employed the Holmium-tagged anti-tGFP antibody as the representative metal-tagged antibody. Both the untagged and metal-tagged anti-tGFP antibodies were selective for tGFP in the scWB as indicated by the overlapping protein bands in the intensity plots (Figure 2.2B), suggesting that metal-

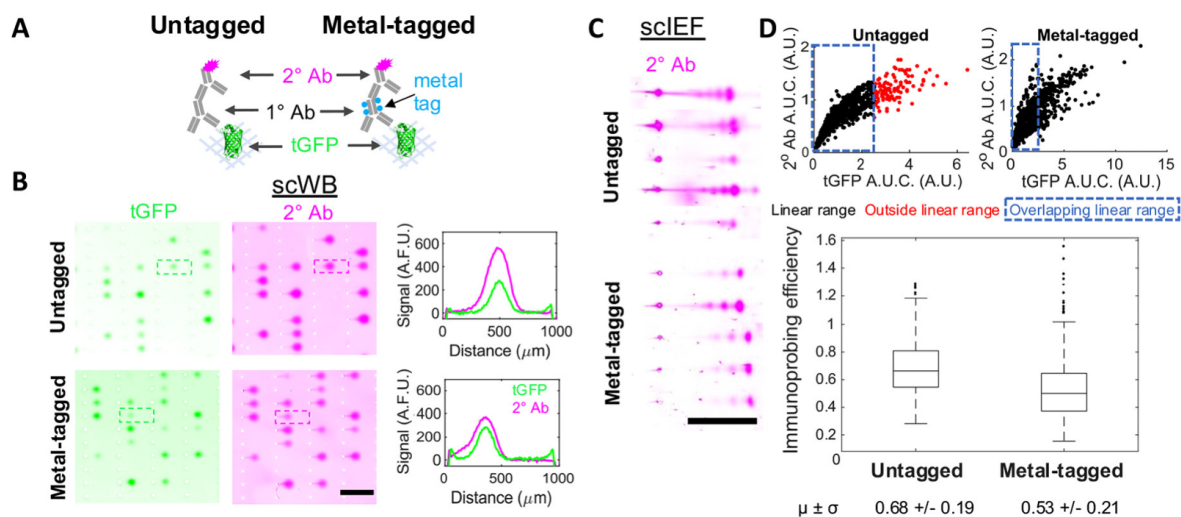


Figure 2.2: Metal-tagged antibody performance in scWB and scIEF. (A) Immunoprobings scheme: tGFP is probed with untagged or metal-tagged primary antibody (1° Ab), followed by a fluorophore-tagged secondary antibody (2° Ab). (B) Fluorescence images and intensity plots of scWBs of U251-tGFP cells. Both expressed tGFP and 2° Ab signal displayed. Scale bar is 1 mm. Micrographs in the same channel have the same acquisition settings, brightness, and contrast (representative micrographs from $n_{\text{Untagged}} = 4, n_{\text{Metal-tagged}} = 4$ independent scWB chips). (C) Fluorescence images of scIEF of U251-tGFP cells probed as in (B). Only 2° Ab signal displayed. Scale bar is 1 mm. Micrographs have the same acquisition settings, brightness, and contrast within each condition but not between the two conditions for better visualization (representative micrographs from $n_{\text{Untagged}} = 2, n_{\text{Metal-tagged}} = 5$ independent scIEF chips). (D) Scatter plots of 2° Ab A.U.C. versus expressed tGFP A.U.C. with the linear data indicated in black, nonlinear data indicated in red, and dashed blue box surrounding overlapping linear data used to generate box plot of immunoprobings efficiency for untagged and metal-tagged configurations. Horizontal line in the boxplot is the median (higher for gels immunoprobed with untagged 1° Ab, MannWhitney U-test p -value < 0.0005), and box edges are at 25th and 75th percentile. Mean and standard deviation of data are displayed below plot. $n_{\text{Untagged}} = 849$ cells, $n_{\text{Metal-tagged}} = 728$ cells from 4 independent scWB chips for each condition.

tagging did not introduce nonspecific binding. We also tested the metal-tagged antibodies in scIEF, where denaturing conditions render the native tGFP signal undetectable, and the metal-tagged antibodies yielded qualitatively similar micrographs of the three tGFP proteoforms versus untagged antibodies (Figure 2.2C), which is aligned with previous work separating tGFP proteoforms with scIEF [12]. Notably, scWB does not resolve the three tGFP proteoforms that are observed with scIEF under denaturing conditions; therefore, tGFP appears as a single protein band in scWB.

We next characterized the relative immunoprobng efficiency of the untagged versus metal-tagged anti-tGFP antibody. Here we define immunoprobng efficiency as the ratio of probed A.U.C. to expressed tGFP A.U.C. We calculated immunoprobng efficiency for protein bands after determining the linear range by using an established approach [22] to exclude high expression protein bands that were in an antibody-limited regime. Using fluorescence microscopy, we measured an immunoprobng efficiency that was 22% lower for the metal-tagged primary antibody configuration, as compared to the untagged primary antibody configuration (reduction in immunoprobng efficiency from 0.68 in untagged to 0.53 for metal-tagged) (Figure 2.2D).

We attribute the slight reduction in immunoprobng efficiency for the metal-tagged antibody configuration to one or a combination of the following effects: (1) reduced primary-target binding efficiency, (2) reduced metal primary antibody partitioning into gel, or (3) reduced primary-secondary binding efficiency. Effect (3) is irrelevant to scIB-MIBI-TOF, as the secondary antibody is only employed here to enable comparison between metal-tagged and untagged primary antibodies; however, MIBI-TOF is typically performed with a cocktail of only metal-tagged primary antibodies. Metals can be conjugated to IgG antibodies using either monomeric or polymeric bifunctional chelating agents (BFCAs) via sulfhydryl chemistry. Polymeric BFCAs (which were what was employed here using the MIBItag Conjugation Kit for metal-tagging) offer superior metal-tagging of antibodies because each repeating unit offers an opportunity to form a complex with a metal ion [23]. However, metal-tagging adds mass to the already bulky antibody probe. Added mass, and therefore a potential increase in hydrodynamic radius, would be expected to exacerbate antibody probe exclusion from the hydrogel (thermodynamic partitioning), thus further reducing the local, in-gel antibody concentration [24, 25] (effect (2)). Moreover, the metal-tag can interfere with the binding of antibody probe to antigen epitope [23] (effect (1)).

Therefore, the 22% reduction represents a worst-case scenario for immunoprobng efficiency for this representative example (8%T 3.3%C PA gel, Holmium-tagging of an antiGFP antibody). For reference, in the stripping and reprobing multiplexing strategy, our group has previously reported a $\sim 75\%$ reduction in antibody signal after one round of stripping [14]. Additionally, the photoactive and hydrophobic moiety used to immobilize proteins in the PA gels after electrophoresis (BPMAC) has been shown to cause non-specific retention of unbound antibody probes [25], which we hypothesized could lead to increased background signal arising from any additional interaction between the metal-tag and the BPMAC. However, the metal-tagged antibody configuration did not increase background signal intensity (Figure 2.3). Additionally, thermodynamic partitioning of antibody into a matrix also depends on the pore size of the gel matrix, which is inversely proportional to the %T of the gel [24]. Accordingly, previous work has shown that there is a 3 orders of magnitude decrease in immunoprobng efficiency in smaller pore-size gels [26], and we hypothesize that this trend will extend to metal-tagged antibody probes as well, meaning larger pore-size gels could be better suited for immunoprobng with metal-tagged probes. Altogether, these results indicate that metal-tagged antibody probes are compatible with detection of protein targets embedded in PA gel. Moreover, the indirect detection of metal-tagged primary antibodies

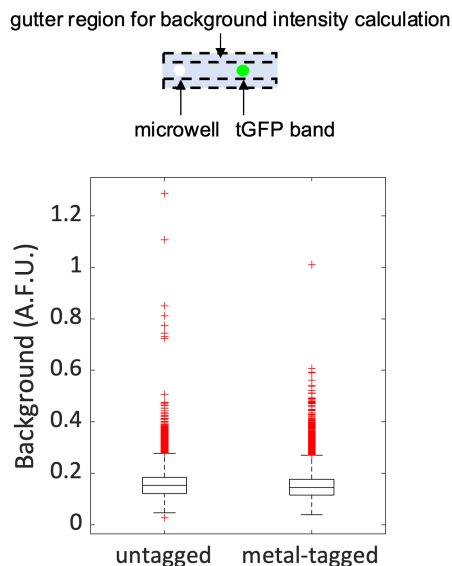


Figure 2.3: Background signal for metal-tagged antibodies. Boxplot of background signal from the same results depicted in Figure 2.2D. Background intensity was calculated from a gutter region of each analyzed ROI chosen as 3-4 standard deviations away from the peak center as depicted in the schematic. Horizontal line in the box is the median (higher for gels immunoprobed with untagged 1° Ab, MannWhitney U-test p-value <0.0005) and box edges are at 25th and 75th percentile. Mean and standard deviation of data is displayed below plot. Difference in background signal in scWB for metal-tagged antibody versus untagged antibody configuration is statistically significant, but small. $n_{\text{Untagged}} = 849$ cells, $n_{\text{Metal-tagged}} = 728$ cells.

with a fluorophore-tagged secondary antibody is a useful strategy to validate metal-tagged probes prior to incorporating the probes for MIBI-TOF detection, since, in any multiplexed assay, it is best practice to independently validate all probes before multiplexing.

Protein signal detected increases with increasing depth imaged. To achieve MIBI-TOF readout of scIB assays, metal atoms from metal-labeled proteins embedded in an $\sim 3.5\text{-}\mu\text{m}$ thick dehydrated PA gel must be ionized for downstream mass spectrometry analysis, since MIBI-TOF is a SIMS instrument [9]. The basis of SIMS is the sputtering process in which the sample is ionized layer-by-layer beginning from the top of the sample to the bottom [27]. Primary ions from an ion source penetrate the sample surface, transferring energy to the sample through a collision cascade, which then causes secondary ions (mono- and polyatomic) to be ejected from the surface, exposing a new surface [15]. Sample imaging requires sustained or repeated bombardment of the sample surface until the desired depth has been ionized and detected [28]. Consequently, MIBI-TOF images thin layers that can be used to reconstruct a final 3D image (analogous to confocal microscopy), whereas conventional

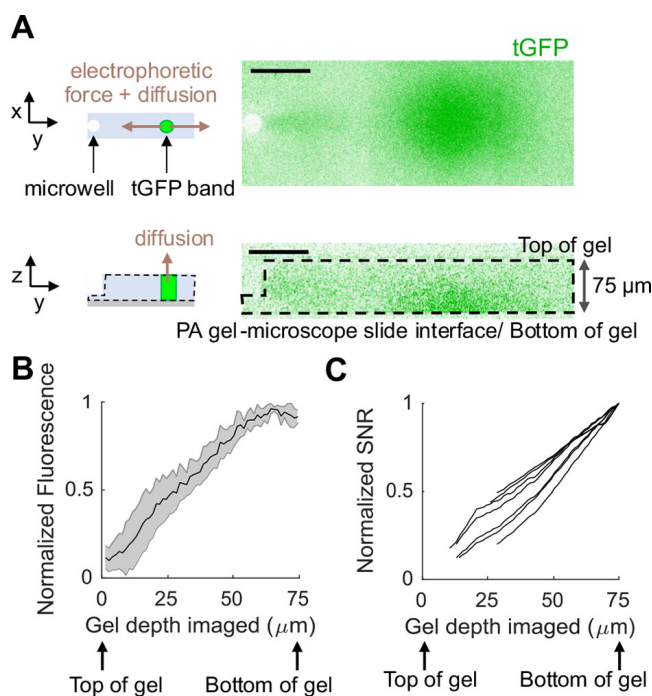


Figure 2.4: Protein signal is concentrated toward the bottom of the PA gel in scIB. (A) Schematics depict the forces acting on protein molecules during electrophoresis. Micrographs are a top (xy) and side (zy) view of a single scWB separation lane of U251-tGFP cells imaged with fluorescence confocal microscopy. tGFP is in green. Scale bar is 100 μm . (B) The plot is the normalized fluorescence intensity after background subtraction of tGFP bands from confocal z-stack images over the gel depth, and shaded error region is standard deviation. (C) Each line in this plot represents the normalized SNR for a single cell as a function of how much percentage of the gel was included in the SNR measurement. For (B) and (C), $n = 7$ cells from 2 independent scWB chips. Cell-to-cell variation resulted in large differences in absolute fluorescence intensity and SNR values, so normalization to the maximum fluorescence intensity and SNR value, respectively, within each cell allowed improved side-by-side comparison of the biological replicates.

fluorescence microarray scanners used to image scIB simultaneously integrate a wide depth of field to generate a single 2D image. Accordingly, for MIBI-TOF of scIB, the sample needs to be treated as a 3D substrate. To that end, we sought to characterize the depth distribution of protein signal in scIB assays to determine the depth at which we could expect to attain the maximum SNR; in other words, what percentage of sample to rasterize for optimal MIBI-TOF detection.

In the conventional MIBI-TOF imaging workflow, only a thin surface layer (~ 200 nm) of the $4\text{-}\mu\text{m}$ thick fixed tissue slice is typically imaged [9, 29]. However, in the scIB system, diffusion during lysis and electrophoresis may dilute protein in scIB samples more than in fixed tissue, so we hypothesized imaging of scIBs would require deeper sample imaging. Though lateral diffusion of protein signal in scIBs has been well characterized [30], the depth distribution of signal in scIB protein bands has only been computationally interrogated [31]. During electrophoresis, the motion of charged molecules in the direction of the electric field is governed by the electrostatic Coulomb force and counteracting viscous drag force [32]. However, the driving force in the z-direction is the concentration gradient, which causes protein loss as proteins diffuse and partition between the PA gel and the fluid and/or gel lid above the device (Figure 2.4A schematics). Based on diffusional loss of protein out of the microwell during cell lysis and out of the PA gel during electrophoresis, we hypothesized that the protein signal will be concentrated toward the PA gel/microscope slide interface (“bottom of the gel”).

To experimentally determine the depth protein concentration in a scIB assay, we directly imaged tGFP bands in a hydrated scWB chip with fluorescence confocal microscopy. Figure 2.4A shows a top view of a tGFP band and the corresponding side view showing the underlying depth protein distribution. As we hypothesized, the tGFP signal is concentrated at the bottom of the gel with protein concentration going to zero at the top of the gel (Figure 2.4B).

We next sought to understand how the depth protein distribution in scIB would impact SNR in MIBI-TOF. To approximate the MIBI-TOF process of sputtering beginning at the top of the gel and sputtering increasing layers, we added increasing numbers of z-stack fluorescence confocal slices and calculated the SNR of the protein band in each summed image (Note S1). By excluding images that yielded $\text{SNR} < 3$ and plotting SNR normalized to the maximum SNR from the series of summed images, we see that the first few layers of the gel are insufficient to yield an SNR greater than 3 and the entirety of gel depth (~ 75 μm) should be imaged to reach the maximum SNR (Figure 2.4C). Since SNR is directly proportional to gel depth imaged, we can anticipate that, to improve the detection of low SNR (low abundance) protein targets with MIBI-TOF (as opposed to the fluorescence confocal microscopy used here), the depth of gel imaged should be as close to the total gel height as possible.

Modulating gel depth rasterized by changing MIBI-TOF ion dose. We next characterized the relationship between depth of PA gel rasterized and ion dose. Ion dose is a function of imaging parameters that can be adjusted in the MIBI-TOF instrument (eq 2.1, $\text{Ion dose} = \text{area normalized ion dose}$, $I = \text{primary ion current}$, $t = \text{acquisition time for a single depth}$,

d = depths acquired, A = field area in mm^2).

$$\text{Ion dose} = \frac{It d}{A} \quad (2.1)$$

Since SIMS is performed in a vacuum chamber, samples for MIBI-TOF are dehydrated before insertion into the instrument (Figure 2.5). Dehydrated scIB gels ($\sim 3.5 \mu\text{m}$) have a similar thickness to the tissue sections ($4 \mu\text{m}$) employed in previous MIBI-TOF studies [9, 17]. The entire depth of a 4-m thick tissue section has been previously imaged with MIBI-TOF [9]. To access the proteins that would be embedded in the $3.5\text{-}\mu\text{m}$ thick scIB chip, we sought to determine the ion dose required to ionize and image various PA gel depths.

Figure 2.6A shows a profilometer trace of MIBI-TOF imaged spots on 6%T PA gel at various ion doses. See Table 2.2 for MIBI-TOF imaging conditions. The depth rasterized was measured using a stylus profilometer which physically drags a stylus across the gel surface to generate a trace of the depth profile. The highest ion dose tested rasterized $\sim 50\%$ of the gel depth with an ion dose of $80 \text{ nA} \times \text{hr}/\text{mm}^2$. We observed a linear relationship between depth rasterized and ion dose (Figure 2.6B, $R^2 = 0.8226$). The sputter yield of individual species increases linearly with applied ion flux [15], so the linear relationship between depth rasterized and ion dose suggests that all species in the PA gel sample are being sputtered at nearly the same rate. Future work will determine whether this constant erosion rate is maintained when imaging the entire $3.5\text{-}\mu\text{m}$ PA gel. Notably, a trade-off between imaging throughput and detection sensitivity is expected because the higher ion dose images (that rasterize deeper into the gel) have the potential to increase SNR (Figure 2.4C) yet require longer acquisition times (eq 2.1).

MIBI-TOF of scIEF resolves tGFP proteoforms from single cells. To validate MIBI-TOF for scIB, we compared MIBI-TOF images to fluorescence images using the same immunoprobng scheme used in Figure 2.2A for the metal-tagged configuration. Figure 2.7A shows

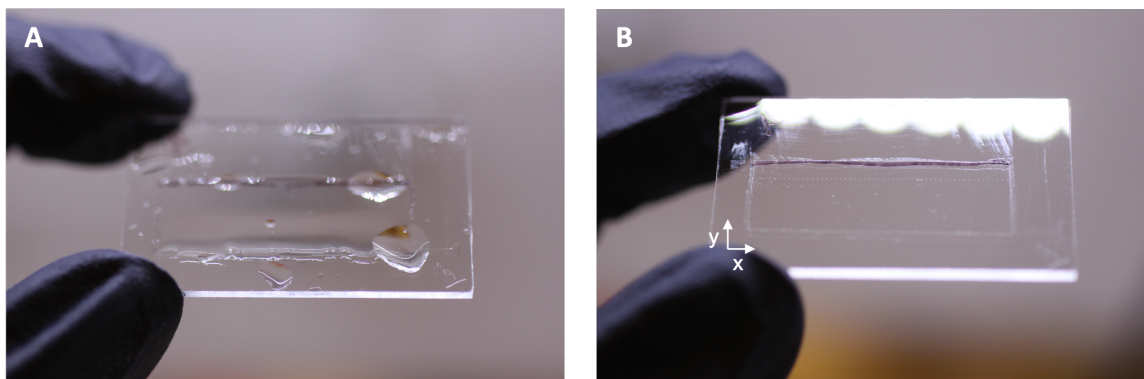


Figure 2.5: PA gel on glass slide is dehydrated before MIBI-TOF. (A) Hydrated scIEF chip on half of a standard microscope slide. (B) Dehydrated scIEF chip. Single row of microwells is visible.

Table 2.2: Imaging conditions and depth rasterized data.

Fig	Current (nA)	FOV size (μm)	Dwell time (ms)	# planes	Pixels	Ion dose/ plane ($\text{nA}\times\text{hr}/\text{mm}^2$)	Ion dose total ($\text{nA}\times\text{hr}/\text{mm}^2$)	Depth rasterized (μm)
2.6B, 2.7	21.9	200	4	1	256	39.87	39.87	1.48
2.6B	21.9	200	4	2	256	39.87	79.74	1.73
2.6B	9.5	400	1	10	256	1.08	10.81	0.13
2.6B	47	400	4	1	256	21.39	21.39	0.44

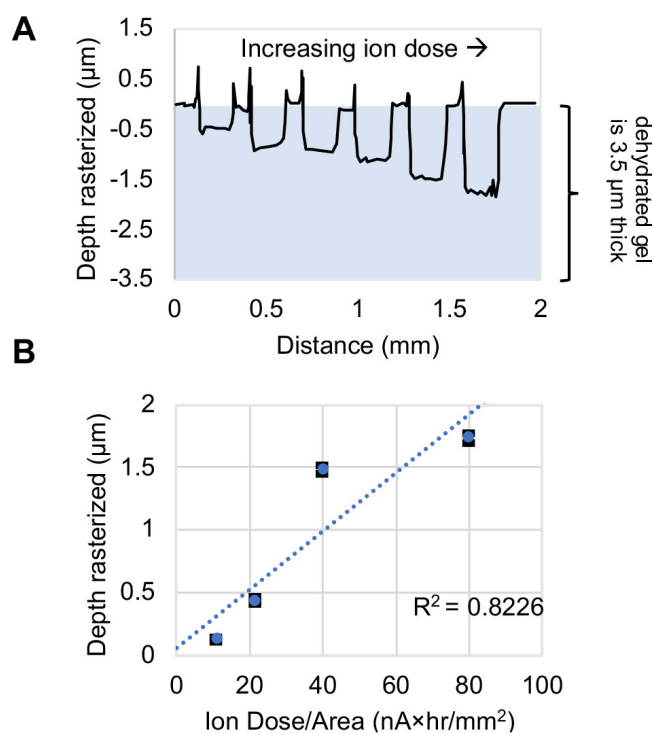


Figure 2.6: PA gel depth rasterized can be tuned by modulating ion dose. (A) Profilometer trace of MIBI-TOF imaged spots with increasing ion dose from left to right. (B) Plot of depth rasterized vs ion dose applied (black error bars are the standard deviation and may be smaller than blue data point symbols, $n \geq 4$ imaged spots per ion dose on same PA gel).

the scIEF images of tGFP proteoforms α , β , and γ , as detected with fluorescence and MIBI-TOF, respectively. See Table 2.2 for MIBI-TOF imaging conditions. The corresponding intensity plots are shown with the overlaid SNR for each protein band, demonstrating that there is an ~ 32 -fold decrease in SNR for MIBI-TOF versus fluorescence imaging. As expected, we observed correlation between fluorescence and MIBI-TOF readouts (Figure 2.7B with colocalized signal in black), but MIBI-TOF was unable to detect the lowest abundance proteoform, γ . However, the ion dose used for the acquisition in Figure 2.7 only rasterized/imaged $\sim 42\%$ of the gel depth; therefore, we hypothesize that MIBI-TOF imaging of the entire gel depth will lead to an ~ 2 -fold improvement in SNR (as suggested by Figure 2.4C).

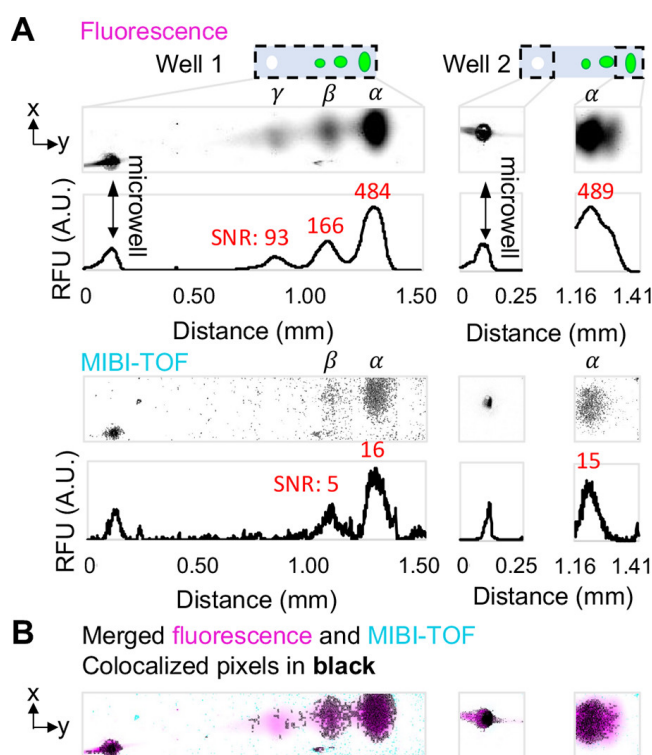


Figure 2.7: MIBI-TOF of scIEF resolves tGFP proteoforms from single cells. (A) Fluorescence vs. MIBI-TOF micrographs and intensity plots of same separated tGFP proteoforms (proteoforms are denoted α , β , and γ) from U251-tGFP cells. SNR for each protein band is indicated in red above its respective intensity plot peak. Well 1 MIBI-TOF image is composed of 8 tiled images of ~ 1 single cell separation. Well 2 MIBI-TOF image is composed of 2 tiled images of ~ 1 single cell separation. (B) Colocalized pixel map of merged images. The x-axis of intensity plots is also the scale bar for micrographs in (B) and (C).

The whole chip fluorescence image was used to identify separation lanes with protein signal for MIBI-TOF imaging to avoid having to scan the whole slide. The acquisition time for

the Well 1 micrograph in Figure 2.7A was ~ 35 min. Removing overlap between imaged tiles results in an acquisition speed of $\sim 1800 \mu\text{m}^2/\text{min}$ for 42% depth rasterized, and assuming depth imaged and ion dose (and therefore acquisition time) have a linear relationship (eq 2.1 and Figure 2.6B), we can estimate an imaging speed of $4200 \mu\text{m}^2/\text{min}$ for 100% depth rasterized which would result in an ~ 1 h acquisition time for a 1-mm separation lane (1 cell/h). Imaging a whole chip, which can contain 100s of single-cell immunoblots, would require a multiday acquisition. Although multiday acquisitions are common for mass spectrometry imaging, there remains opportunity to decrease acquisition time for scIB samples, since even at the lowest resolution settings possible on this MIBI-TOF instrument, the instrument was set up for nanometer-scale tissue analysis. The application here only requires a resolution of 10s of micrometers. As such, we expect a lower resolution instrument configuration would have exponentially higher primary ion beam power, thus be able to sample more gel for better SNR over a shorter period of time. Moreover, there remains avenues of sample preparation optimization to increase substrate conductivity (in addition to or instead of the 15-nm gold coating) and, thus, sensitivity of detection of the secondary reporter ions. Nevertheless, we anticipate there to be a trade-off among multiplexing, imaging speed, and SNR for MIBI-TOF of scIB. Altogether, these results demonstrate successful MIBI-TOF detection of two distinct tGFP proteoforms separated using scIEF, a scIB assay.

2.5 Conclusions

The MIBI-TOF-based single-cell immunoblotting performance reported here forms a promising basis for the extension of MIBI-TOF readouts to other bioanalytical assays and samples where multiplexed detection from a 3D matrix is desirable. In the case of single-cell immunoblotting, by demonstrating the feasibility of MIBI-TOF readout, we increased the amount of theoretically simultaneously available antibody labels from ~ 3 to ~ 40 and eliminated the need to perform antibody stripping and reprobing for multiplexed target detection, including for proteoforms. With additional optimization, scIB-MIBI-TOF is a promising strategy to increase the number of low-abundance targets detected with a simplified experimental workflow.

Importantly, due to the spatial separation between protein bands, we detected two distinct tGFP proteoforms with MIBI-TOF, yet only one metal-tag channel was utilized. Besides the potential ~ 40 channels provided by the distinct metal-tags in MIBI-TOF (if the scIB chip were to be immunoprobed with a cocktail of ~ 40 primary metal-tagged antibodies, as is done for mass spectrometry imaging of tissue samples [9, 33]), scIB provides an additional opportunity to increase the current multiplexing capability of MIBI-TOF by a factor of approximately the peak capacity of the scIB assay. Peak capacity is the number of theoretical protein bands that can “fit” in a separation lane if only one channel was employed, which is ~ 10 for scWB with a 1-mm separation lane [34] and ~ 17 for scIEF with a 9-mm separation lane [12].

Although high parameter single-cell measurement tools increase the complexity of data

analysis, data analysis pipelines for 10s to 1000s of parameters from single cells are rapidly emerging and offer deep insight into how cell composition and functionally relevant markers change with disease [18, 35]. Building on these results, ongoing research is focused on multiplexed detection in additional channels by utilizing additional metal-tagged antibodies during immunoprobng. Looking beyond method innovation, we are interested in studying the role of proteoforms, including truncated HER2 proteoforms and associated proteins, in the context of heterogeneous tumor and immune cell populations to predict drug resistance.

References

- (1) Yang, L.; George, J.; Wang, J. *PROTEOMICS* **2020**, *20*, 1900226.
- (2) Aebersold, R. et al. *Nature Chemical Biology* **2018**, *14*, 206–214.
- (3) Smith, L. M.; Kelleher, N. L. *Nature Methods* **2013**, *10*, 186–187.
- (4) Arribas, J.; Baselga, J.; Pedersen, K.; Parra-Palau, J. L. *Cancer Research* **2011**, *71*, 1515–1519.
- (5) Levy, E.; Slavov, N. *Essays in Biochemistry* **2018**, *62*, 595–605.
- (6) Chattopadhyay, P. K.; Roederer, M. *Methods* **2012**, *57*, 251–258.
- (7) Regnier, F. E.; Kim, J. *Analytical chemistry* **2018**, *90*, 361–373.
- (8) Dickinson, M.; Bearman, G.; Tille, S.; Lansford, R.; Fraser, S. *BioTechniques* **2001**, *31*, 1272–1278.
- (9) Keren, L. et al. *Science Advances* **2019**, *5*, eaax5851.
- (10) Bodenmiller, B. *Cell Systems* **2016**, *2*, 225–238.
- (11) Hughes, A. J.; Spelke, D. P.; Xu, Z.; Kang, C.-C.; Schaffer, D. V.; Herr, A. E. *Nature Methods* **2014**, *11*, 749–755.
- (12) Tentori, A. M.; Yamauchi, K. A.; Herr, A. E. *Angewandte Chemie International Edition* **2016**, *55*, 12431–12435.
- (13) Sinkala, E.; Sollier-Christen, E.; Renier, C.; Rosàs-Canyelles, E.; Che, J.; Heirich, K.; Duncombe, T. A.; Vlassakis, J.; Yamauchi, K. A.; Huang, H.; Jeffrey, S. S.; Herr, A. E. *Nature Communications* **2017**, *8*, 14622.
- (14) Gopal, A.; Herr, A. E. *Scientific Reports* **2019**, *9*, 15389.
- (15) Vickerman, J. C. In *TOF-SIMS: Surface Analysis by Mass Spectrometry*; Manchester and IM Publications: Chichester, 2001, pp 1–40.
- (16) Kang, C.-C.; Yamauchi, K. A.; Vlassakis, J.; Sinkala, E.; Duncombe, T. A.; Herr, A. E. *Nature Protocols* **2016**, *11*, 1508–1530.
- (17) Keren, L.; Bosse, M.; Marquez, D.; Angoshtari, R.; Jain, S.; Varma, S.; Yang, S.-R.; Kurian, A.; Van Valen, D.; West, R.; Bendall, S. C.; Angelo, M. *Cell* **2018**, *174*, 1373–1387.e19.

- (18) Baharlou, H.; Canete, N. P.; Cunningham, A. L.; Harman, A. N.; Patrick, E. *Frontiers in Immunology* **2019**, *10*.
- (19) Yu, Y.; Dang, J.; Liu, X.; Wang, L.; Li, S.; Zhang, T.; Ding, X. *Analytical Chemistry* **2020**, *92*, 6312–6320.
- (20) Angelo, M.; Bendall, S. C.; Finck, R.; Hale, M. B.; Hitzman, C.; Borowsky, A. D.; Levenson, R. M.; Lowe, J. B.; Liu, S. D.; Zhao, S.; Natkunam, Y.; Nolan, G. P. *Nature Medicine* **2014**, *20*, 436–442.
- (21) Rost, S.; Giltneane, J.; Bordeaux, J. M.; Hitzman, C.; Koeppen, H.; Liu, S. D. *Laboratory Investigation* **2017**, *97*, 992–1003.
- (22) Kroll, M. H.; Emancipator, K.; Floering, D.; Tholen, D. *Computers in Biology and Medicine* **1999**, *29*, 289–301.
- (23) Han, G.; Spitzer, M. H.; Bendall, S. C.; Fantl, W. J.; Nolan, G. P. *Nature Protocols* **2018**, *13*, 2121–2148.
- (24) Gehrke, S. H.; Fisher, J. P.; Palasis, M.; Lund, M. E. *Annals of the New York Academy of Sciences* **1997**, *831*, 179–184.
- (25) Su, A.; Smith, B. E.; Herr, A. E. *Analytical Chemistry* **2020**, *92*, 875–883.
- (26) Duncombe, T. A.; Kang, C.-C.; Maity, S.; Ward, T. M.; Pegram, M. D.; Murthy, N.; Herr, A. E. *Advanced Materials* **2016**, *28*, 327–334.
- (27) Nuñez, J.; Renslow, R.; Cliff, J. B.; Anderton, C. R. *Biointerphases* **2017**, *13*, 03B301.
- (28) Walker, A. V. In *Encyclopedia of Spectroscopy and Spectrometry*; Elsevier: 2016, pp 44–49.
- (29) Levenson, R. M.; Borowsky, A. D.; Angelo, M. *Laboratory Investigation* **2015**, *95*, 397–405.
- (30) Tan, K. Y.; Herr, A. E. *Analyst* **2020**, *145*, 3732–3741.
- (31) Rosàs-Canyelles, E.; Dai, T.; Li, S.; E. Herr, A. *Lab on a Chip* **2018**, *18*, 1875–1883.
- (32) Kirby, B. J., *Micro- and Nanoscale Fluid Mechanics: Transport in Microfluidic Devices*; Cambridge University Press: 2010.
- (33) Jackson, H. W.; Fischer, J. R.; Zanutelli, V. R. T.; Ali, H. R.; Mechera, R.; Soysal, S. D.; Moch, H.; Muenst, S.; Varga, Z.; Weber, W. P.; Bodenmiller, B. *Nature* **2020**, *578*, 615–620.
- (34) Yamauchi, K. A.; Herr, A. E. *Microsystems & Nanoengineering* **2017**, *3*, 1–9.
- (35) Yuan, G.-C.; Cai, L.; Elowitz, M.; Enver, T.; Fan, G.; Guo, G.; Irizarry, R.; Kharchenko, P.; Kim, J.; Orkin, S.; Quackenbush, J.; Saadatpour, A.; Schroeder, T.; Shivdasani, R.; Tirosh, I. *Genome Biology* **2017**, *18*, 84.

Chapter 3

Detecting Proteoforms using Isoelectric Focusing in On-Chip Immobilized pH Gradient Gels

3.1 Abstract

Microfluidic analytical tools play an important role in the miniaturization of proteomic assays for increased sensitivity, throughput, and automation. Microfluidic isoelectric focusing (IEF) assays have made it possible to assay proteoforms from low starting cell numbers, yet these often rely on carrier ampholytes (CAs) to establish a pH gradient for protein separation and these CAs have major limitations, including lack of pH gradient tunability and stability (e.g., cathodic drift). Immobilized pH gradient (IPG) gels have been developed to overcome these limitations but efforts to implement IPGs at the microscale have been limited to difficult-to-manufacture glass devices and require proteins to be labeled before analysis, precluding complex samples such as cell lysate. Here, we introduce a polydimethylsiloxane (PDMS)-based IPG microfluidic device (μ IPG) and eliminate cathodic drift at the microscale. We utilize a two-step photopolymerization procedure to create a composite gel with two functions: 1) protein capture for downstream immunoprobing via a photoactive gel component, and 2) IEF protein separation via an IPG gel component. First, we polymerize the photoactive gel in the separation channel. Next, we establish a pH gradient by introducing acidic and basic gel precursors at two reservoirs flanking the separation channel and allow diffusion to establish a linear pH gradient IPG gel. The photoactive gel doubles as a scaffold for the IPG gel, since it prevents fluid flow during gel precursor diffusion. We show that the pH gradient in the PDMS-based μ IPG is stable for at least 30 minutes and resolves proteoforms differing by about 0.1 isoelectric point. Additionally, μ IPG is suitable for analysis of unlabeled, complex samples, which we demonstrate by immunoprobing green fluorescent protein (GFP) from GFP-expressing MCF-7 cells.

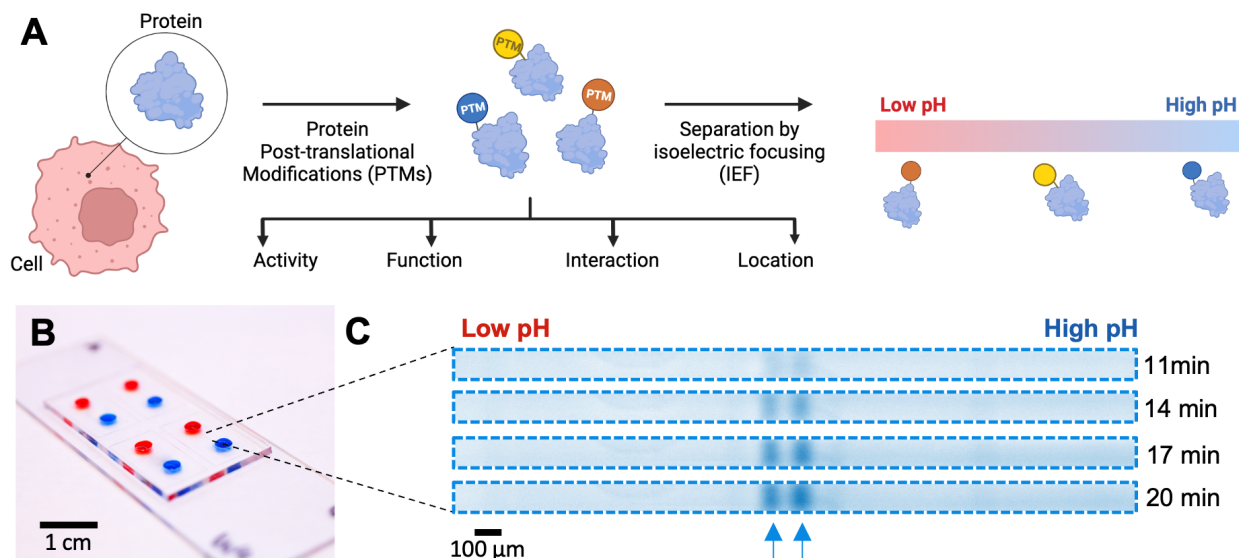


Figure 3.1: μ IPG device enables separation of proteoforms by isoelectric point. (A) IEF can be applied to the analysis of proteoforms. (B) μ IPG device containing food dye-filled microchannels. (C) Inverted fluorescence micrographs of IEF-separated GFP proteoforms at several time points demonstrates pH gradient stability as protein bands remain fixed in position. Micrographs have the same acquisition settings, brightness, and contrast. Representative of $n = 3$ separations.

3.2 Introduction

Isoelectric focusing, or IEF, is a powerful technique capable of effectively distinguishing proteoforms resulting from various post-translational modifications of proteins (Figure 3.1A)[1, 2]. Miniaturization of IEF is necessary for high-throughput analysis of proteoforms with reduced starting sample amounts, as is the case in single-cell studies. Microfluidic IEF has typically been carried out using carrier ampholytes (CAs)[2–4]. CAs are small molecules with both positive and negative charge groups[5]. In CA-IEF, a mixture of CAs placed between an anolyte and catholyte region arrange themselves into a pH gradient under an applied electric field and then the sample proteins migrate to their isoelectric point, pI, in the gradient. Unfortunately, CA-IEF suffers from pH gradient instability and the pH range cannot be easily engineered[5].

A major form of pH gradient instability in CA-IEF is undesired flow in the form of cathodic drift, which is the tendency for molecules to move toward the cathode. Cathodic drift is typically attributed to electroosmotic movement of molecules caused by the slight negative charge of polyacrylamide gels, the typical separation matrix used in IEF[6]. Cathodic drift leads to a multitude of issues during IEF, including loss of separation resolution,

shifts in pH gradient that confound pI value determination, loss of proteins with high pH as they run off the separation lane, and run-to-run variation[3, 5–7]. Previous investigations that have implemented microscale CA-IEF have reported cathodic drift velocities of ~ 10 -600 $\mu\text{m}/\text{min}$ [4, 7–9]. While work has been done to reduce cathodic drift in centimeter-scale slab IEF to a manageable ~ 100 $\mu\text{m}/\text{min}$ [10], cathodic drift in microscale devices is more pronounced relative to the characteristic length- (micrometers) and time-scales (minutes) for IEF separation[11]. Overall, cathodic drift poses challenges to the reliability, accuracy, and reproducibility of IEF, underscoring the need to minimize or eliminate its effects for optimal separation and analysis of proteoforms in microscale devices.

Another class of IEF employs immobilized pH gradient (IPG) gels in which a pH gradient is already established before sample application by polymerizing Immobilines into the polyacrylamide (PA) gel. Immobilines are small molecules containing either a carboxyl or tertiary amino group that buffer the gel to a different pH. Since the Immobilines are fixed in position, IEF performed with IPG gels does not suffer from cathodic drift, unlike CA-IEF[5]. Moreover, by creating a gradient in Immobiline concentrations across a gel, a highly tunable pH gradient is created. Tunability is key, since a broad pH range might be desired in a multiplexed study with various proteins, while a narrow pH range increases the minimum resolvable pI difference and can be used to separate proteoforms close in pI[5]. Since the pH gradient is immobilized, drift of protein bands towards the cathode is abolished and the protein band position is reproducible[5, 12]. Additionally, there is a class of IEF called mixed-bed CA-IPG IEF. In mixed-bed CA-IPG IEF, a primary, stationary, Immobiline-driven pH gradient coexists with a secondary, soluble, CA driven pH gradient[13]. Mixed-bed IEF does not suffer from cathodic drift, making mixed-bed IEF an effective method to combine the advantages of both CA- and IPG-IEF[5].

An IPG microfluidic device was previously reported, introducing the term μIPG , but it was fabricated in glass microchannels[14]. While glass microfluidic devices have seen commercial success[15], they typically require complex and time-consuming fabrication processes, such as photolithography and etching, which are less accessible to researchers without specialized facilities[16, 17]. Moreover, the sample proteins had to be pre-labeled with dye for detection. Protein staining of the glass-based μIPG was challenging, since the μIPG was only accessible at the two ends of the microchannel. A CA-based microfluidic device employed electrophoretic immunoprobings for protein readout[4]. In this device, proteins were photocaptured to the PA gel by incorporating a photoactive moiety in the PA backbone. Uncaptured protein species and CAs were electrophoretically washed from the microchannel, and then antibodies were electrophoretically introduced into the microchannel. Electrophoretic immunoprobings of a μIPG device would be challenging, since the pH gradient cannot be easily washed away and it can be anticipated that antibodies would focus in the IPG, like any other protein sample, and make it challenging to expose the whole length the microchannel to the immunoprobes. Immunoprobings via diffusion may also be used to introduce immunoprobes to microscale electrophoretic separations, yet diffusive immunoprobings is best suited when immunoprobes must only traverse 10s of microns (as is the case in single-cell immunoblots[18]) instead of 1000s of microns thick (as is the case in μIPG [14]),

since diffusion of a bulky antibody probe across a millimeter length scale can take multiple days[19], and would therefore be impractical.

The μ IPG device presented here is made with PDMS. PDMS is a soft, elastomeric material that is flexible and can be easily molded or patterned using standard soft lithography techniques[16]. PDMS is a highly ubiquitous material in microfluidics for its favorable properties, including cost-effective prototyping and biocompatibility[20]. Our PDMS-based μ IPG device is fabricated with a similar robust Immobiline chemistry employed by centimeter-scale commercial IPG strips. We introduce a photoactive hydrogel overlaid on the IPG hydrogel to covalently immobilize proteins so that captured proteins can be immunoprobed and read out via immunofluorescence. To overcome the challenge of electrophoretic probing in an IPG, the PDMS is reversibly attached to a glass support so that the μ IPG can be exposed for diffusive immunoprobing. We investigate the performance of our μ IPG device using a cocktail of pI markers and perform isoelectric focusing and immunoprobing of cell lysate.

3.3 Materials and Methods

Device Assembly. The μ IPG device was fabricated by standard soft lithography methods. A silicon wafer (WaferPro C04009) was patterned with SU8 3050 photoresist (MicroChem Y311075) using in-house-designed masks (CAD/ART Services) to create the silicon wafer mold and coated with dichlorodimethylsilane (Sigma 440272) to prevent PDMS from sticking to the SU8 features. RTV615 PDMS (Momentive) was mixed at a 10:1 ratio, degassed for 2 hours under vacuum, and poured over the silicon wafer mold of the microchannel features. Each microchannel is 3.5-mm long, 100- μ m wide, and 50- μ m tall. After the PDMS was cured at 80 °C for 2 hours, a biopsy punch was used to make 3-mm diameter inlet and outlet holes for each microchannel. The PDMS slab was cleaned of any dust and debris by sticking and peeling tape to the patterned surface multiple times, and then immediately assembled onto a standard glass slide (VWR 48300-048). Since only light pressure will be applied to the microchannels in subsequent steps, the noncovalent interaction is sufficient to hold the PDMS onto the glass slide during device fabrication and operation, while letting the bond between the PDMS and the glass be reversible for subsequent delamination of the PDMS from the glass for immunoprobing, as previously described[17]. Therefore, we did not perform plasma bonding of the PDMS to glass as is standard in soft lithography. We then apply Kapton tape (Electron Microscopy Sciences 77708-02) on the other side of the glass slide to cover the inlet and outlet holes to serve as a photomask and prevent photopolymerization in those regions.

Gel Fabrication. The next step is to polymerize PA gel in the PDMS channels. Since PA polymerization is oxygen inhibited and PDMS is known to absorb oxygen, the microchannels are first prepped for PA polymerization by adding 10 μ L of a 10% benzophenone in acetone solution to each inlet and outlet and allowing the benzophenone solution to permeate the PDMS for 3 minutes. Benzophenone serves as an oxygen scavenger when exposed to UV[17]. To prevent benzophenone crystals from forming in the microchannel, the inlet and outlet

benzophenone solution is wicked with a Kimwipe and replaced with 10 μL methanol (VWR BDH1135). The methanol is then wicked and a gentle nitrogen stream at one of the inlets is used to dry the microchannels. The methanol rinse and nitrogen drying is repeated one more time.

As shown in Figure 3.3Aii, 10 μL of a 6 %T PA gel precursor made from 30 %T 29:1 acrylamide/bis-acrylamide (Sigma A3574), the photo-active moiety N-[3-[(3-benzoylphenyl)-formamido]propyl] methacrylamide (BPMAC, custom synthesized by PharmAgra Laboratories), and UV photoinitiator 2,2-Azobis(2-methyl-N-(2-hydroxyethyl) propionamide) (VA086, Wako Chemicals 01319342) is then applied at one of the inlets. Since the benzophenone treatment renders the microchannel hydrophobic, we apply gentle suction at the opposite inlet using a pipette tip to promote the PA gel precursor to fill the microchannel. Table 3.1 lists all PA gel precursor recipes. All PA gel precursors are prepared in deionized water provided by an Ultrapure Millipore filtration system (18.2 M Ω).

The PA gel precursor is then photopolymerized with 2 minutes of UV light exposure at 20 mW/cm² (Figure 3.3Aiii). An OAI Model 200 Collimated UV light source provides the UV light exposure for gel photopolymerization. The UV activates both the benzophenone (oxygen scavenger) and the VA-086 photoinitiator (radical polymerization initiator). The inlets were then emptied and filled with 6 %T or 12 %T PA acidic (pH = 3.8) and basic (pH = 7.0) precursors containing acrylamide/bis-acrylamide, Immobilines, and VA-086 (Figure 3.3Aiv-v) (Table 3.1). Immobilines used were acrylamido buffers pKa 3.6 (\sim 0.2 M in water, Sigma 01716), pKa 4.6 (\sim 0.2 M in water, Sigma 01718), pKa 6.2 (\sim 0.2 M in 1-propanol, Sigma 01721), pKa 7.0 (\sim 0.2 M in 1-propanol, Sigma 01729), and pKa 9.3 (\sim 0.2 M in 1-propanol, Sigma 01738). The acidic and basic IPG precursor recipes were adapted from previous work[14]. The precursors were allowed to diffuse into the microchannels for 7 hours to establish a linear concentration gradient. During this step, the preexisting 6 %T PA gel serves as a scaffold for the IPG gel, since it prevents fluid flow during gel precursor diffusion[14]. The IPG precursor was then photopolymerized with 2 minutes of UV light exposure at 20 mW/cm² (Figure 3.3Avi-viii). The Kapton tape photomask is then removed from the bottom of the glass slide. The devices were then incubated in deionized water (for IPG-only IEF) or sample loading buffer (for mixed-bed CA-IEF) overnight and could be stored at 4 $^{\circ}\text{C}$ in deionized water or sample loading buffer for at least 9 days. The sample loading buffer consisted of 1% ZOOM Carrier Ampholytes pH 4 to 7 (Thermo Fischer Scientific ZM0022), 3% 3-[(3-Cholamidopropyl)dimethylammonio]-1-propanesulfonate (CHAPS, Sigma RES1300C), 10% D-sorbitol (Sigma S6021), and 200 mM nondetergent sulfobetaine-256 (Abcam ab142233) in deionized water.

Gradient Formation and Polymerization Experiments. To determine how much time is necessary to establish a linear Immobililine concentration gradient within the microchannel via diffusion (Figure 3.3Avi), we monitored the diffusion of Nile Blue acrylamide (NB) within the microchannel. NB was used as a proxy for Immobililine chemicals since it has a similar molecular weight and would therefore be expected to diffuse through the PA gels at a similar time scale. For the diffusion experiment in Figure 3.3C-D, NB was spiked into the acidic gel precursor at a concentration of 17.4 μM .

Table 3.1: Recipes of PA gel precursors.

6 %T scaffold gel precursor	<ul style="list-style-type: none"> • 6 %T, 3.3 %C acrylamide/bis-acrylamide • 0.5 %VA-086 • 3 mM BPMAC
6 %T gel precursor for CA-IEF	<ul style="list-style-type: none"> • 6 %T, 3.3 %C acrylamide/bis-acrylamide • 0.5 %VA-086
6 %T pH 3.8 gel precursor	<ul style="list-style-type: none"> • 6 %T, 3.3 %C acrylamide/bis-acrylamide • 0.5 %VA-086 • 12.7 mM pKa 3.6 Immobiline • 7.48 mM pKa 6.2 Immobiline
12 %T pH 3.8 gel precursor	<ul style="list-style-type: none"> • 12 %T, 3.3 %C acrylamide/bis-acrylamide • 1 %VA-086 • 12.7 mM pKa 3.6 Immobiline • 7.48 mM pKa 6.2 Immobiline
6 %T pH 7.0 gel precursor	<ul style="list-style-type: none"> • 6 %T, 3.3 %C acrylamide/bis-acrylamide • 0.5 %VA-086 • 4.40 mM pKa 3.6 Immobiline • 10.3 mM pKa 4.6 Immobiline • 2.36 mM pKa 6.2 Immobiline • 4.17 mM pKa 7.0 Immobiline • 12.1 mM pKa 9.3 Immobiline
12 %T pH 7.0 gel precursor	<ul style="list-style-type: none"> • 12 %T, 3.3 %C acrylamide/bis-acrylamide • 1 %VA-086 • 4.40 mM pKa 3.6 Immobiline • 10.3 mM pKa 4.6 Immobiline • 2.36 mM pKa 6.2 Immobiline • 4.17 mM pKa 7.0 Immobiline • 12.1 mM pKa 9.3 Immobiline

For the polymerization test experiment in Figure 3.2A, AlexaFluor-647-labeled donkey anti-rabbit antibody (Invitrogen A-31573) was spiked into the scaffold, acidic, and basic gel precursors at a concentration of 0.01 mg/mL. For the polymerization experiment, the antibody simply served as a large molecular weight dye. For the polymerization test experiment in Figure 3.2B, NB was spiked into the gel precursors at a concentration of 17.4 μ M.

Cell Culture and Cell Lysate Preparation. An MCF7 human breast cancer cell line genetically modified to stably express enhanced green fluorescent protein (GFP) was obtained from the American Type Culture Collection, authenticated by short tandem repeat analysis, and tested negative for mycoplasma. The MCF7-GFP cells were maintained in a humidified 37 °C incubator kept at 5% CO₂ with RPMI media (Gibco 11875-093) supplemented with 1% penicillin/streptomycin (Invitrogen 15140122) and 10% Fetal Bovine Serum (FBS,

Gemini Bio-Products 100-106).

A T75 flask with MCF7 cells at 80% confluency was used to prepare cell lysate. Cell lysate preparation was performed as previously described[4] with some modifications. Cells were detached with 0.05% Trypsin-EDTA (ThermoFisher 25300-120), resuspended in 4 °C 1× phosphate-buffered saline (PBS, Thermo Fisher Scientific 10010023), and counted with a phase counting chamber (Hausser Scientific 3200). The cell suspension was pelleted, the PBS was removed, and the cell pellet was resuspended in HNTG buffer for a final concentration of 20,000 cells/ μL HNTG buffer. HNTG buffer was prepared with 20 mM HEPES pH 7.5 (Sigma H-9897), 25 mM NaCl (Fisher S271), 0.1% Triton X-100 (Sigma X100), 10% glycerol (Sigma G7893), and 1X cOmplete™ EDTA-free Protease Inhibitor Cocktail (Sigma COEDTAF-RO) in deionized water. The cells were allowed to lyse in the HNTG buffer for 30 minutes on ice with vortexing every 5 minutes. Finally, the samples were clarified by centrifugation at 16,000 \times g for 10 min at 4 °C, the lysate supernatant was collected, and 50 μL aliquots were stored at -80 °C.

Isoelectric Focusing Experiments. Fluorescent pI markers (pI 4.5, Sigma 89149; pI 5.5, Sigma 77866; pI 5.9, Sigma 89478; pI 6.6, Sigma 73376; pI 6.7, Sigma 73938) were used at a various concentrations to provide similar peak intensities and were diluted in deionized water or sample loading buffer. We also tested fluorescent pI marker 4.0 (Sigma 89827), but this pI marker was excluded from analysis since it was difficult to accurately identify a peak center (data not shown). For all experiments, the anode inlet was filled with 1X IEF Anode Buffer (Bio-Rad 1610761) and the cathode inlet was filled with 1X IEF Cathode Buffer (Bio-Rad 1610762). For cell lysate experiments, 1 μL of MCF7-GFP cell lysate (\sim 20,000 cells) was applied to the cathode inlet, as well as pI markers in sample loading buffer. Table 3.2 lists the anode inlet and cathode inlet sample components for all isoelectric focusing experiments.

The inlets were connected to a programmable high voltage power supply, LabSmith HVS448LC 3000V High Voltage Sequencer, with platinum electrodes. An electric field was applied using the following voltage ramp: 50 V/cm for 4 minutes, 100 V/cm for 5 minutes, 200 V/cm for 5 minutes, and 300 V/cm for 6 minutes or more depending on the experiment. For immunoprobings experiments, the electric field was turned off and the photoactive IPG gel was immediately irradiated by UV light at 100% intensity for 45 seconds with the Hamamatsu LC8 Spot Light Source in order to photocapture proteins, including GFP.

Immunoprobings. To expose the IPG gel inside of the μIPG device for immunoprobings, the PDMS was gently peeled from the glass slide. Since the PA gel is covalently bonded to the PDMS and not the glass slide, the IPG gel was retained on the PDMS layer. In some devices, the IPG gel stuck to the glass slide in which case the separation was not immunoprobed for analysis. After delamination, the PDMS containing IPG gel was rinsed in Tris-buffered saline with Tween-20 (TBS-T, Cell Signaling Technologies 9997S) for 30 min to remove uncaptured species and blocked in 2% bovine serum albumin (BSA, Sigma-Aldrich A7030) in TBS-T for 30 min. The gels were immunoprobed for GFP as previously described[21]. Each IPG gel was incubated in 20 μL of 110 $\mu\text{g}/\text{mL}$ primary polyclonal goat anti-GFP antibody (Abcam ab6673) in 2% BSA/TBS-T for 2 h, washed with TBS-T 2 \times for 30 min, exposed to 67 $\mu\text{g}/\text{mL}$ secondary polyclonal AlexaFluor™ 555-labeled donkey anti-

Table 3.2: Anode inlet and cathode inlet sample components for all isoelectric focusing experiments.

Figure	IPG %T	Anode Inlet Sample Components	Cathode Inlet Sample Components
3.1C	6	<ul style="list-style-type: none"> • 7.5 μL of pI 4.5 marker (10 $\mu\text{g}/\text{mL}$), pI 5.5 marker (30 $\mu\text{g}/\text{mL}$), and pI 5.9 marker (20 $\mu\text{g}/\text{mL}$) in sample loading buffer • 1 μL cell lysate ($\sim 20,000$ cells) • 6.5 μL DI water • 1.5 μL Anode Buffer 	<ul style="list-style-type: none"> • 7.5 μL sample loading buffer • 1 μL cell lysate ($\sim 20,000$ cells) • 6.5 μL DI water • 1.5 μL Cathode Buffer
3.4	6	<ul style="list-style-type: none"> • 5 μL of pI 4.5 marker (10 $\mu\text{g}/\text{mL}$), pI 5.5 marker (30 $\mu\text{g}/\text{mL}$), pI 5.9 marker (20 $\mu\text{g}/\text{mL}$), pI 6.6 marker (20 $\mu\text{g}/\text{mL}$), and pI 6.7 marker (20 $\mu\text{g}/\text{mL}$) in DI water • 1.5 μL Anode Buffer 	<ul style="list-style-type: none"> • 15 μL DI water • 1.5 μL Cathode Buffer
3.5	6	<ul style="list-style-type: none"> • 5 μL of pI 4.5 marker (10 $\mu\text{g}/\text{mL}$), pI 5.5 marker (30 $\mu\text{g}/\text{mL}$), pI 5.9 marker (20 $\mu\text{g}/\text{mL}$), in DI water • 1.5 μL Anode Buffer 	<ul style="list-style-type: none"> • 15 μL DI water • 1.5 μL Cathode Buffer
3.6 3.8	6	<ul style="list-style-type: none"> • 7.5 μL of pI 4.5 marker (10 $\mu\text{g}/\text{mL}$), pI 5.5 marker (30 $\mu\text{g}/\text{mL}$), and pI 5.9 marker (20 $\mu\text{g}/\text{mL}$) in sample loading buffer • 1 μL cell lysate ($\sim 20,000$ cells) • 6.5 μL DI water • 1.5 μL Anode Buffer 	<ul style="list-style-type: none"> • 7.5 μL sample loading buffer • 1 μL cell lysate ($\sim 20,000$ cells) • 6.5 μL DI water • 1.5 μL Cathode Buffer

goat antibody (Invitrogen A-21432) in 2% BSA/TBS-T, and washed with TBS-T $2\times$ for 30 min. The gels were then rinsed briefly in DI water to remove salts mounted on a no. 1.5H glass coverslip (Ibidi 0107999097) before imaging.

Fluorescence Imaging. Nile Blue acrylamide diffusion experiments (Figures 3.3C-D) were imaged using an Olympus IX71 inverted epifluorescence microscope equipped with an Andor iXon + EMCCD camera, ASI motorized stage, and X-cite exacte illumination system from Lumen Dynamics. All IEF experiments were imaged using an Olympus IX-51 inverted epifluorescence microscope equipped with a Peltier-cooled CCD camera CoolSNAP HQ2 (Roper Scientific), ASI motorized stage, and X-cite exacte illumination system from Lumen Dynamics. The polymerization experiments (Figure 3.2), delamination experiment (Figure 3.7), and immunoprobed gels (Figure 3.8) were imaged on the GenePix 4300A microarray scanner (Molecular Devices).

Image/Micrograph Analysis. Fluorescence micrographs were analyzed using in-house ImageJ and MATLAB (R2022b, MathWorks) scripts. Illumination correction for fluorescence micrographs was performed with the BaSiC plugin for ImageJ 1.54f (NIH). Intensity profiles were generated by summing across the width of the microchannel. Peak centers were calculated by curve-fitting the IEF peaks (both the pI marker and GFP peaks) from the intensity profiles to a Gaussian function.

3.4 Results and Discussion

Design of μ IPG for Isoelectric Focusing and Immunoblotting. The μ IPG device presented here holds 4 separation lanes on a standard microscope slide (Figure 3.1B). Loaded analytes migrate along the pre-established pH gradient (μ IPG) within the separation lane until they reach net zero charge (Figure 3.1C). Figure 3.3A provides details on the two-step photopolymerization process of PA gel precursors to form the μ IPG. Steps i-iv establish a photoactive scaffold gel within the PDMS microchannel, while steps v-viii serve to overlay the IPG onto the PA scaffold through diffusion, creating a composite hydrogel/interpenetrating network (Figure 3.3B). The scaffold gel serves two purposes: firstly, it prevents fluid flow and enables the establishment of a linear gradient in steps v-viii[14]; secondly, the scaffold gel contains a photoactive moiety for downstream in-gel immunoprobing[4]. UV irradiation is used in both photopolymerization steps for two reasons: it activates the benzophenone absorbed by the PDMS to quench oxygen and graft the PA gel to the PDMS[22]; and it activates the photoinitiator, VA-086, in the gel precursors to initiate radical PA polymerization. We confirmed that all precursors polymerized in the PDMS channel and that both UV irradiation and benzophenone were necessary for polymerization (Figure 3.2). Overall, we leverage the ease with which polyacrylamide forms copolymers to create a μ IPG gel capable of both IEF and immunoblotting. Furthermore, we overcome the challenge of performing radical chemistry in PDMS by utilizing an oxygen scavenger[22].

Establishing a Linear Gradient. We first sought to establish a linear Immobiline concentration gradient within the μ IPG microchannel, which in turn establishes a linear pH

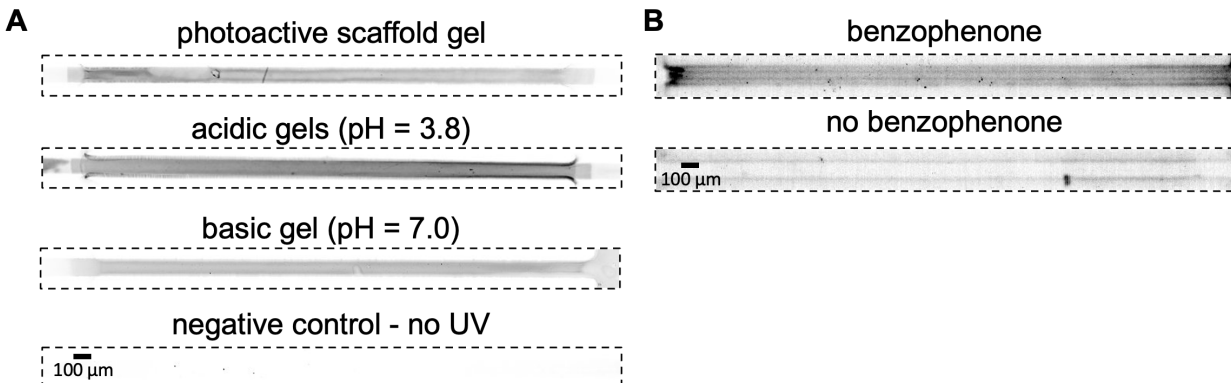


Figure 3.2: Both UV irradiation and the benzophenone coating are necessary for PA gel polymerization in the PDMS device. (A) Confirmation of UV photopolymerization of PA gel precursors individually in microchannels ($n = 1$ gel). Precursors were spiked with 0.01 mg/mL AlexaFluor-647-labeled antibody to make the PA gel fluorescent. (B) PA gel did not polymerize without benzophenone coating ($n = 2$ gels). Precursors were spiked with 17.4 μ M Nile Blue acrylamide to make the PA gel fluorescent. (A-B) Micrographs have the same acquisition settings, brightness, and contrast within panels.

gradient. IPG pH gradients are highly tunable, including the option to form a linear or nonlinear gradient. A linear pH gradient provides a more predictable separation of proteins based on their isoelectric points compared to nonlinear pH gradients. A nonlinear pH gradient may be desired to create regions of narrow pH to analyze complex protein mixtures[23]. To demonstrate the feasibility of IPG-IEF in a PDMS device, the present work focuses on linear pH gradients.

To determine the amount of diffusion time necessary to establish a linear gradient of IPG gel precursor molecules within a microchannel prefilled with 6 %T PA scaffold gel, we modeled the diffusion behavior of a proxy molecule, Nile Blue acrylamide (Figure 3.3C). We calculated diffusion for Nile Blue acrylamide dye ($MW = 408 \text{ g mol}^{-1}$) since it has a larger molecular weight than all the individual molecules of the IPG gel precursors and we can therefore assume it will have a similar or slower diffusion rate than the IPG gel precursor molecules we want to model.

To calculate the diffusion coefficient of Nile Blue acrylamide in PA gel, we used the universal equation for probe diffusion in PA gels (eq 3.1) described by Park *et al.* where D is the diffusion coefficient of the molecule in the gel (m^2/s), D_0 is the diffusion coefficient of the molecule in the pure solvent (m^2/s), R_h is the hydrodynamic radius of the molecule (\AA), and C is the acrylamide concentration (g/mL)[24].

$$\frac{D}{D_0} = \exp(-3.03R_h^{0.59}C^{0.94}) \quad (3.1)$$

To calculate D_0 and R_h for Nile Blue acrylamide and solve for D , we used the following equations (eq 3.2, eq 3.3, and eq 3.4) described by Evans *et al.*, which are based on the Stokes-Einstein equation but allows D_0 to be estimated from molecular weight[25]. In eq 3.2, eq 3.3, and eq 3.4, k_B is the Boltzmann constant (1.38×10^{-23} m²kg/s²K), T is temperature (K), η is viscosity of the solvent (kg/ms), MW is the molecular weight of the molecule (g/mol), MW_s is the molecular weight of the solvent (g/mol), ρ_{eff} is the effective density of the solvent (g/m³), N_A is the Avogadro number (6.022×10^{23} mol⁻¹), and Pa is the packing fraction of the material (0.64 if a liquid).

$$D_0 = \frac{k_B T \left(\frac{3\alpha}{2} + \frac{1}{1+\alpha} \right)}{6\pi\eta \sqrt[3]{\frac{3MW}{4\pi\rho_{eff}N_A}}} \quad (3.2)$$

$$\alpha = \sqrt[3]{\frac{MW_s}{MW}} \quad (3.3)$$

$$R_h = \sqrt[3]{\frac{3PaMW}{4\pi\rho_{eff}N_A}} \quad (3.4)$$

If we solve for Nile Blue acrylamide diffusion in a 6 %T PA gel, where water is the solvent, we arrive at $D = 2.7 \times 10^{-10}$ m²/s or 0.0162 mm²/min.

Next, the concentration profile of Nile Blue acrylamide in the microchannel was modeled with the 1-D Diffusion equation:

$$\frac{\partial u}{\partial t} = D \frac{\partial^2 u}{\partial x^2} \quad (3.5)$$

where D is the diffusion coefficient of Nile Blue acrylamide (0.0162 mm²/min), x is the spatial coordinate in millimeters, t is time in minutes, and u is the concentration in micromolar. The initial condition is:

$$u(x, 0) = 0, \quad 0 < x < L \quad (3.6)$$

where L is the length of the microchannel (3.5 mm). The boundary conditions are:

$$u(0, t) = 0, \quad u(L, t) = U, \quad t > 0 \quad (3.7)$$

where U is the concentration of Nile Blue acrylamide in the reservoir (17.4 μM). Applying the technique of separation of variables leads to the analytical solution[26]:

$$u(x, t) = U \frac{x}{L} - \frac{2U}{\pi} \sum_{n=1}^{\infty} \frac{1}{n} \exp(-n^2 \pi^2 \frac{Dt}{L^2}) \sin[n\pi(1 - \frac{x}{L})] \quad (3.8)$$

Eq 3.8 was evaluated every minute from $t = 0$ minutes to $t = 500$ minutes. Finally, the linearity (R^2) of the resulting concentration profiles at each time point was used to plot linearity in Figure 3.3C. We compared the modeling results to experimental results and

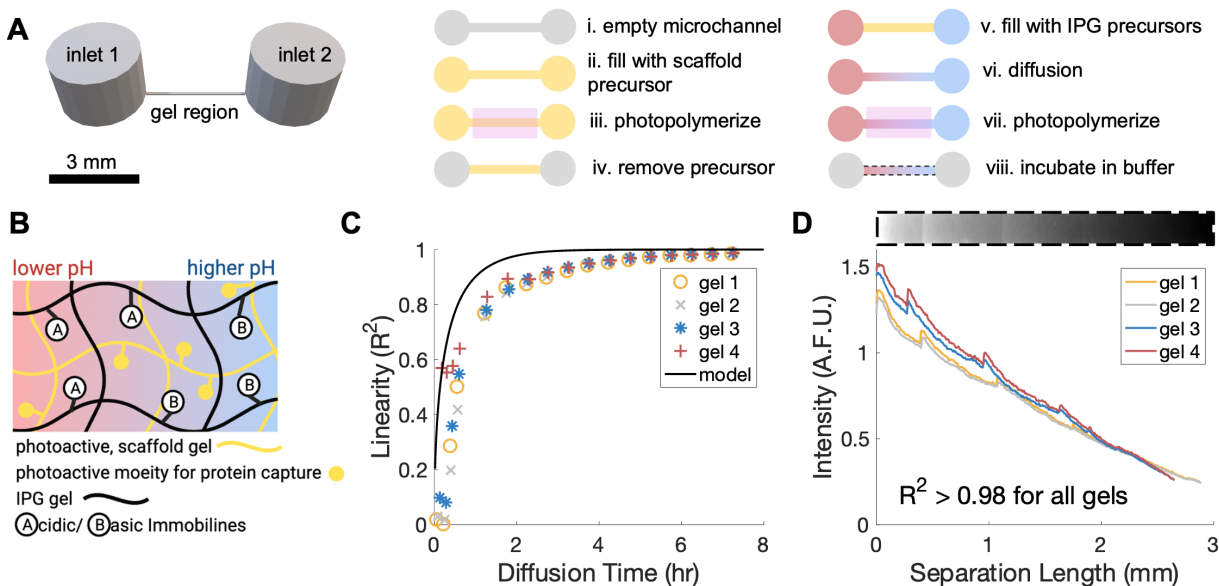


Figure 3.3: Concept and fabrication of the μ IPG device. (A) μ IPG device fabrication protocol using a double photopolymerization method. (B) Schematic of μ IPG gel composition. IPG PA gel is overlaid on photoactive, scaffold PA gel. (C) Linearity of gradient during diffusion step is modeled and experimentally monitored ($n = 4$ gels) with Nile Blue acrylamide dye. (D) Plot shows the intensity profile of the Nile Blue acrylamide dye diffusion for experimental results from (C) after 7.2 hours of diffusion for $n = 4$ gels. A representative micrograph is displayed above the plot.

observed that diffusion in the microchannel was slower than predicted ($R^2 > 0.95$ achieved after ~ 250 min instead of expected ~ 120 min) (Figure 3.3C). We hypothesize that the slower effective NB diffusion could be due to hydrophobic interactions between NB and BPMAC. This phenomenon, called retarded diffusion, has also been observed when DNA is immobilized in a PA gel[27].

The Nile Blue acrylamide concentration profile is linear after 7.2 hours (Figure 3.3D). We therefore chose a diffusion time of 7 hours or longer as a conservative estimate of time needed to establish a linear Immobililine gradient, which still allowed device fabrication to be completed in one day.

Performance of μ IPG device. We next sought to characterize the μ IPG device performance using a fluorescent pI marker ladder to investigate the linearity of the pH gradient and stability of the pH gradient.

Our μ IPG device was designed to separate proteoforms having pI's in the pH range of

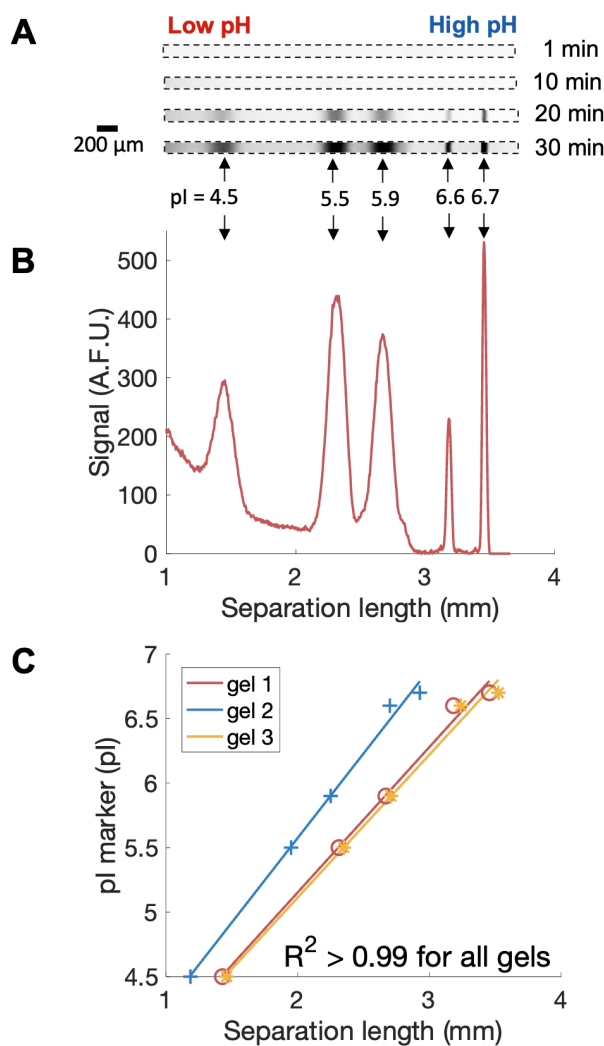


Figure 3.4: IEF of pI markers in μIPG device confirms a linear pH gradient. (A) Inverted fluorescent micrographs of IEF-separated pI markers at several time points demonstrates separation evolution and stability. Micrographs have the same acquisition settings, brightness, and contrast. (B) Intensity plot of pI marker separation from (A) after 20 minutes of focusing. (A)-(B) are representative of $n = 3$ separations. (C) Plot shows the pI of 5 pI markers versus position to determine the linearity of the pH gradient from pH 4.5 – 6.7 for $n = 3$ gels/separations. IPG gel is 6 %T.

3.8 to 7.0. Figure 3.4A demonstrates separation of 5 pI markers (ranging from 4.5 to 6.7). Notably, the μ IPG device resolves pI markers 6.6 and 6.7, which differ by only 0.1 pH unit (Figure 3.4A-B). The IPG-IEF device’s pH gradient is linear from 4.5 to 6.7 (Figure 3.4C). We observe device-to-device variation in the position of the pH gradient within the microchannel (gel 2 in Figure 3.4C). We hypothesize that this variability is caused by the visual alignment of the Kapton tape photomask to the microchannels during device fabrication. Reduction in device-to-device variability can be achieved by the use of a mask aligner. Consequently, we include fluorescent pI markers in all IEF runs to assess run success and as internal standards of pI, as is routine in IEF[28].

To understand the pH gradient stability of IPG-IEF versus CA-IEF, we monitored pI marker peak positions over time in our μ IPG device for both IEF modalities (Figure 3.5). To perform an accurate comparison between IPG-IEF and CA-IEF in our device, the only modifications we made to the CA-IEF condition compared to the IPG-IEF condition are the following: (1) Immobiline reagents were excluded from the PA gel, and (2) the device was incubated in 1% ZOOM Carrier Ampholytes pH 4 to 7 in DI water overnight. The IPG-IEF condition included Immobiline reagents and was incubated in only DI water overnight. Anode and cathode sample components were the same for both IPG-IEF and CA-IEF, as listed in Table 3.2.

As expected of an IPG-based IEF separation, where the pH generating species are covalently fixed in the separation matrix, pI marker peak positions remain fixed over time in the IPG-IEF device (30 minutes tested in Figure 3.4A and 20 minutes tested in Figure 3.5A), resulting in an effective cathodic drift velocity of $\sim 0 \mu\text{m/s}$. On the other hand, we observed a cathodic drift velocity of $70 \mu\text{m/min}$ for the 5.5 pI marker in the CA-IEF configuration (Figure 3.5B). Moreover, we also observed anodic drift for the 4.5 pI marker, which is known as another source of pH gradient instability[29]. Lastly, CA-IEF in our device did not resolve the 5.9 pI marker. We hypothesize that cathodic drift caused the 5.9 pI marker to “run off” the gel before it was sufficiently concentrated to be detected. Our IPG-IEF device represents a marked improvement in pH gradient stability compared to CA-IEF (Figure 3.5B, $70 \mu\text{m/min}$ cathodic drift velocity) and other microscale CA-IEF devices ($\sim 10\text{--}600 \mu\text{m/min}$ cathodic drift velocities)[4, 7–9]. Another defect of CA-IEF is compression of the pH gradient[3]. The μ IPG device presented here does not suffer from pH gradient compression in the pH 4.5 to 6.7 range analyzed over the course of 30 minutes (Figure 3.4A).

Cell Lysate Separations. To understand the performance of the μ IPG device with a complex sample, we performed IEF of cell lysate (Figure 3.6). Cell lysate was prepared from GFP-expressing MCF7 cells to a final concentration of $\sim 20,000$ cells/ μL lysate. Cell lysate IEF experiments were first performed using IPG-only IEF, yet IPG-only IEF did not successfully resolve the pI markers or GFP proteoforms (data not shown). We hypothesized that the additional salts in the cell lysate buffer could be interfering with IEF in the IPG-only device, so we tested mixed-bed CA-IPG IEF in the μ IPG device (Figure 3.6). Mixed-bed CA-IPG IEF is beneficial in samples containing high salt levels where the presence of CA in the sample improves buffering[13]. Mixed-bed CA-IPG IEF is achieved by the addition of 1% CAs to the IPG gel, which we accomplished by incubating the μ IPG device in a sample

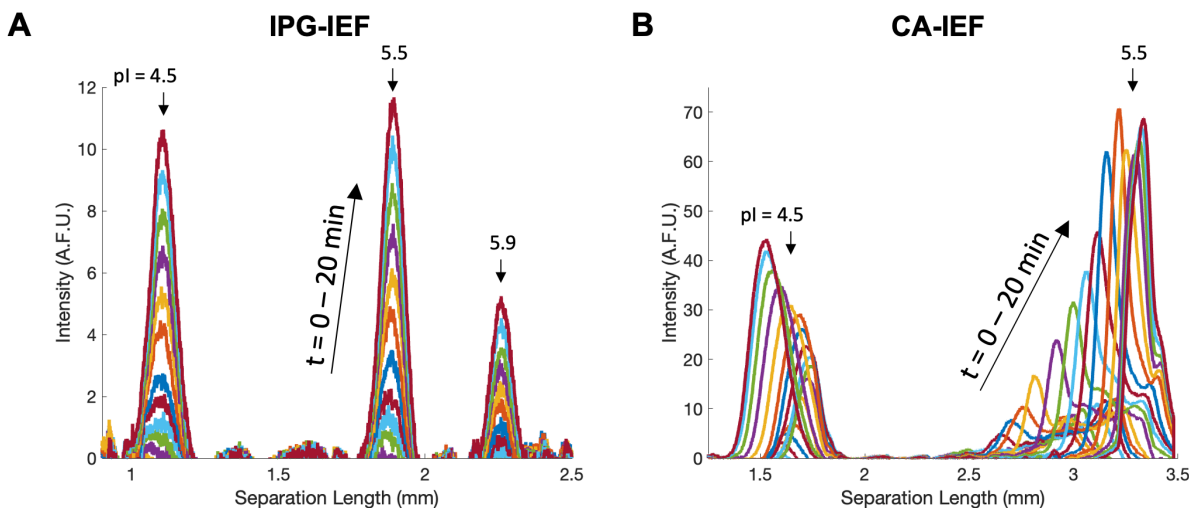


Figure 3.5: Anodic and cathodic drift is eliminated in μ IPG device. Intensity plots of pI markers focused in microfluidic IEF devices. Images were taken every minute for 20 minutes of IEF in (A) μ IPG device and (B) μ IPG device with Immobilines excluded from the PA gel precursor and incubated overnight in 1% ZOOM Carrier Ampholytes pH 4 – 7 to create a CA-IEF condition. Cathodic drift velocity of the 5.5 pI marker in CA-IEF condition is $70 \pm 10 \mu\text{m}/\text{min}$. Representative of $n = 3$ separations.

loading buffer containing 1% CAs.

IEF of GFP-expressing MCF7 cell lysate in the μ IPG device using mixed-bed CA-IEF resolved up to four GFP proteoforms (Figure 3.6A). Out of 14 total separations (technical replicates), 1 separation detected only one GFP proteoform, 5 separations resolved two GFP proteoforms, 4 separations resolved three GFP proteoforms, and 4 separations resolved four GFP proteoforms. Variation in the number of proteoforms resolved could be attributable to the manual fabrication of μ IPG devices, as discussed in the *Performance of μ IPG device section*. Additionally, variation in the distance between electrodes during μ IPG operation could also lead to variability in electric field strengths between technical replicates. The large size of the reservoirs (3-mm diameter) meant that the distance between the electrodes could vary from 3.5 mm to 9.5 mm, and therefore the final electric field strength could vary from 284 V/cm to 771 V/cm. Since separation resolution is dependent on electric field strength[6], changes in electric field strength between different separations could lead to band broadening that would obscure additional proteoform peaks. Mechanically fixing the distance between electrodes could be an avenue to better control electric field strength, and therefore, separation resolution.

The main GFP proteoforms detected with our device had pIs of 4.80 (CV = 0.09%), 4.86 (CV = 0.13%), 4.92 (CV = 0.07%), and 5.00 (CV = 0.266%) for $n = 4$ separations, comparable to the glass-based μ IPG device (GFP pIs ranging from 4.88 to 5.19[14]) and

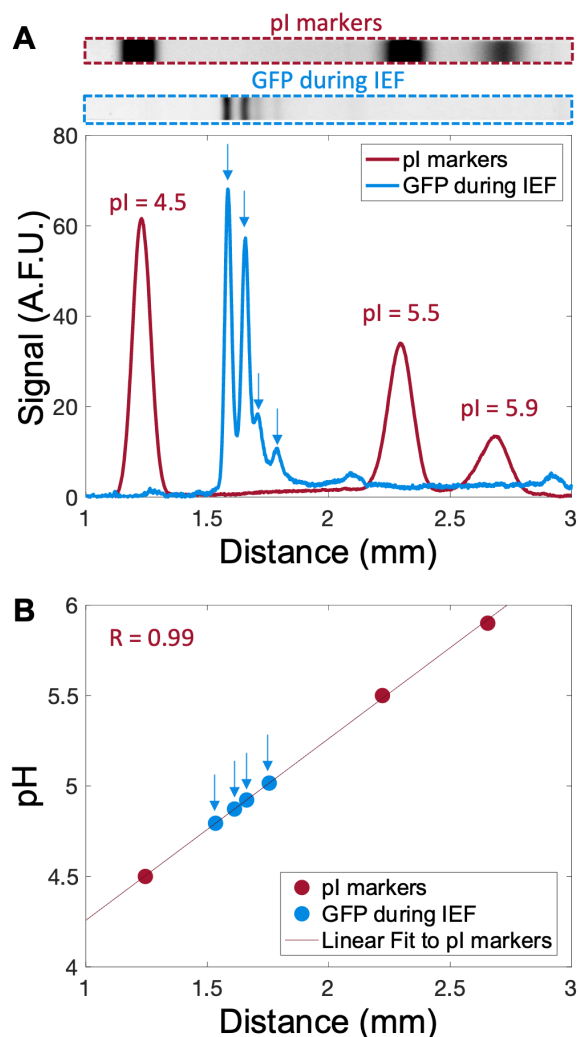


Figure 3.6: μ IPG device resolves GFP proteoforms from MCF7 cell lysate. (A) Inverted fluorescence micrographs and corresponding intensity plot of pI markers and GFP focused in μ IPG device from MCF7 cell lysate (40,000 cells). pI markers and GFP during IEF images taken after 20 minutes of IEF. The x-axis of the intensity plot is also the scale bar for the fluorescence images. (B) Linear fit to pI markers is used to determine pI of GFP proteoforms from separation shown in (A). The GFP proteoforms' pIs are determined to be 4.80 (CV = 0.09%), 4.86 (CV = 0.13%), 4.92 (CV = 0.07%), and 5.00 (CV = 0.266%) for $n = 4$ separations. GFP proteoform peaks are indicated with blue arrows. IPG gel is 12 %T. IEF performed using mixed-bed CA-IPG IEF.

slab IEF (GFP pIs ranging from 4.7 to 5.1[30]). The various GFP proteoforms have been attributed to differential C-terminal cleavage by nonspecific proteases[30]. While the core of the GFP protein is resistant to proteolysis, the C-terminus “tail” sequence, His-Gly-Met-Asp-Glu-Tyr-Lys, contains both basic and acidic amino acid residues, which, when cleaved, produce a variety of GFP proteoforms [30]. These GFP proteoforms can be detected by various techniques, including isoelectric focusing[31] and capillary zone electrophoresis[32, 33].

Since the pI difference between neighboring GFP proteoforms ranges from 0.06 to 0.08, we demonstrate that our PDMS-based μ IPG device can resolve pI differences of about 0.1 for both a protein sample (Figure 3.6) and a fluorescent pI marker sample (Figure 3.4). For context, a single phosphorylation event can cause a pI change of 0.3-0.4[34]. We anticipate that even smaller pI differences can be resolved in the μ IPG device for protein targets larger than GFP, since smaller molecular weight samples tend to experience more peak broadening and therefore loss in separation resolution. GFP has a molecular weight of 27 kDa[30], which makes it a relatively small sized protein[35]. Moreover, the pH gradient in IPGs is highly tunable, so increased separation resolution may also be achieved by choosing a narrower pH range than the 3.8-7.0 pH range employed here.

Critically, the PDMS-based μ IPG device performance is comparable to the previous glass-based μ IPG device, even though the separation length in the PDMS-based μ IPG device is 1.7-fold shorter (3.5 mm versus 6 mm), making it the μ IPG device with the shortest separation length to date. In addition to reducing the footprint of each separation, which can have advantages in throughput[36], we anticipate that this additional miniaturization of the μ IPG device will facilitate analysis of small sample amounts by reducing the available surface area for nonspecific absorption of sample to the microchannel walls or separation matrix. Moreover, compared to CA-based microfluidic devices where the microchannel should be sufficiently long to prevent samples from running off the separation lane due to cathodic drift[3], the separation lane of the μ IPG device can remain short since the peak positions are stationary.

Immunoprobed Readout of μ IPG device. Finally, we performed immunoprobings in the μ IPG device to demonstrate the feasibility of analyzing proteins from complex samples in the μ IPG device. First, we examined the compatibility of our photoactive moiety, BMPAC, with IPG-IEF. Protein photocapture using BMPAC has previously only been demonstrated with CA-IEF[4]. We hypothesized that the buffering capabilities of the Immobililine species within the μ IPG device would be sufficient to mask any contributions from BMPAC to the pH of the PA gel and BMPAC should therefore not inhibit IEF. As shown in the Figure 3.8 pI marker separation on a μ IPG device with BMPAC incorporated into the scaffold gel, we show that BMPAC is compatible with IPG-IEF.

Next, we tested μ IPG delamination from its glass support to expose the μ IPG for diffusive immunoprobings (Figure 3.7A). Since the μ IPG is not covalently attached to the glass slide, we anticipated that the entire μ IPG would be retained on the PDMS layer. For μ IPG devices with a 6 %T IPG gel, the μ IPG was only successfully delaminated from the glass slide 12.5% of the time ($n = 8$ gels from 2 devices) (Figure 3.7B). Increasing the %T of the IPG gel from

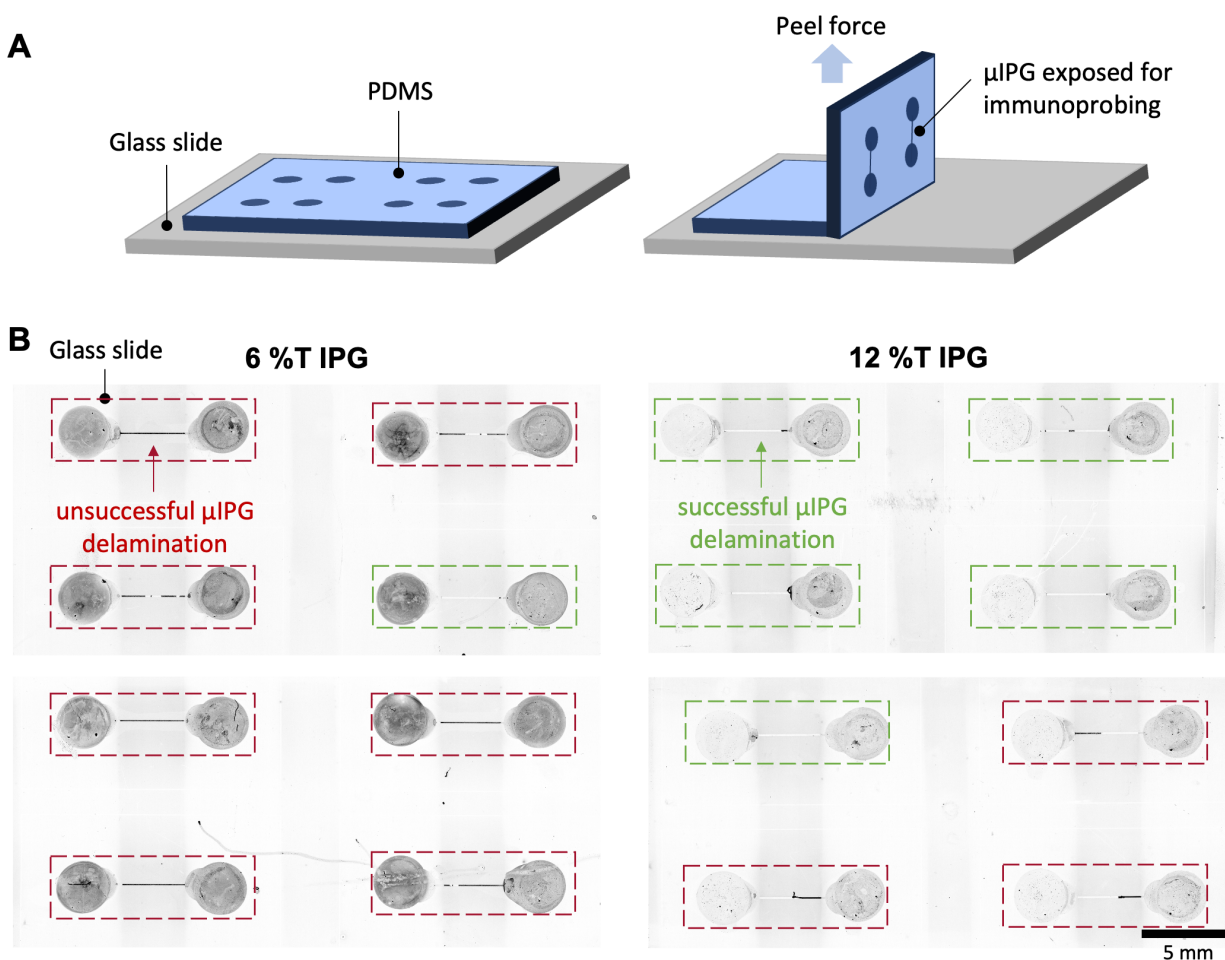


Figure 3.7: Delamination of PDMS from glass to expose μ IPG for immunoprobing. (A) Schematic of PDMS delamination from glass. PDMS peels away from glass since plasma bonding was not performed. (B) Inverted fluorescence micrographs of μ IPG adhered to glass for 6 %T and 12 %T IPG gel formulations ($n = 8$ gels from 2 devices). If μ IPG is present on glass, delamination from glass and retention of μ IPG on PDMS layer was unsuccessful. BP-MAC (PA gel component) autofluorescence measured using 488-filter set. Autofluorescence in the reservoir region is likely autofluorescence from BPMAC and benzophenone adsorbed to glass during device fabrication.

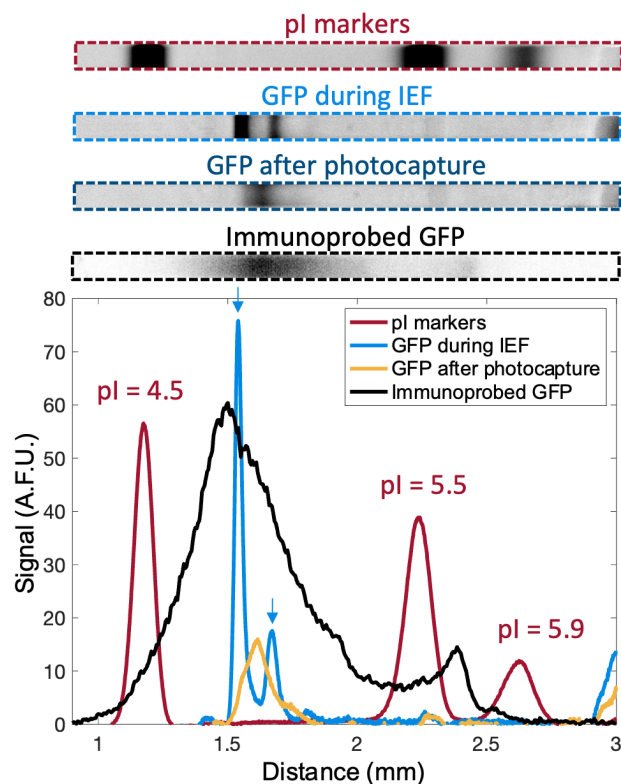


Figure 3.8: Immunoprobing μ IPG device. Inverted fluorescence micrographs and corresponding intensity plot of pI markers and GFP focused in μ IPG device from MCF7 cell lysate (40,000 cells). pI markers and GFP during IEF images taken after 20 minutes of IEF and before electric field is turned off (GFP proteoform peaks are indicated with blue arrows). The electric field was turned off after 20 minutes of IEF and before photocapture of protein. GFP after photocapture image taken immediately after 45 seconds of photocapture with UV light. Immunoprobed GFP image taken after immunoprobing with an anti-GFP primary antibody, followed by a fluorophore-tagged secondary antibody. The x-axis of the intensity plot is also the scale bar for the fluorescence images. Acquisition settings, brightness, and contrast only the same for GFP during IEF and GFP after photocapture micrographs. Representative of $n = 3$ separations. IPG gel is 12 %T. IEF performed using mixed-bed CA-IPG IEF.

6 %T to 12 %T allowed us to accomplish a 5-fold improvement in delamination efficiency to 62.5% ($n = 8$ gels from 2 devices) (Figure 3.7B). While 62.5% successful delamination was sufficient to demonstrate the feasibility of immunoprobng in a μ IPG device, we anticipate that additional improvements in delamination efficiency can be achieved by further increasing the μ IPG gel structural integrity, applying a non-stick coating to the glass slide, or using a sacrificial barrier between the PA gel and the glass[37].

Photocapture of proteins, including GFP, to the μ IPG was conducted after 20 minutes of IEF. The electric field was turned off and the μ IPG was irradiated with UV for 45 seconds to initiate covalent attachment of the proteins to the PA gel matrix. Separation of two GFP proteoforms (indicated by blue arrows) was lost after protein photocapture (Figure 3.8). Prior work has also observed a reduction in separation resolution during protein photocapture due to band broadening[4]. Moreover, this prior investigation also evaluated photocapture efficiency in a microfluidic IEF device and demonstrated that photocapture efficiency varies in different pH conditions, with improved protein photocapture towards the cathode[4], which could explain the shift in peak position after photocapture in our device (Figure 3.8).

The μ IPG was then exposed by delamination of the PDMS from the glass slide, washed in TBS-T, and immunoprobed with a primary anti-GFP antibody and a fluorescent secondary antibody. The GFP band after photocapture and after immunoprobing has the same characteristic shape and peak position (Figure 3.8), confirming the feasibility of immunoprobing in a μ IPG device. However, further band broadening of the GFP band was observed between photocapture and immunoprobing step, meaning there is an additional loss in separation resolution and peak capacity. Additionally, there is a peak artifact between pI 5.5 and 5.9 that is not observed prior to immunoprobing. Since antibody binding efficiency can be highly dependent on local pH[38], we anticipate that minor artifacts and differences between photocaptured and immunoprobed signal, including the aforementioned band broadening, could be features of immunoprobing in an IPG gel. Therefore, relative quantitation of protein bands between different devices would be more appropriate than relative quantitation of protein bands within a single device, since band intensities may be a function of photocapture and antibody binding efficiency, rather than abundance alone. We hypothesize that further improvement of the quantitative abilities of μ IPG could be achieved by dissolving the IPG prior to immunoprobing using a commercially available reversible crosslinker, such as bis-acrylylcystamine (BAC). Since BPMAC is only contained in the scaffold gel, photocaptured proteins should remain immobilized while the IPG, and therefore pH gradient, is dissolved for more uniform immunoprobing.

3.5 Conclusions

In conclusion, the development of the PDMS-based immobilized pH gradient microfluidic device (μ IPG) represents a significant advancement in microfluidic analytical tools for proteomic assays. By addressing the limitations of traditional carrier ampholytes (CAs) and difficult-to-manufacture glass devices, the μ IPG offers a versatile and efficient platform for

protein separation and analysis.

The μ IPG overcomes the need for protein labeling, allowing for the analysis of complex, unlabeled samples such as cell lysate. This capability is demonstrated by successfully immunoprobng GFP from GFP-expressing MCF-7 cells, highlighting the utility of the μ IPG device in proteomic studies.

The two-step photopolymerization procedure utilized in the μ IPG enables the creation of a composite gel with dual functionality. Firstly, it facilitates isoelectric focusing (IEF) protein separation through the IPG gel component, allowing for resolution of proteoforms differing by approximately 0.1 isoelectric point. Secondly, it enables protein capture for downstream immunoprobng via the photoactive gel component.

Looking ahead, the development and optimization of the μ IPG present opportunities for further advancements in microfluidic proteomic assays. Future research can focus on expanding the capabilities of the μ IPG by exploring different gel formulations and optimizing the immunoblotting step. Additionally, efforts can be directed towards enhancing the sensitivity and resolution of the μ IPG for the analysis of complex protein samples, enabling the detection and characterization of rare or low-abundance proteoforms. Moreover, the flexibility of PDMS allows for the creation of complex microfluidic designs and the integration of various features, such as channels, valves, and chambers, in a single device. We anticipate that the PDMS-based μ IPG device presented here could be integrated into other PDMS-based microfluidic devices for additional capabilities (i.e., to automate cell culture and sample preparation).

In summary, the PDMS-based IPG microfluidic device (μ IPG) offers a versatile, efficient, and stable platform for microfluidic proteomic assays. With its ability to analyze complex, unlabeled samples and achieve high-resolution protein separation, the μ IPG holds great promise for advancing the field of proteomics and contributing to the miniaturization, sensitivity, throughput, and automation of analytical techniques.

References

- (1) Smith, L. M.; Kelleher, N. L. *Nature Methods* **2013**, *10*, 186–187.
- (2) Tentori, A. M.; Yamauchi, K. A.; Herr, A. E. *Angewandte Chemie International Edition* **2016**, *55*, 12431–12435.
- (3) Cui, H.; Horiuchi, K.; Dutta, P.; Ivory, C. F. *Analytical Chemistry* **2005**, *77*, 1303–1309.
- (4) Hughes, A. J.; Lin, R. K. C.; Peehl, D. M.; Herr, A. E. *Proceedings of the National Academy of Sciences* **2012**, *109*, 5972–5977.
- (5) Righetti, P. G., *Immobilized PH Gradients: Theory and Methodology*; Elsevier: 1990.
- (6) Righetti, P. G., *Isoelectric Focusing: Theory, Methodology, and Applications*; Elsevier Biomedical Press: 1983.

- (7) Xu, Z.; Okabe, N.; Arai, A.; Hirokawa, T. *ELECTROPHORESIS* **2010**, *31*, 3558–3565.
- (8) Yamauchi, K. A.; Tentori, A. M.; Herr, A. E. *ELECTROPHORESIS* **2018**, *39*, 1040–1047.
- (9) Tentori, A. M.; Hughes, A. J.; Herr, A. E. *Analytical Chemistry* **2013**, *85*, 4538–4545.
- (10) Righetti, P. G.; Macelloni, C. *Journal of Biochemical and Biophysical Methods* **1982**, *6*, 1–15.
- (11) Wang, Z.; Ivory, C.; Minerick, A. R. *ELECTROPHORESIS* **2017**, *38*, 2565–2575.
- (12) Corbett, J. M.; Dunn, M. J.; Posch, A.; Görg, A. *ELECTROPHORESIS* **1994**, *15*, 1205–1211.
- (13) Rabilloud, T.; Barzaghi, B.; Giorgi Righetti, P. *Journal of Biochemical and Biophysical Methods* **1988**, *16*, 237–241.
- (14) Sommer, G. J.; Singh, A. K.; Hatch, A. V. *Analytical Chemistry* **2008**, *80*, 3327–3333.
- (15) Nielsen, J. B.; Hanson, R. L.; Almughamsi, H. M.; Pang, C.; Fish, T. R.; Woolley, A. T. *Analytical Chemistry* **2020**, *92*, 150–168.
- (16) McDonald, J. C.; Whitesides, G. M. *Accounts of Chemical Research* **2002**, *35*, 491–499.
- (17) Abdel-Sayed, P.; Yamauchi, K. A.; Gerver, R. E.; Herr, A. E. *Analytical Chemistry* **2017**, *89*, 9643–9648.
- (18) Hansen, L. L.; Lomeli, G.; Vlassakis, J.; Herr, A. E. In *Single Cell ‘Omics of Neuronal Cells*, Sweedler, J. V., Eberwine, J., Fraser, S. E., Eds.; Neuromethods; Springer US: New York, NY, 2022, pp 165–192.
- (19) Geldert, A.; Huang, H.; Herr, A. E. *Scientific Reports* **2020**, *10*, 8768.
- (20) Raj M, K.; Chakraborty, S. *Journal of Applied Polymer Science* **2020**, *137*, 48958.
- (21) Kang, C.-C.; Yamauchi, K. A.; Vlassakis, J.; Sinkala, E.; Duncombe, T. A.; Herr, A. E. *Nature Protocols* **2016**, *11*, 1508–1530.
- (22) Schneider, M. H.; Tran, Y.; Tabeling, P. *Langmuir* **2011**, *27*, 1232–1240.
- (23) Righetti, P. G.; Tonani, C. *ELECTROPHORESIS* **1991**, *12*, 1021–1027.
- (24) Park, I. H.; Johnson, C. S.; Gabriel, D. A. *Macromolecules* **1990**, *23*, 1548–1553.
- (25) Evans, R.; Deng, Z.; Rogerson, A. K.; McLachlan, A. S.; Richards, J. J.; Nilsson, M.; Morris, G. A. *Angewandte Chemie International Edition* **2013**, *52*, 3199–3202.
- (26) Pozrikidis, C.; Ferziger, J. H. *Physics Today* **1997**, *50*, 72–74.
- (27) Moss, A. C.; Herr, A. E. *APL Bioengineering* **2020**, *4*, 046104.
- (28) Duša, F.; Kubesová, A.; Šalplachta, J.; Moravcová, D. *TrAC Trends in Analytical Chemistry* **2023**, *162*, 117018.

- (29) Thormann, W.; Mosher, R. A. *ELECTROPHORESIS* **2021**, *42*, 814–833.
- (30) Chalfie, M.; Kain, S. R., *Green Fluorescent Protein: Properties, Applications and Protocols*; John Wiley & Sons: 2005.
- (31) Hughes, A. J.; Tentori, A. M.; Herr, A. E. *Journal of the American Chemical Society* **2012**, *134*, Publisher: American Chemical Society, 17582–17591.
- (32) Korf, G. M.; Landers, J. P.; O’kane, D. J. *Analytical Biochemistry* **1997**, *251*, 210–218.
- (33) Radko, S. P.; Stastna, M.; Buzas, Z.; Kingsley, D.; Chrambach, A. *Analytical Biochemistry* **1999**, *274*, 146–148.
- (34) O’Neill, R. A. et al. *Proceedings of the National Academy of Sciences* **2006**, *103*, 16153–16158.
- (35) Maier, T.; Schmidt, A.; Güell, M.; Kühner, S.; Gavin, A.-C.; Aebersold, R.; Serrano, L. *Molecular Systems Biology* **2011**, *7*, 511.
- (36) Grist, S. M.; Mourdoukoutas, A. P.; Herr, A. E. *Nature Communications* **2020**, *11*, 6237.
- (37) Ou, J.; Ren, C. L.; Pawliszyn, J. *Analytica Chimica Acta* **2010**, *662*, 200–205.
- (38) Luisa, B. G., *Immunoassay: A Practical Guide*; Elsevier: 2012.

Chapter 4

Towards Pore-Size Gradient Gels for Projection Electrophoresis

This work was performed in collaboration with Dr. Samantha M. Grist.

4.1 Abstract

3D projection electrophoresis is a single-cell protein analysis technique that offers increased throughput compared to previous 2D single-cell electrophoresis devices[1], with the potential to perform electrophoresis of intact tissue while preserving spatial context[2]. However, 3D projection electrophoresis relies on confocal/light-sheet imaging readout, which limits the separation distance and therefore, separation performance. To overcome this limitation and enhance the capabilities of the technique, we propose using gradient pore-size gels, which can separate a broader range of molecular weight proteins within the same distance versus uniform pore-size gels[3]. The current methods of generating gradient pore-size gels are not readily compatible with the miniaturized gel format required by 3D projection electrophoresis. In this chapter, we present two approaches for producing gradient pore-size hydrogels that are suitable for 3D projection electrophoresis. The first method involves modulating the concentration of gel precursor components across the hydrogel to control pore-size. The second method employs the modulation of oxygen concentration across the hydrogel to selectively inhibit polymerization, thereby providing an additional avenue for controlling pore-size. These material advances open up new possibilities for improving the separation performance of 3D projection electrophoresis.

4.2 Introduction

Improvements in single-cell protein analysis are required to study the cell-to-cell variation inherent to many diseases, including cancer[4]. Cell-to-cell heterogeneity has important biological consequences, as it can dictate the cell's response to drugs or other stimuli[4]. One

method of single-cell protein analysis, the single-cell western blot, enables electrophoretic protein separation followed by antibody probing of single-cell lysates[5]. By first separating proteins by size, off-target antibody binding can be more readily excluded from protein quantification[5]. However, the standard single-cell western blotting platform requires cells to be detached from each other or their substrate to be isolated in microwells for analysis. This detachment step can be detrimental for accurate protein quantification, since a cell's proteome, and resulting behavior, is influenced by its environment[6]. Moreover, detachment also eliminates tissue context information, which is necessary for understanding the driving factors in cell heterogeneity. For example, tumor cell behavior depends on the cell's access to nutrients and oxygen, as well as the mechanical properties of the surrounding extracellular matrix[7].

In order to perform western blots of individual cells within tissue slices while preserving 2-D spatial information, our group has developed an assay called 3D projection electrophoresis[1]. In this assay, the sample of cells or tissue slice will be covered with polyacrylamide (PA) gel slabs of 1-mm thickness, allowing for electrophoresis into the gel without having to isolate single cells[1, 2]. However, it can be difficult to achieve good protein separation in a short separation distance (1 mm)[8]. Conventional western blots (as well as single cell western blots) have employed a gradient pore size in the axis of separation in order to improve separation efficiency[3, 8]. Electrophoresis into gradient pore size gels allows proteins to migrate until the decreasing pore size slows down or stops their progress. This has several advantages, including sharper bands, separation of a larger range of molecular weights, and separation of proteins close in molecular weight[9]. The conventional fabrication method of gradient pore-size gels involves the use of gradient former to perform a controlled pour of light and heavy acrylamide solutions[10]. However, gradient formers are best suited for centimeter-scale gels and would be difficult to implement for a 1-mm thick gel.

This chapter describes the development of a gel slab for tissue projection electrophoresis with a gradient pore size in the z-direction (axis of separation). First, we implement ratio-metric imaging in order to assess gel density (a proxy for pore-size) of a 1-mm thick gel using an epifluorescence microscope. We then explore two strategies to create gradient pore-size gels for 3D projection electrophoresis. In the first approach, a concentration gradient of gel precursor components is created using diffusion and photopolymerized to create a gradient pore-size gel. In the second approach, gel precursor components are maintained constant, but oxygen levels in the precursor are modulated to selectively inhibit polymerization, and therefore a pore-size gradient is additionally attained. The gradient pore-size gels could be integrated with projection electrophoresis (Figure 4.1) to enhance protein separation performance.

4.3 Materials and Methods

Gel fabrication. Substrate-free and featureless PA gels were fabricated following previously described methods[1], with modifications to create pore-size gradient cells. The recipes

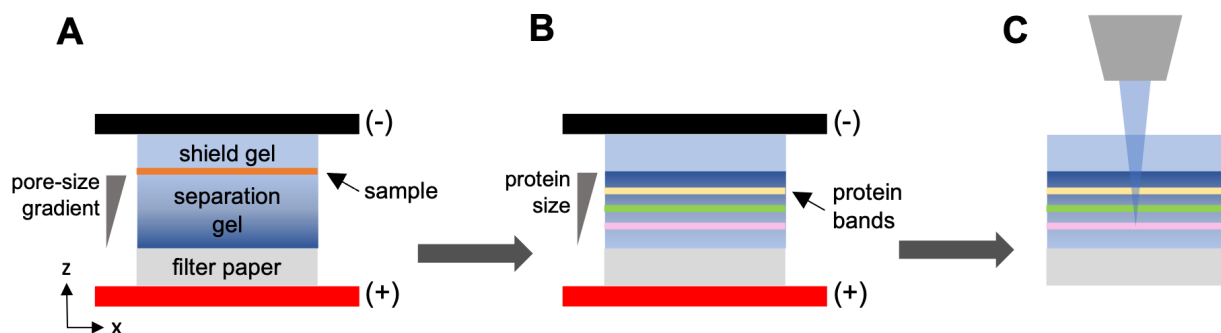


Figure 4.1: Proposed workflow for using pore-size gradient gel for high-throughput single-cell projection electrophoresis. (A) Assemble electrodes, shield gel, single-cell or tissue sample, pore-size gradient separation gel, and buffer-soaked filter paper. (B) Apply an electric field and photo-capture proteins. (C) Perform confocal/light-sheet imaging after immunoprobing.

for the various gel conditions used in this chapter are summarized in Table 4.1. To prepare the gel precursor solution, 30% acrylamide/bis-acrylamide (Sigma A3699), Rhinohide (ThermoFisher R33400), and N-[3-[(3-benzoylphenyl)formamido]propyl] methacrylamide (BPMAC, custom synthesized by PharmAgra Laboratories) were diluted in deionized (DI) water from an Ultrapure Millipore filtration system (18.2 M Ω). Rhinohide enhances the gel's strength, while BPMAC provides a photo-active moiety for protein photocapture (a feature not utilized in this chapter). For fluorescence imaging, rhodamine B methacrylate (Polysciences 23591) and/or allylamine (Sigma 145831) were added to the gel precursor. Throughout the rest of this chapter, rhodamine B methacrylate is referred to simply as "rhodamine B." To initiate polymerization, ammonium persulfate (APS, Sigma A3678) and N,N,N,N-tetramethylethylenediamine (TEMED, Sigma T9281) were incorporated into the gel precursor.

The gel precursor was deposited between a glass plate (McMaster-Carr) and a standard microscope slide (VWR 48300-048), both treated with GelSlick (Lonza 50640) to prevent the gel from sticking. A 1-mm spacer (C.B.S. Scientific Gel Wrap) was placed between the two glass pieces to define the gel's thickness. Polymerization was allowed to proceed for 60 minutes in a humidified, dark chamber. Subsequently, the gel/glass assembly was hydrated with DI water before the gel was released and cut to size (1 cm x 1 cm) using a razor blade. Unless otherwise stated, gels containing allylamine were incubated in 0.1 mg/mL fluorescein isothiocyanate isomer I (FITC, Sigma F7250) for 8 hours or overnight, and finally rinsed in DI water for an additional 2 hours.

For gradient pore-size gels, either a delivery gel or the separation gel itself was incubated in a gel precursor prepared by diluting 40% acrylamide/bis-acrylamide (Sigma A7802), rhodamine B, and the UV photoinitiator 2,2-Azobis(2-methyl-N-(2-hydroxyethyl)propionamide)

(VA086, Wako Chemicals 01319342). After the gel precursor or oxygen gradient formation (further details in Results and Discussion), UV excitation for gel photopolymerization was provided by an OAI Model 30 Collimated UV light source. UV light was applied for 4 minutes at 20 mW cm⁻² through a 390 nm longpass UV filter (Edmund Optics).

Table 4.1: Recipes for the various gel conditions.

Fig.	Gel Type	Gel Precursor Recipe	Polymerization Conditions	Buffer/ Additional Gel Precursor
4.2C	Uniform pore-size %T standards	<ul style="list-style-type: none"> • 30% (37.5:1) PA stock; final concentration 6, 8, 12, 16 or 20 %T • 3.75 μM rhodamine B per %T • 0.67% rhinohide per %T • 3 mM BPMAC • 0.08% (w/v) APS • 0.08% (v/v) TEMED 	60 mins (chemical polymerization)	N/A
4.3	Uniform pore-size gels to assess spectral overlap	<ul style="list-style-type: none"> • 30% (37.5:1) PA stock; final concentration 6 %T • If present, 1:100 molar ratio allylamine with acrylamide • If present, 3.75 μM rhodamine B per %T • 0.67% rhinohide per %T • 3 mM BPMAC • 0.08% (w/v) APS • 0.08% (v/v) TEMED 	60 mins (chemical polymerization)	N/A
4.4	Uniform pore-size to assess ratiometric imaging and %T standards	<ul style="list-style-type: none"> • 30% (37.5:1) PA stock; final concentration 6 %T • 1:100 molar ratio allylamine with acrylamide • 0.67% rhinohide per %T • 3 mM BPMAC • 0.08% (w/v) APS • 0.08% (v/v) TEMED 	60 mins (chemical polymerization)	<ul style="list-style-type: none"> • 40% (37.5:1) PA stock; final concentration 0, 3, 10, 18, 25 %T • 3.75 μM rhodamine B per %T • 0.2% VA-086
4.5	Delivery gel and 'sink' gel	<ul style="list-style-type: none"> • 30% (37.5:1) PA stock; final concentration 6 %T • 0.67% rhinohide per %T 	60 mins (chemical polymerization)	Delivery gel: <ul style="list-style-type: none"> • 40% (37.5:1) PA stock; final

		<ul style="list-style-type: none"> • 0.08% (w/v) APS • 0.08% (v/v) TEMED 		concentration 25 %T <ul style="list-style-type: none"> • 3.75 μM rhodamine B per %T • 0.2% VA-086 'Sink' gel: • DI water only
4.5	Pore-size gradient gel	<ul style="list-style-type: none"> • 30% (37.5:1) PA stock; final concentration 6 %T • 1:100 molar ratio allylamine with acrylamide • 0.67% rhinohide per %T • 3 mM BPMAC • 0.08% (w/v) APS • 0.08% (v/v) TEMED 	60 mins (chemical polymerization) followed by 4 min UV-initiated polymerization after "sandwich method"	<ul style="list-style-type: none"> • Additional gel precursor added using "sandwich method" with delivery and 'sink' gels
4.6, 4.7	Pore-size gradient gel	<ul style="list-style-type: none"> • 30% (37.5:1) PA stock; final concentration 6 %T • 1:100 molar ratio allylamine with acrylamide • 0.67% rhinohide per %T • 3 mM BPMAC • 0.08% (w/v) APS • 0.08% (v/v) TEMED 	60 mins (chemical polymerization) followed by 4 min UV-initiated polymerization after soaking in gel precursor	<ul style="list-style-type: none"> • 40% (37.5:1) PA stock; final concentration 25 %T • 3.75 μM rhodamine B per %T • 0.2% VA-086

Fluorescence imaging. All experiments were imaged using a 4 \times air objective on an Olympus IX71 inverted epifluorescence microscope equipped with an Andor iXon+ EMCCD camera, ASI motorized stage, and X-cite exacte illumination system from Lumen Dynamics. GFP and TRITC filter sets were used to image FITC and rhodamine B, respectively.

4.4 Results and Discussion

Ratiometric imaging allows for high quality imaging of 1-mm thick gels

Our first objective was to establish a calibration curve using a fluorescent indicator of gel density, which would later enable us to verify the formation of a gradient and determine the %T of that gradient. Additionally, we aimed to confirm that gels of uniform pore size also exhibit uniform fluorescence from rhodamine B using our gel slicing method (Figure 4.2A). However, the intensity profile of each uniform pore-size gel varied greatly across the z-axis (Figure 4.2B-C). This variation would make it very difficult to generate a calibration curve from Figure 4.2C and, in further studies, to differentiate a gradient from a uniform gel.

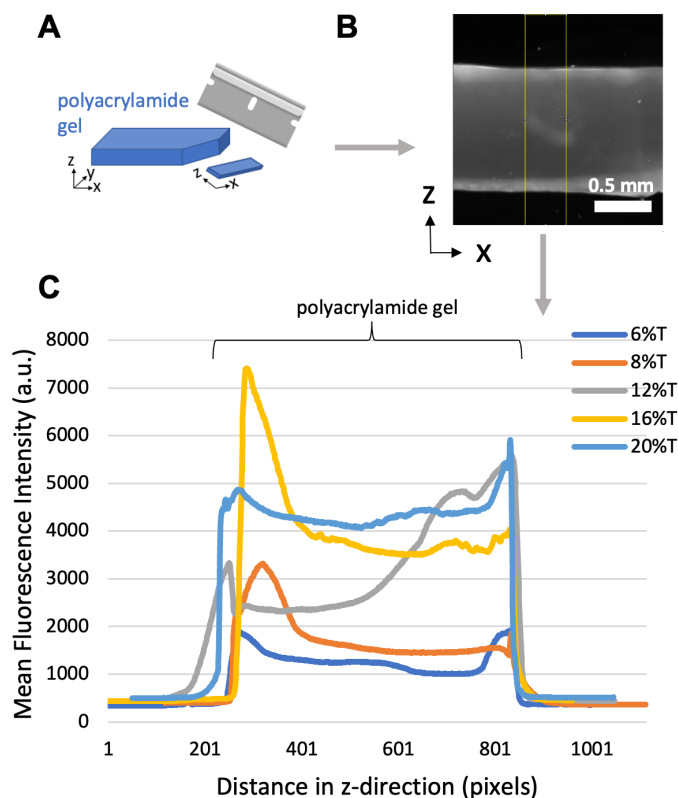


Figure 4.2: Fluorescence intensity profile of rhodamine B as an indicator of gel density does not yield quantifiable results. (A) A 0.75-mm spacer placed between two razor blades is used to cut a 0.75-mm thick gel slice in a single movement. (B) Fluorescence micrograph of rhodamine B-labeled polyacrylamide gel slice. (C) Intensity plot of fluorescence micrographs for polyacrylamide gel standards with different gel densities ($n = 1$). High variability in mean fluorescence intensity within gel region and overlap between different standards indicate that imaging of polyacrylamide gel using method in (A) and rhodamine B dye alone is not adequate to establish a calibration curve for %T.

Visually, it was apparent that the gel slices were uneven, so the varying fluorescence profile is likely due to inconsistent slicing of the gels.

We hypothesized that epifluorescence imaging is sensitive to the variable gel slice thickness and sought out to find a strategy to overcome this limitation. Ratiometric imaging is an approach that can overcome inhomogeneities arising from varying sample thickness, non-uniform illumination, and inhomogeneous sensitivity of the detection system[11]. Ratiometric imaging involves calculating the ratio between the intensity image of interest and a reference image to obtain a ratiometric image independent of inhomogeneities[11]. For

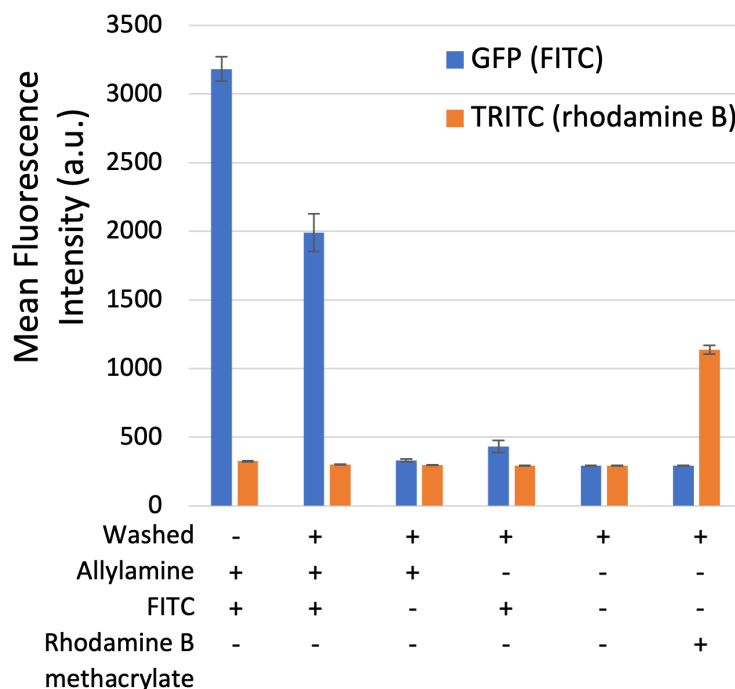


Figure 4.3: FITC and rhodamine B do not exhibit spectral overlap. Mean fluorescence intensity plot of different gels (conditions listed below plot) with different filters (GFP or TRITC). Error bars represent the standard deviation of $n = 3$ measurements on a single gel.

our PA gels, we selected FITC as the reference dye and rhodamine B as the gel density readout dye. Both FITC and rhodamine B are incorporated into the PA gel. Importantly, we confirmed that FITC and rhodamine B do not exhibit spectral overlap in our sample and imaging setup (Figure 4.3), ensuring that FITC and rhodamine B are an appropriate fluorescent dye pair for ratiometric imaging. Additionally, only gels that had allylamine incorporated into the acrylamide backbone demonstrated FITC fluorescence (Figure 4.3), confirming that the allylamine-FITC method to fluorescently label PA gels was successful.

By calculating the ratio between two images, we can obtain a ratiometric image that does not depend on gel thickness. In order to calculate a ratiometric image, we used the following equation:

$$R = \frac{\text{rhodamine B intensity}}{\text{FITC intensity}} = \frac{\text{TRITC channel}}{\text{GFP channel}} \quad (4.1)$$

We next sought to assess whether ratiometric imaging improves the quality of the resulting image of a uniform pore-size gel. The coefficient of variation (CV) is reduced from 23% in the TRITC image alone to 7.6% in the ratiometric image (Figure 4.4A-B), demonstrating that ratiometric imaging indeed reduces inhomogeneities from varying gel thickness.

Accordingly, we were able to produce a calibration curve of R versus %T for a range of 0 to 25 %T ($R^2 = 0.9962$) (Figure 4.4C).

Making gradient pore-size gels using a “sandwich” method

Our first attempt was to test a “sandwich” method for generating gradient pore-size gels, which uses a delivery gel to create a gel precursor concentration gradient in an existing gel. As shown in Figure 4.5A and 4.5B, three gels are sandwiched between two glass slides. The pink gel is the gel precursor-saturated delivery gel containing rhodamine B. The yellow middle gel is the FITC-labeled separation gel. The clear bottom gel is the ‘sink’ gel to keep the bottom boundary of the separation gel close to 0%T additional gel precursor.

We calculated the characteristic timescale of gel precursor diffusion into the gel to inform selection of the diffusion time for the gradient fabrication. The characteristic timescale, τ , for 1-D diffusion is given by the following equation:

$$\tau = \frac{z^2}{2D} \quad (4.2)$$

where z is the sample thickness in meters and D is the diffusion coefficient of the solute in m^2/s . Using eqs 3.1, 3.2, 3.3, and 3.4, we calculated the diffusion coefficient of rhodamine B (the largest and fluorescent gel precursor component, $\text{MW} = 666.2$ Da) in 6%T PA to be 7.6×10^{-10} m^2/s . Since the thickness of the gel is 1 mm, we can estimate τ to be 3.67 minutes. We therefore selected a 3-minute (Figure 4.5C) and 5-minute (Figure 4.5D) gel-gel contact time to allow diffusion of gel precursor components into the separation gel. From looking at the unreferenced rhodamine B image and comparing the intensity to the calibration curve in Figure 4.4B, it appears that the 5-minute gel has a gel density of ~ 8.7 -9.3%T (after adding back the initial 6%T). However, from Figure 4.5D, it is also apparent that unpolymerized rhodamine B did not have enough time to completely wash away, so ~ 8.7 -9.3%T is an overestimate of gel density. Overall, the gel “sandwich” method does appear to create a pore-size gradient in the z -direction.

Making gradient pore-size gels using controlled oxygen-inhibited photopolymerization

Our next step was to determine whether we could modulate pore size by adjusting oxygen concentration within the PA gel precursor. For conventional PA gel fabrication, it is essential to properly degas the gel precursor, as dissolved oxygen in the precursor will inhibit free radical polymerization[12]. As shown in Figure 4.6, oxygen inhibits polymerization of additional gel precursor, especially in regions of the gel directly exposed to air. It is noteworthy to point out that the gels that were polymerized without a glass lid took on a curved conformation (Figure 4.6A). It appears as if the denser gel portions tend to swell, as highlighted by the red arrows (Figure 4.6A-B). This effect has been observed by others previously[8].

The gradient pore-size hydrogel depicted in Figure 4.6A shows a sudden step change in gel density. To soften the transition between low density (high porosity) and high density (low porosity), we hypothesized that incubating the gel in gel precursor in a nitrogen chamber

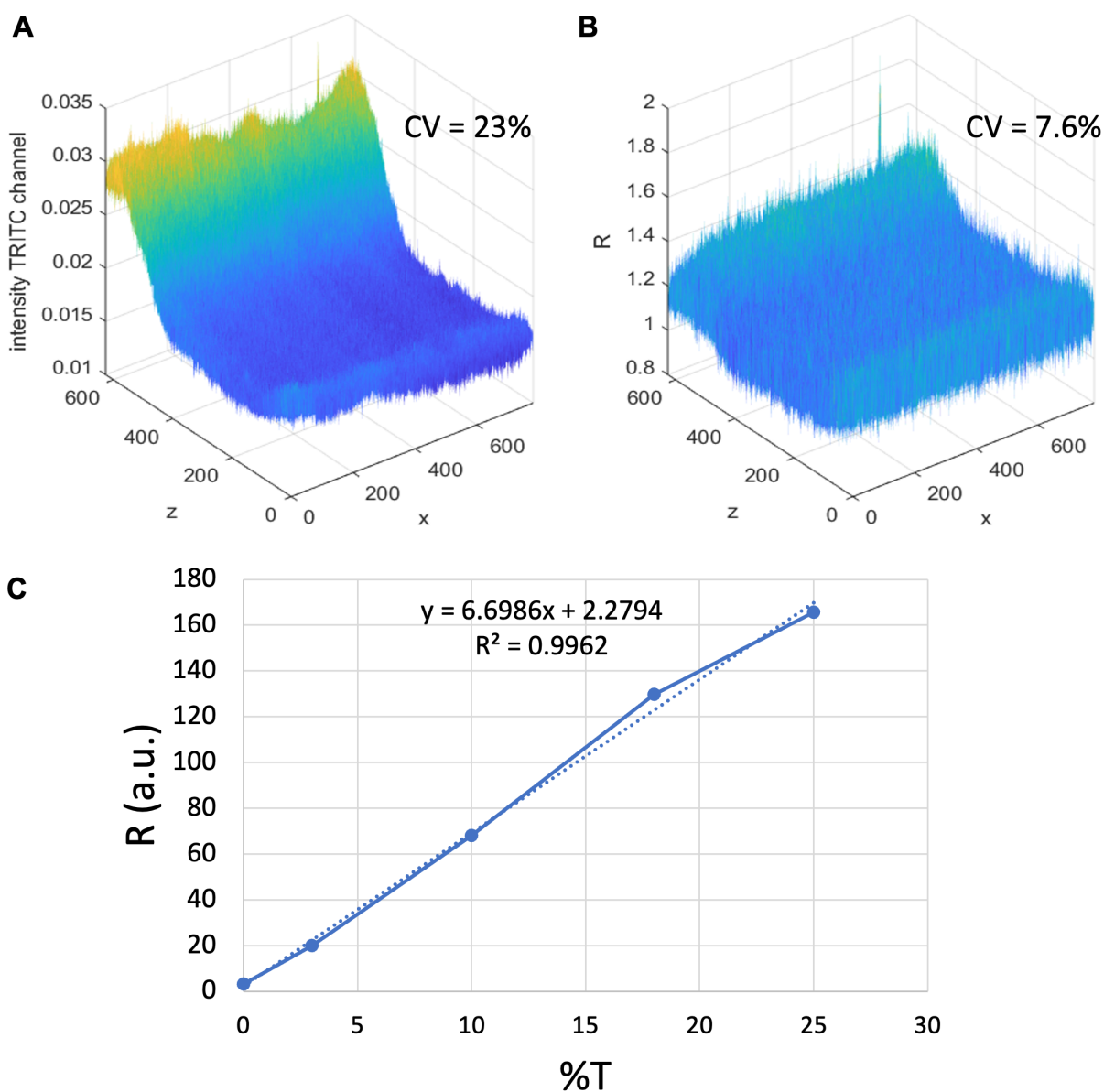


Figure 4.4: Example of how ratiometric imaging improves the quality of intensity image alone for a more quantitative assessment of pore-size (proportional to %T). (A) Intensity plot of rhodamine B (TRITC channel). (B) Ratiometric image obtained by division of the TRITC channel by the GFP channel (eq 4.1). The gel was labeled with FITC and soaked in 25%T gel precursor containing rhodamine B. Additional gel precursor was not washed away or polymerized. (C) Calibration curve of R versus %T from ratiometric images ($R^2 = 0.9962$).

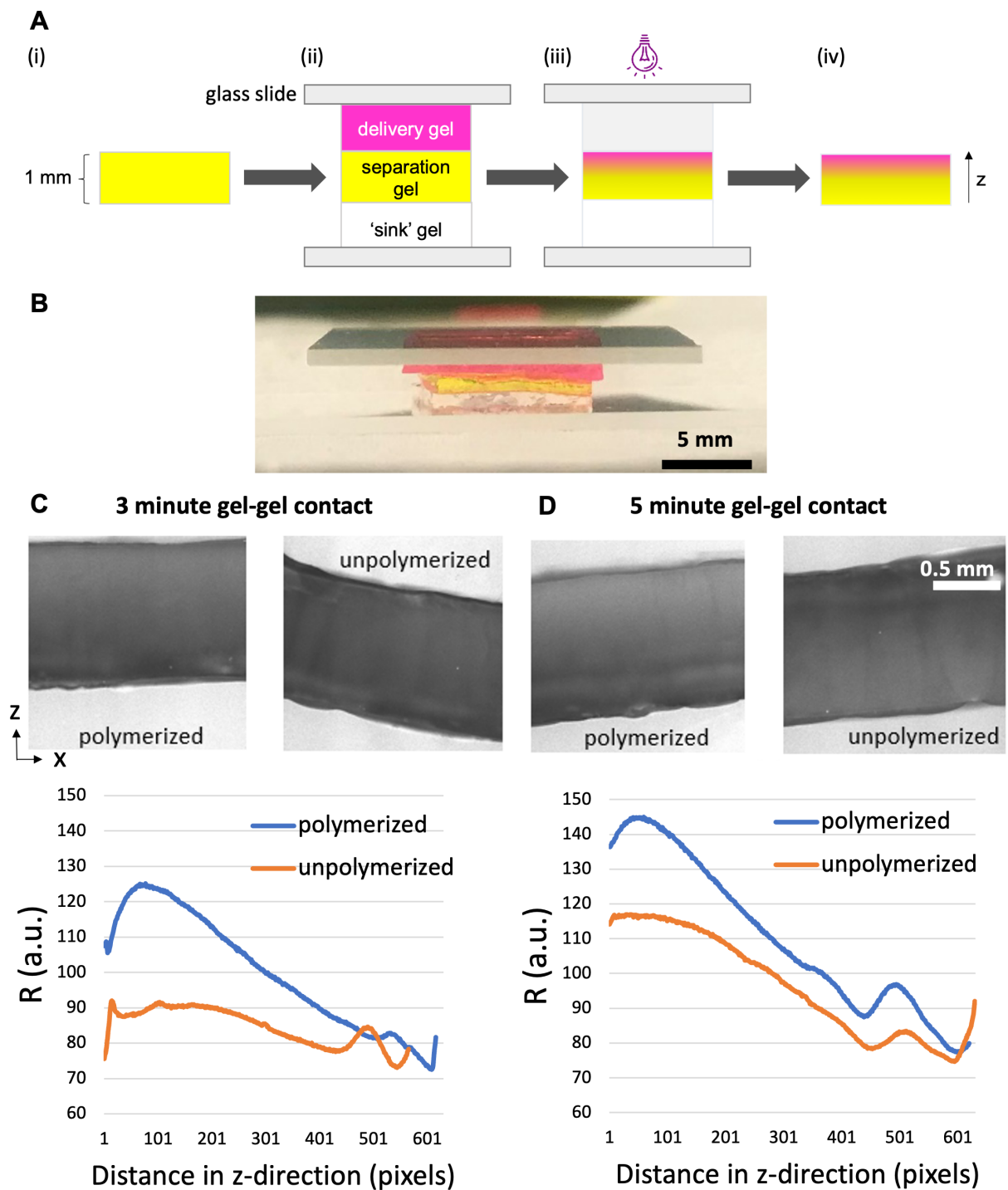


Figure 4.5: “Sandwich” method for creating z-direction pore-size gradient gels. (A) Schematic of the “sandwich” method. (i) A uniform pore-size gel is first polymerized. (ii) A delivery gel is saturated with gel precursor and delivers additional gel precursor to the separation gel by diffusion, creating a gradient of gel precursor components. (iii) Photopolymerization of the gel precursor gradient creates a (iv) z-direction pore-size gradient gel. (B) Photo of the assembled gel “sandwich,” labeled in (ii). Ratiometric images and intensity profile plots for (C) 3-minute gel-gel contact and (D) 5-minute gel-gel contact. The polymerized condition underwent photopolymerization and washing of excess gel precursor, while the unpolymerized condition did not undergo photopolymerization but was washed of excess gel precursor. Gels depicted do not have replicates.

could reduce the dissolved oxygen in the PA gel precursor. Oxygen would then diffuse back into the gel precursor during transfer of the gel from the nitrogen chamber to the OAI instrument for photopolymerization, creating a pore-size gradient. We calculated the characteristic timescale of oxygen diffusion into the sample to inform selection of nitrogen chamber incubation time and time for transfer of the gel from the nitrogen chamber to the OAI. Based on previous work, the diffusion coefficient for oxygen in PA gel or similar gels is around 2.1×10^{-9} - 8×10^{-10} m²/s[13, 14]. Using eq 4.2 we estimate τ to be 1.32-3.47 minutes for oxygen diffusion in PA gel. We therefore selected a 2 minute nitrogen incubation time and anticipated the time to transfer the gel from the nitrogen chamber to the OAI to naturally approximate 2 minutes as well. Figure 4.7 demonstrates that oxygen can be used to create a gradient pore-size gel. From looking at the unreferenced rhodamine B image and comparing the intensity to the calibration curve in Figure 4.4B, it appears that the open-faced sandwich condition (which allows oxygen to diffuse into the precursor after degassing) has an apparent gel density of ~ 20 - 30% T (after adding back the initial 6% T).

Using oxygen to modulate polymerization efficiency has the added advantage of being a more controlled method than manually sandwiching gels. The oxygen modulation method is analogous to the method used by Duncombe et al. to create gradient pore-size gels for the scWB[8]. In that scenario, Duncombe et al. modulated the amount of light the gel was exposed to create the gradient. For the z-direction system, we have modulated the amount of oxygen the gel is exposed to.

4.5 Conclusions

This chapter focuses on the construction and testing of z-direction gradient pore-size polyacrylamide gels. We verified the gradient formation by creating ratiometric images using two fluorescent indicators. We developed two methods for generating gradient pore-size gels, which both involve a two-step gel casting process. Firstly, a uniform gel with a target thickness of 1 mm was cast. In the first method, additional gel precursor was added to one side of the gel, allowing diffusion to create a gradient of gel precursor, which later becomes the

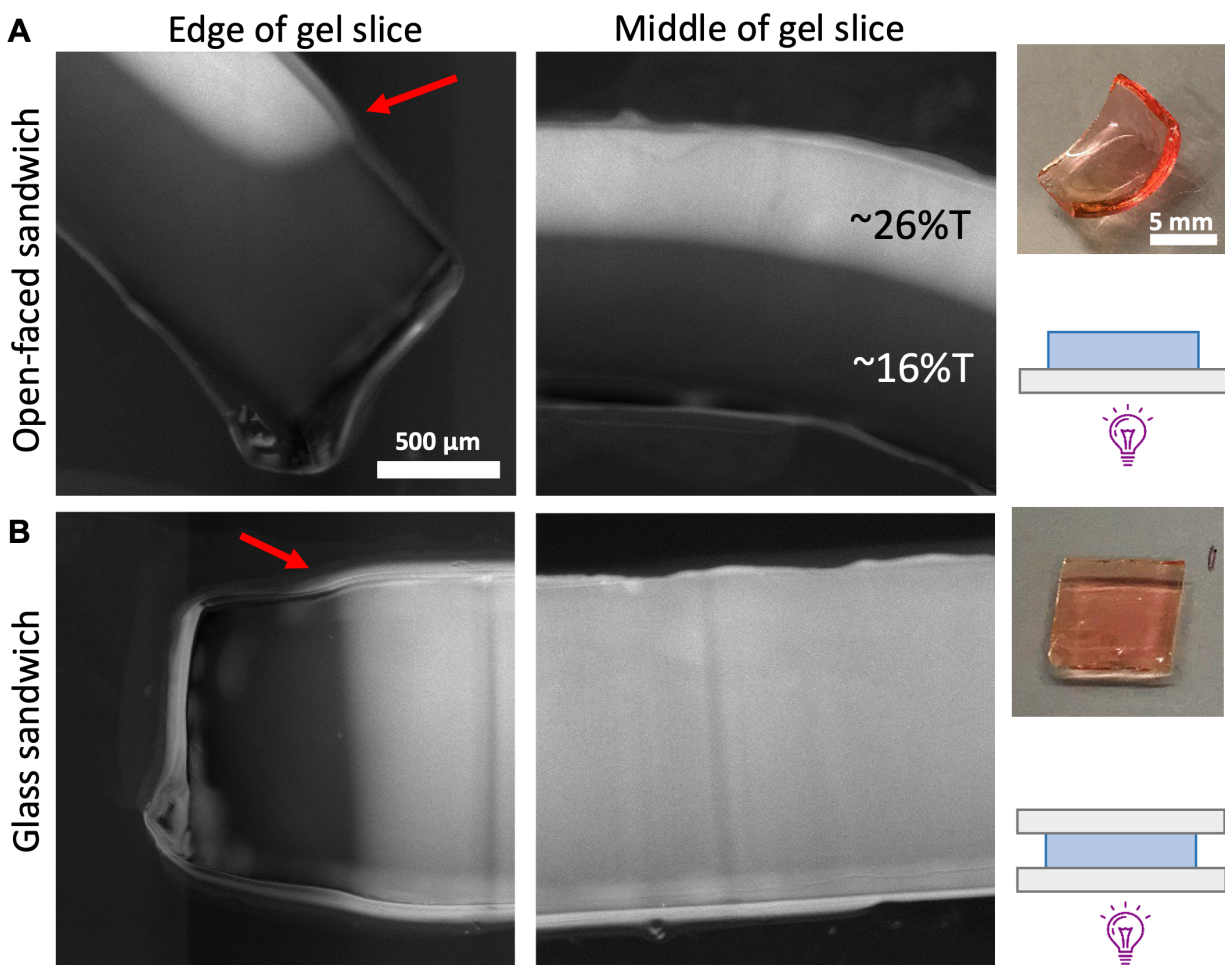


Figure 4.6: Oxygen-inhibited polymerization facilitates pore-size patterning. Both gels were labeled with FITC and soaked in 25%T gel precursor containing rhodamine B. After polymerization, excess rhodamine B was washed away. (A) When the gel is photopolymerized with the surface exposed to air (as shown in the schematic on the right), oxygen inhibits polymerization at the gel surface, creating a step change in pore size. The gel depicted represents $n = 2$ replicates. (B) When the gel is photopolymerized between two glass slides to limit gel exposure to air, the gel is uniformly polymerized except at the edge of the gel, which was still in contact with air. The gel depicted does not have replicates.

pore-size gradient after photopolymerization. In the second method, additional gel precursor was added to the entire 1 mm gel, and photopolymerization occurred in a gradient oxygen environment, leading to inhibited polymerization in the oxygen-rich regions compared to the relatively less oxygenated regions.

Next, we will evaluate the separation performance of gradient pore-size gels compared to uniform pore-size gels. Some specific questions of interest are: How much did the protein bands sharpen? By what percent did we decrease the separation distance needed to resolve a set range of molecular weights? How much did the separation resolution improve? As we move forward, one significant adjustment we plan to make to the proposed gradient pore-size gel is to enhance the accessibility of immunoreagents to all areas of the gel. One potential solution is to use an acid-labile cross-linker during the gradient formation step so that when it undergoes hydrolysis, the gel achieves a uniform porosity[8].

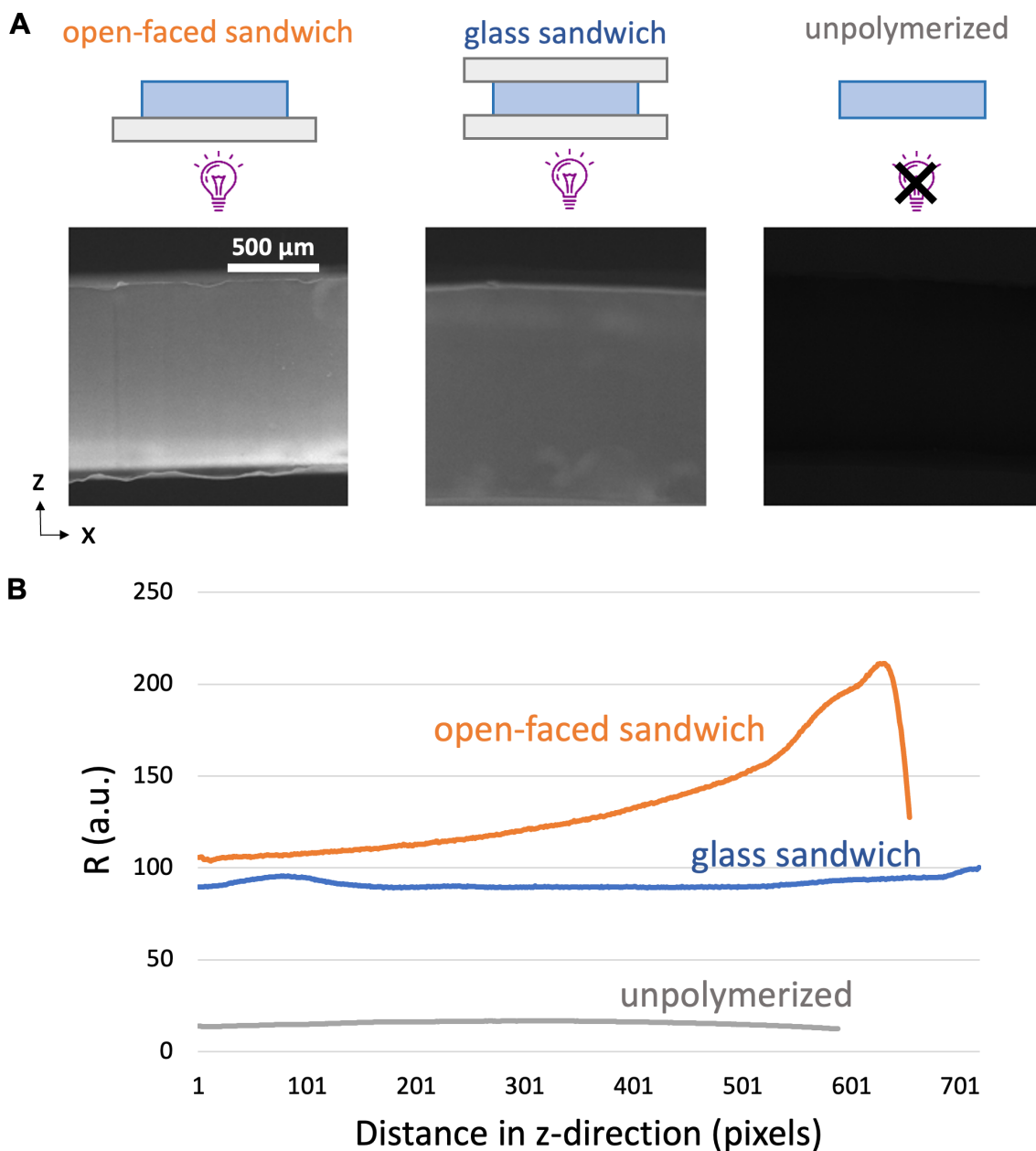


Figure 4.7: Use of oxygen to modulate polymerization efficiency to create oxygen gradient-driven pore-size gradient gel. (A) Schematics and ratiometric images of different gel photopolymerization conditions. All gels were labeled with FITC and soaked in 25%T gel precursor containing rhodamine B. Gels were degassed in a nitrogen chamber for approximately 2 minutes before polymerization. (B) Intensity profile plot for ratiometric images polymerized under the conditions described in the schematic of (A). The open-faced sandwich condition produces a pore-size gradient gel. Gels depicted do not have replicates.

References

- (1) Grist, S. M.; Mourdoukoutas, A. P.; Herr, A. E. *Nature Communications* **2020**, *11*, 6237.
- (2) Herr, A. E.; Grist, S. M.; Kang, C.-C.; Sefunc, B. G.; Vlassakis, J. Tissue Projection Electrophoretic Separation of Protein, US20210048410A1, 2021.
- (3) Rodbard, D.; Kapadia, G.; Chrambach, A. *Analytical Biochemistry* **1971**, *40*, 135–157.
- (4) Singh, A. K.; Chandrasekaran, A. *Single Cell Protein Analysis Methods and Protocols Methods in Molecular Biology 1346*; tech. rep.; 2015.
- (5) Hughes, A. J.; Spelke, D. P.; Xu, Z.; Kang, C.-C.; Schaffer, D. V.; Herr, A. E. *Nature Methods* **2014**, *11*, 749–755.
- (6) Huang, S. *Development (Cambridge, England)* **2009**, *136*, 3853–62.
- (7) Marusyk, A.; Almendro, V.; Polyak, K. *Nature Reviews Cancer* **2012**, *12*, 323–334.
- (8) Duncombe, T. A.; Kang, C.-C.; Maity, S.; Ward, T. M.; Pegram, M. D.; Murthy, N.; Herr, A. E. *Advanced Materials* **2016**, *28*, 327–334.
- (9) Walker, J. M. In *Proteins*; Humana Press: New Jersey, 1984; Vol. 1, pp 57–62.
- (10) Simpson, R. J. *Cold Spring Harbor Protocols* **2010**, *2010*, pdb.prot5411.
- (11) Ungerböck, B.; Charwat, V.; Ertl, P.; Mayr, T. *Lab on a Chip* **2013**, *13*, 1593–1601.
- (12) Menter, P. *Acrylamide Polymerization — A Practical Approach*, en, 2000.
- (13) Hulst, A. C.; Hens, H. J. H.; Buitelaar, R. M.; Tramper, J. *Biotechnology Techniques* **1989**, *3*, 199–204.
- (14) Hepworth, S. J.; Leach, M. O.; Doran, S. J. *Physics in Medicine and Biology* **1999**, *44*, 1875–1884.

Chapter 5

Combining Hydrodynamic Trapping and Electrical Lysis for Single-Cell Electrophoresis

This work was performed in collaboration with Dr. Yang Liu.

5.1 Abstract

Electrophoretic assays are capable of elucidating proteoforms, which are often indistinguishable with canonical antibody-based protein assays and mass spectrometry. Single-cell electrophoresis (scEP) is a powerful method for separating proteoforms based on size and charge within individual cells. However, the current implementation of scEP is limited to open microfluidic devices, which precludes its integration with enclosed microfluidic formats (e.g., for microchannel electrophoresis), which could introduce additional performance improvements and separation modalities to scEP. In this study, we present an enclosed microfluidic scEP device that combines hydrodynamic cell trapping, electrical lysis, and protein electrophoresis. The device incorporates a hybrid polydimethylsiloxane (PDMS)-hydrogel hydrodynamic cell trapping component that also functions as an electrical lysis component. While challenges regarding poor cell settling efficiencies ($\sim 1\%$) and cross-talk between microchannels remain, we demonstrate proof-of-concept of hydrodynamic cell trapping followed by rapid (< 1 second) and non-denaturing electrical cell lysis, preserving protein native state during both lysis and electrophoresis.

5.2 Introduction

Single-cell proteomics has garnered immense significance in various fields of biological and medical research[1–4]. Single-cell electrophoresis (scEP) techniques, such as single-cell western blotting (scWB)[5, 6] and single-cell isoelectric focusing (scIEF)[7], provide valuable

insights into cell-to-cell proteoform heterogeneity, offering critical information that is often obscured in ensemble measurements[8, 9]. While scEP serves as a powerful single-cell analysis tool, its “open microfluidic” design presents a challenge for integrating scEP with enclosed electrophoretic formats.

Current scEP microdevices are designed as “open microfluidic” platforms, consisting of a thin layer of polyacrylamide (PA) gel adhered to a glass slide or other support. The fundamental steps of scEP involve the following: (1) single-cell isolation, (2) cell lysis, (3) protein electrophoresis, and (4) immunostaining[10]. Following the isolation of individual cells in microwells (step 1), a buffer that facilitates chemical lysis (step 2) is rapidly introduced to initiate in-well cell lysis and protein solubilization. Single-cell settling and simultaneous lysis allow multiple cells to be analyzed in parallel on the same platform, which facilitates the comparison of protein expression levels across different cells and provides valuable insights into cellular heterogeneity within a population[5, 11].

Single-cell analysis in an enclosed electrophoretic format (e.g., microchannel) could offer performance improvements (e.g., eliminate cathodic drift in isoelectric focusing as discussed in Chapter 3) or additional separation modalities (e.g., two-dimensional electrophoresis[12] or isotachopheresis[13]) compared to current open hydrogel formats. However, a major challenge to moving to an enclosed design is loss of access to microwells for (1) single-cell settling and (2) the rapid delivery of lysis buffer to all microwells near simultaneously. Several methods of single-cell settling have been employed for scEP, including gravitational settling[5], centrifugation-based seating[14], and mouth-controlled manipulation[15], but all these methods utilized an open hydrogel analytical layer. Hence, there is a need to engineer a single-cell isolation and lysis strategy that introduces the single-cell lysate to the separation microchannel with minimal dilution.

Hydrodynamic cell trapping is a promising approach that allows the precise manipulation and confinement of individual cells in enclosed microfluidic devices[16, 17]. By controlling fluid flow via geometric constraints, hydrodynamic trapping enables the immobilization of cells at specific locations within a device, facilitating subsequent analysis and experimentation[18]. In parallel, electrical lysis methods have emerged as powerful tools for cell disruption, enabling the release of intracellular contents for downstream analysis[19].

We propose a novel approach that combines hydrodynamic cell trapping and electrical lysis for single-cell electrophoresis in an enclosed microfluidic device. Various formats can enable hydrodynamic cell trapping, including serpentine[18, 20–23] and grid[24, 25] arrangements. To accommodate the separation microchannels, we opted for a linear arrangement inspired by a previously published design, where two parallel channels are interconnected through a series of cell traps[26]. However, whereas the previous design had sidewalls made entirely of PDMS[26], our device has sidewalls made of both PDMS and polyacrylamide (PA) gel, where the main role of the PA gel is to enable electrophoresis. Moreover, we take advantage of the geometry of the cell trap to produce a localized region of high electric field ($\sim 10^4$ - 10^5 V/m) to induce simultaneous cell lysis. In this study, we present the experimental setup, theory, simulations-guided design, results, and challenges of our approach to an enclosed scEP assay. We demonstrate hydrodynamic trapping to immobilize cells within

microfluidic cell traps, followed by localized electrical lysis to disrupt the cell membrane and release intracellular contents for electrophoresis. Additionally, we report key failure modes of hydrodynamic cell trapping in the hybrid PDMS-PA gel environment that lead to cell settling efficiencies of <1% and cross-talk between neighboring microchannels.

5.3 Materials and Methods

Device Design

The device is shown in Figure 5.1A and consists of a single polydimethylsiloxane (PDMS) layer assembled to a standard glass slide (VWR 48300-048). The design of the device is presented in Figure 5.1B and consists of channels (316 total) in between flanking reservoirs (4-mm tall, 65-mm long, and 2.677-mm wide). The reservoirs are used for delivery of PA gel precursor during device fabrication, as well as insertion of electrodes during device operation. Each channel can accommodate a single cell for analysis and consists of three regions (Figure 5.1C): (1) a PA gel (2.136-mm long, 100- μm wide) prevents cells from escaping into the cathode reservoir by providing a physical barrier, while serving as an electrically conductive medium for the subsequent application of an electric field for electrical cell lysis and protein electrophoresis, (2) a gel-free cell trapping region (Figure 5.1D), and (3) a PA gel (3.6215-mm long, 100- μm wide) for electrophoretic protein separation, capture, and readout.

Device Fabrication

The full workflow schematic for fabrication of the device is shown in Figure 5.2.

Device Assembly. The PDMS device was fabricated by soft lithography techniques. To create through-holes for the reservoirs, laser-cut acrylic posts (10-mm tall, 65-mm long, and 2.677-mm wide) were attached with double-sided tape (Scotch Permanent Double Sided Tape) to a silicon wafer (WaferPro C04009) patterned with 28- μm tall SU8 2025 (MicroChem Y111069) features using a custom-designed chrome mask (Front Range Photomask) and coated with trichloro(1H,1H,2H,2H-perfluorooctyl)silane (Sigma-Aldrich 448931) (Figure 5.2Ai). RTV615 PDMS (Momentive) was mixed at a 10:1 ratio, degassed, and poured over the assembled acrylic and silicon mold (Figure 5.2Aii). Enough PDMS was poured so that the PDMS layer would be 4-mm thick, and therefore the final reservoir features 4-mm tall. The PDMS was cured at 80°C for 2 hours, removed from the mold, and then a biopsy punch was used to make 1 mm diameter inlet and outlet holes. Finally, the PDMS layer was plasma bonded to a microscope slide (Figure 5.2Aiii).

Gel Fabrication. The next step is to polymerize PA gel in the PDMS microchannels. The microchannels are first filled with a 10% w/v benzophenone (Sigma B9300) in acetone solution for 3 minutes, via application of the benzophenone solution at the reservoirs. The benzophenone serves as an oxygen scavenger to prevent inhibition of the polyacrylamide free radical polymerization reaction²⁷. The entire device is then dunked in methanol and dried with a gentle nitrogen stream applied at the reservoirs. The entire device is then submerged in a 50 mL Falcon tube filled with a 12 %T PA gel precursor prepared from

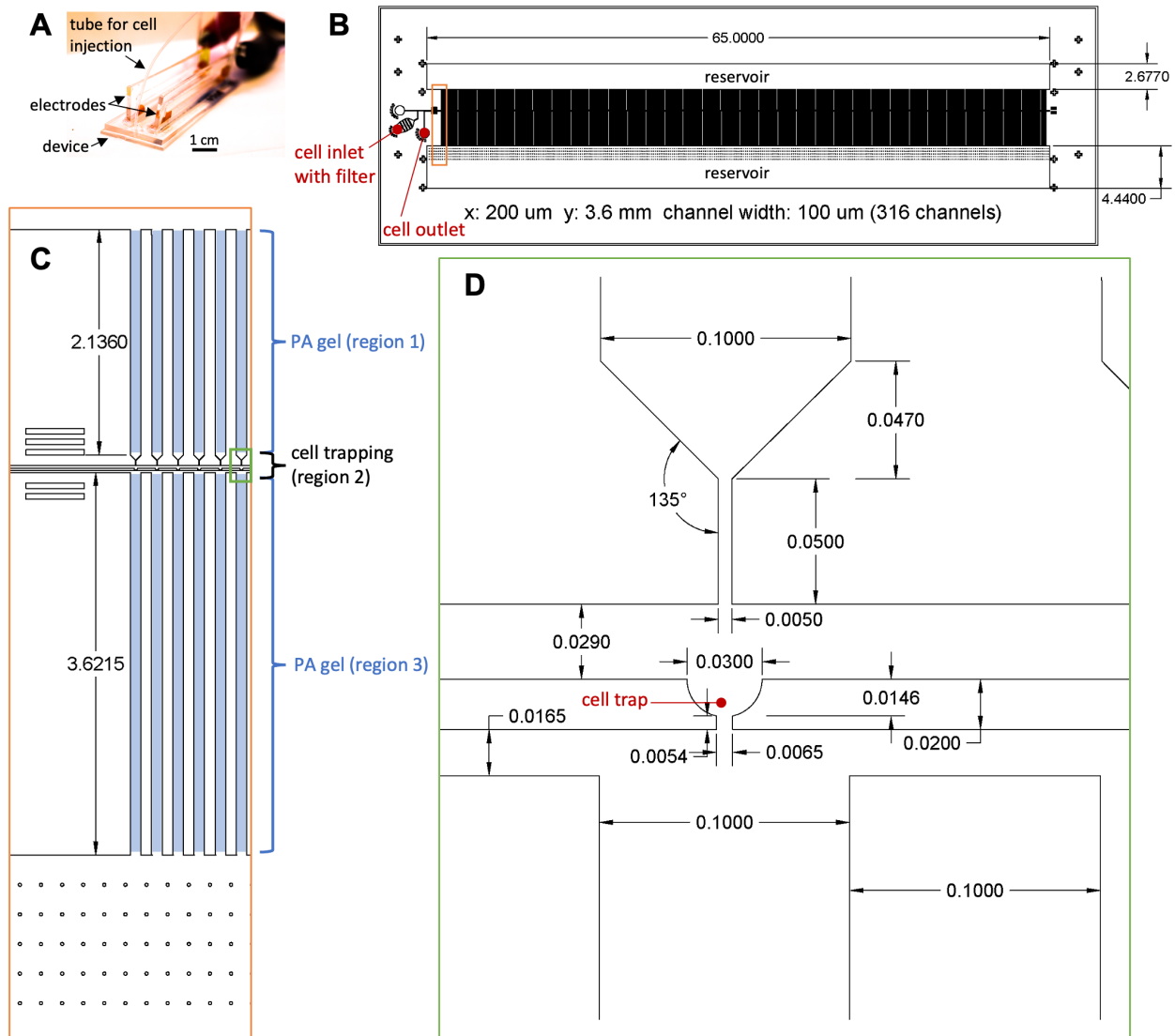


Figure 5.1: Overview of enclosed single-cell electrophoresis device design. (A) Image of device during operation. (B-D) CAD renderings of device architecture with dimensions, focusing on (B) the entire device, (B) the microchannels with PA gel and cell trapping regions labeled, and (C) the cell trap region. Units for all dimensions are in millimeters.

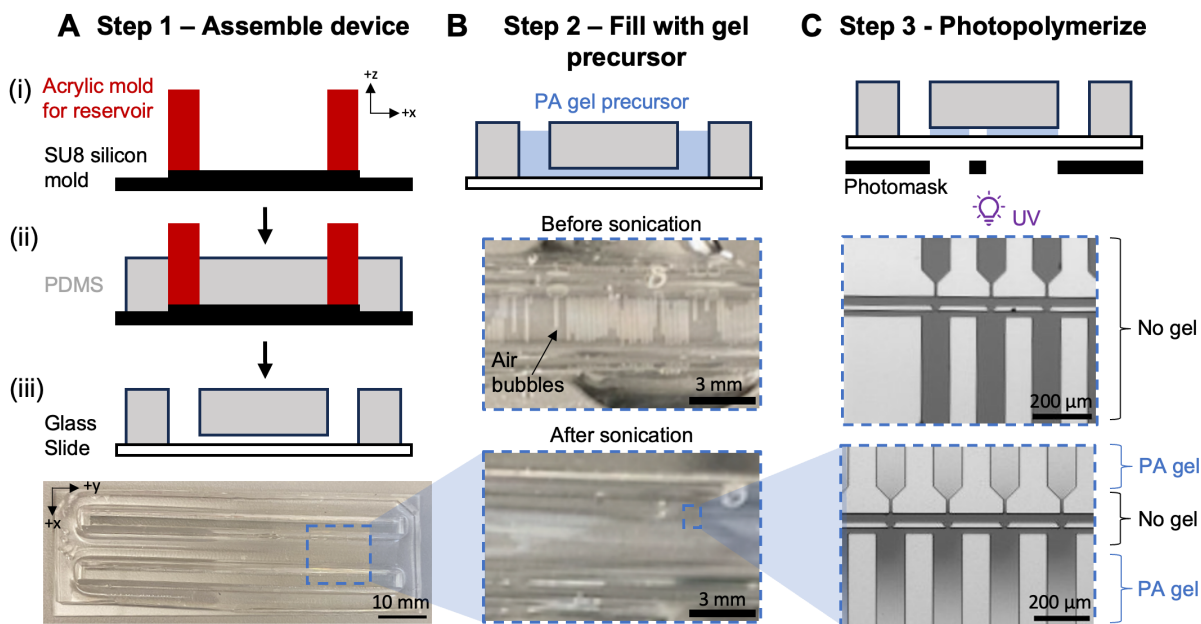


Figure 5.2: Overview of microfluidic device fabrication. (A) PDMS is molded and assembled onto a glass slide. (B) Sonication under vacuum of device submerged in gel precursor removes bubbles trapped in device. Before sonication under vacuum, bubbles are clearly visible by eye and microchannel features are visible. After sonication under vacuum, microchannel features are not visible as PA gel precursor and PDMS have a similar index of refraction. (C) Photopolymerization of gel within microchannels leaves a gel-free region for cell trapping. Presence of gel confirmed by flowing dye into device and observing its path.

30%T 29:1 acrylamide/bis-acrylamide solution (Sigma A3574), 1X Tris-Glycine Buffer (Bio-Rad 1610734), and 1% w/v UV photoinitiator 2,2-Azobis(2-methyl-N-(2-hydroxyethyl) propionamide) (VA086, Wako Chemicals 01319342). A small hole is punched into the Falcon tub lid and a vacuum line is attached to sonicate the entire device under vacuum for 10 minutes to ensure the microchannels are filled with gel precursor (Figure 5.2B). The gel is photopolymerized for 45 seconds at 20 mW/cm^2 light intensity using an OAI Model 200 Tabletop Mask Aligner. A mylar photomask (Artnet Pro) was used to polymerize only the gel inside regions (1) and (3) and allow the cell trapping region (2) to remain gel-free (Figure 5.2C). Excess gel precursor was removed from the reservoirs and replaced with $400 \mu\text{L}$ 1X Tris-glycine buffer. Devices remained in 1X Tris-glycine buffer for a minimum of 17 hours and maximum of 7 days before use for the experiments in this chapter, although longer storage of devices is likely possible.

Cell Culture

An MCF7 human breast cancer cell line genetically modified to stably express green fluores-

cent protein (GFP) was obtained from the American Type Culture Collection, authenticated by short tandem repeat analysis, and tested negative for mycoplasma. The MCF7-GFP cells were maintained in a humidified 37°C incubator kept at 5% CO₂ with RPMI media (Gibco 11875-093) supplemented with 1% penicillin/streptomycin (Invitrogen 15140122) and 10% Fetal Bovine Serum (FBS, Gemini Bio-Products 100-106). Cells were detached with 0.05% Trypsin-EDTA (ThermoFisher 25300-120) and resuspended in 4°C 1× phosphate-buffered saline (PBS, Thermo Fisher Scientific 10010023) with 1% w/v Pluronic F-127 (Sigma P2443) to generate cell suspensions. The cells were kept wrapped in foil and on ice for up to 1 hour until use.

A K562 suspension cell line genetically modified to express marker LifeAct:GFP was maintained in a humidified 37°C incubator kept at 5% CO₂ with RPMI media supplemented with 1 mM sodium pyruvate (Life Technologies 11360-070) and 10% FBS. Cells were kept at 37°C in RPMI media until use.

Device Operation

Hydrodynamic bead trapping. 20- μ m polystyrene beads (ChemGenes MACOSKO-2011-10) were diluted in deionized water to 100,000 beads/mL. The bead suspension is loaded onto a syringe pump (Chemyx Fusion 4000 X) and connected to the device with polytetrafluoroethylene (PTFE) tubing (Alpha Wire TFT20024). The bead suspension is introduced into the device at a flow rate of 0.01 μ L/min.

Hydrodynamic cell trapping. A solution of 2% ultra-low gelling agarose (Sigma A5030) is prepared by adding 5 mL of 1X PBS to 100 mg of ultra-low gelling agarose, and dissolving in a microwave in 2 second intervals with stirring in between. Once the agarose is dissolved, the solution is maintained at 37°C. The MCF7-GFP or K562-LifeAct-GFP cell suspension (\sim 1 million cells/mL in 1X PBS) was mixed in equal parts with the 2% agarose solution, for a final density of \sim 500,000 cells/mL in 1% agarose. The cell/agarose suspension is loaded onto a 1 mL syringe (BD 309628) and connected to the device with PTFE tubing. For cell trapping experiments, we did not apply any additional pressure to the syringe using the syringe pump. The act of inserting the tubing into the device itself provided sufficient pressure to enable the flow of cells into the cell traps. Once hydrodynamic cell trapping is complete (\sim 10-20 minutes), the tubing is disconnected from the device, and the device is placed on ice for 10 minutes to allow the agarose to gel. The cell traps are then inspected under brightfield or fluorescence.

Electrophoresis. After hydrodynamic cell trapping, reusable electrodes made of platinum wire in an acrylic plastic holder were inserted into the 2 reservoirs. Using a high voltage power supply (Bio-Rad PowerPac HV Power Supply), 200 V or 32 V were applied across the electrodes, spaced 8 mm apart, to induce electrical cell lysis and protein electrophoresis.

Fluorescence Imaging

Hydrodynamic cell trapping and electrical lysis experiments were imaged using an Olympus IX-51 inverted epifluorescence microscope equipped with an iPhone 11 Pro Max as a camera, ASI motorized stage, and X-cite exacte illumination system from Lumen Dynamics.

Numerical Simulation

Computational fluid dynamics. Finite element simulations for hydrodynamic flow in the cell trapping region were performed using the Laminar Flow physics in COMSOL Multiphysics 5.6 to solve the Navier-Stokes equations for conservation of momentum and the continuity equation for conservation of mass. A 2D model was used for the simulation since all device features had the same height. A portion of the geometry for the hydrodynamic flow simulation is presented in Figure 5.4A. We assumed the PA gel regions to be impermeable to flow (no flux) in our simulations since interstitial flow through the PA gel would be negligible compared to pressure-driven flow in the gel-free cell trapping region. Flow boundary conditions on the cell trap sidewalls were “no slip”. The initial velocity in the cell trapping region is zero. The inlet has a 0.001 m s^{-1} bulk fluid velocity boundary condition and the outlet has a 0 Pa pressure boundary condition. The model was meshed with a physics-controlled mesh. A stationary analysis was used to model the hydrodynamic flow profile at steady state. After running the model, we assessed the ratio of the flow rate through the inlet channel (m^2s^{-1}) versus the flow rate through the first trap gap (m^2s^{-1}).

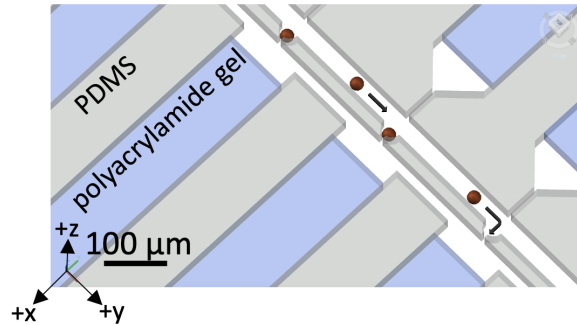
Computational electric field simulations. Finite element simulations for electric fields in the cell trapping region were performed using the Electric Currents physics in COMSOL Multiphysics 5.6 to solve a current conservation equation based on Ohm’s law using the scalar electric potential as the dependent variable. A 2D model was used for the simulation since all device features had the same height. A portion of the geometry for the electric field simulation is presented in Figure 5.6B. The effect of the PA gel on conductivity was assumed to be negligible since PA gel does not contribute significantly to conductivity unless the buffer has low ($<10^{-3} \text{ M}$) ionic strength[27, 28], and the 1X Tris-glycine buffer ($\sim 0.1 \text{ M}$) does not have low ionic strength. The electric potential at the cathode was set to either 32 V or 200 V and the electric potential at the anode was set to 0 V. The model was meshed with a physics-controlled mesh. A stationary analysis was used to model the electric field profile at steady state. After running the model, we assessed the electric field strength (V/m) at different regions of the device.

5.4 Results and Discussion

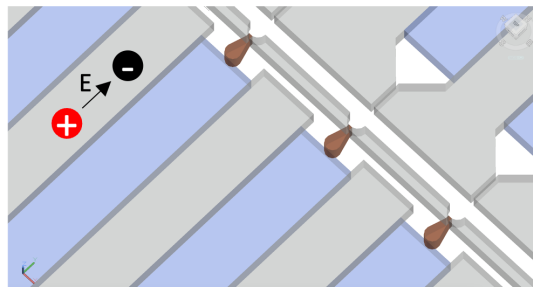
The subsequent subsections will describe the design choices employed when combining hydrodynamic cell trapping with electrical lysis for single-cell electrophoresis. Although the device geometry parameters for hydrodynamic cell trapping and electrical lysis are interconnected, we accorded higher priority to the design for hydrodynamic cell trapping due to its more stringent constraints based on cell size compared to electrical lysis. An overview of the enclosed single-cell electrophoresis device operation is illustrated in Figure 5.3.

Theory and simulation of hydrodynamic cell trapping

Step 1: Hydrodynamic cell trapping



Step 2: Electrical cell lysis



Step 3: Electrophoresis



Figure 5.3: Device combines hydrodynamic trapping and electrical lysis for single-cell protein electrophoresis.

Hydrodynamic cell trapping is a method for isolating single cells within microfluidic devices. We devised hydrodynamic cell traps, with each trap designed to address an individual separation microchannel for subsequent analysis. Figure 5.4A offers an overview of the device geometry. Contrary to other designs where the trap sidewalls are made entirely of PDMS, our device incorporates PA gel membranes at the top and bottom of the trap (Figure 5.1C). This strategic modification serves multiple purposes: preventing cell escape, providing a medium for protein separation, and establishing a path for electricity. The critical design parameter for hydrodynamic cell trapping is the flow ratio, R_{flow} :

$$R_{flow} = \frac{Q_{trap}}{Q_{ic}} \quad (5.1)$$

where Q_{trap} is the flow rate through the trap gap (m^2s^{-1}) and Q_{ic} is the flow rate through the inlet channel (m^2s^{-1} , labeled on Figure 5.4B). To promote sequential, single-cell trapping, R_{flow} should be greater than 1, which means the bulk of the flow is through the trap gap, and therefore a cell carried by the flow is directed to the cell trap[18]. The flow through the trap gap is subsequently blocked by the cell, enabling the process to repeat at the next trap in the series until all or a majority of traps are occupied by a single cell. A previous study empirically determined that when R_{flow} is ≤ 1.0 , large numbers of empty traps ($\sim 65\%$) were observed, but when R_{flow} is ≥ 1.4 , the device enabled efficient single cell settling ($\sim 80\%$), with few traps containing multiple cells ($\sim 20\%$)[22]. Therefore, we set the target design specification of R_{flow} to ~ 1.4 .

Numerical simulations were employed to model the hydrodynamic flow within the cell trapping region, enabling the quantification of resulting flow profiles with varying geometry parameters. These simulations served to optimize cell trapping efficiency and determine fabrication error tolerances, specifically, alignment of the photomask for photopolymerization of the PA gel membranes. For the purpose of enhancing cell trapping efficiency, we simulated R_{flow} for various geometries, and the summary of these simulations can be found in Table 5.1. Incorporating a High Resistance Channel in the device design was crucial to prevent cell escape into the Top Channel. Additionally, the inclusion of Top and Bottom Channel Lengths ensured that the cell trapping region remained free of gel during photopolymerization (labeled on Figure 5.4A).

Among the geometry parameters tested, the Outlet Channel Width and Inlet Channel Width exhibited the most significant impact on R_{flow} . For instance, reducing the Outlet Channel Width from $18.5 \mu m$ to $16 \mu m$ led to an increase in R_{flow} from 1.33 to 1.72. However, it was essential to consider the potential blockage risks associated with a narrower Outlet Channel. Consequently, we chose an Outlet Channel Width of $16.5 \mu m$ as a balanced compromise (R_{flow} of 1.38). On the other hand, the Top Channel and High Resistance Channel had a less notable effect on R_{flow} . Notably, increasing the Top Channel Width from $50 \mu m$ to $100 \mu m$ showed no effect on R_{flow} . As for the Bottom Channel geometry, it had a moderate impact on R_{flow} . For example, decreasing the Bottom Channel Length from $25 \mu m$ to $10 \mu m$ increased R_{flow} from 1.16 to 1.22. Thus, it's important to keep in mind during the photomask alignment that less gel free space should be left in the Bot-

Table 5.1: R_{flow} obtained for the first cell trap for various geometries. Highlighted values are the modified parameters from the previous row.

Inlet Channel Width (μm)	Outlet Channel Width (μm)	Bottom Channel Length (μm)	Bottom Channel Width (μm)	High Resistance Channel Length (μm)	High Resistance Channel Width (μm)	Top Channel Length (μm)	Top Channel Width (μm)	R_{flow} (Goal =1.4)
30	18.5	0	0	70	6	500	100	1.29
30	18.5	0	0	70	6	250	100	1.31
30	18.5	0	0	70	5	250	100	1.33
30	18.5	100	32	70	5	250	100	1.27
30	18.5	0	0	100	5	250	100	1.32
30	18.5	0	0	20	5	250	100	1.33
30	18.5	0	0	20	5	250	50	1.33
30	16	0	0	20	5	250	50	1.72
30	16	0	0	20	5	250	100	1.72
30	17	0	0	20	5	250	100	1.54
30	17	0	0	50	5	250	100	1.53
30	17	100	32	50	5	250	100	1.46
30	17	25	100	50	5	250	100	1.16
30	17	10	100	50	5	250	100	1.22
30	17	10	100	100	5	250	100	1.21
29	17	10	100	50	5	250	100	1.24
29	16.5	10	100	50	5	250	100	1.38

tom Channel. Finally, after careful consideration, we selected the final device geometry with an R_{flow} of 1.38, which is summarized in the last row of Table 5.1 and depicted in Figure 5.4B.

Hydrodynamic cell trapping isolates cells

We next sought out to evaluate the performance of the hydrodynamic cell traps. Figure 5.5 summarizes bead and cell trapping results. In Figure 5.5A, 20- μm polystyrene beads ($\sim 100,000$ beads/mL in deionized water) were delivered to the device at a flow rate of 0.01 $\mu\text{L}/\text{min}$. The device successfully trapped 7 beads, each single bead occupying a single bead trap out of 316 total bead traps (bead settling efficiency of 2.2%). In Figure 5.5B, we used K562-LifeAct-GFP cells (at a concentration of $\sim 500,000$ cells/mL in 1% agarose) and introduced the cells into the device. The results showed that 4 out of 316 cell traps were occupied, with each cell trap containing approximately 1 to 3 cells. Cells sometimes overlap in the cell traps, confounding precise counting of cell occupancy per cell trap. In both the bead

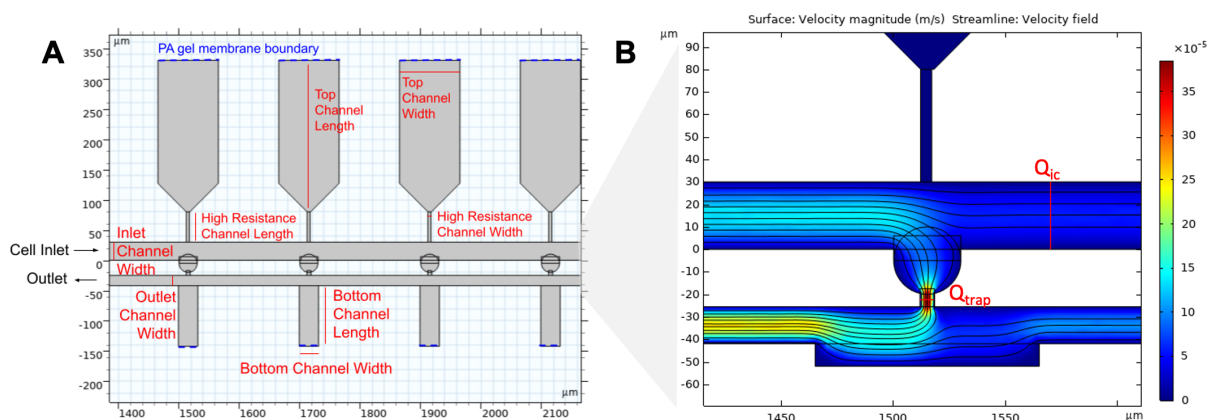


Figure 5.4: Simulation of hydrodynamic cell trapping. (A) Geometry of hydrodynamic cell traps with key parameters labeled. (B) Velocity magnitude plot of first cell trap with streamlines showing that majority of flow passes through the trap gap (Q_{trap}) versus the inlet channel (Q_{ic}).

and cell trapping experiments, the cell traps were sequentially occupied from left to right, as expected. However, all 5 devices tested exhibited poor cell settling efficiencies. Only 1 to 4 cell traps out of the total 316 available cell traps per device were occupied (cell settling efficiencies of $\sim 0.3\%$ to $\sim 1.3\%$), and in some cases, multiple cell occupancy occurred instead of the desired single cell occupancy.

Figures 5.5C and 5.5D illustrate the most common failure modes observed during cell trapping. The cell traps are confined by two PA gel boundaries (regions (1) and (3) as shown in Figure 5.1C and Figure 5.2C). In certain devices, we noticed gel tearing occurring in region (1) (Figure 5.5C) or (3) (Figure 5.5D) or both, as evidenced by the path of the cells. This allowed some cells to escape into the anode or cathode reservoirs, instead of being retained in the designated cell trapping region. Our hypothesis is that the act of inserting the tubing into the device leads to an excess of pressure at the first cell trap, resulting in the rupture of the gel membranes, since this failure mode (shown in Figures 5.5C and 5.5D) was observed regardless of whether the syringe pump was used to flow in cells or not. In an earlier prototype of the device, the PA gel was 6 %T compared to the 12 %T gel used in all experiments in this chapter. The 6 %T devices experienced gel tearing in every device tested. We hypothesized that increasing the stiffness of the PA gel by increasing the percentage of total acrylamide concentration (%T)[29] could increase its structural integrity and mitigate the gel tearing failure mode. The 12 %T devices experienced gel tearing in only $\sim 50\%$ of the devices tested ($n = 12$), but the gel tearing failure mode was not fully eliminated (Figures 5.5C and 5.5D).

Another failure mode that adversely affected the efficiency of the cell traps involved

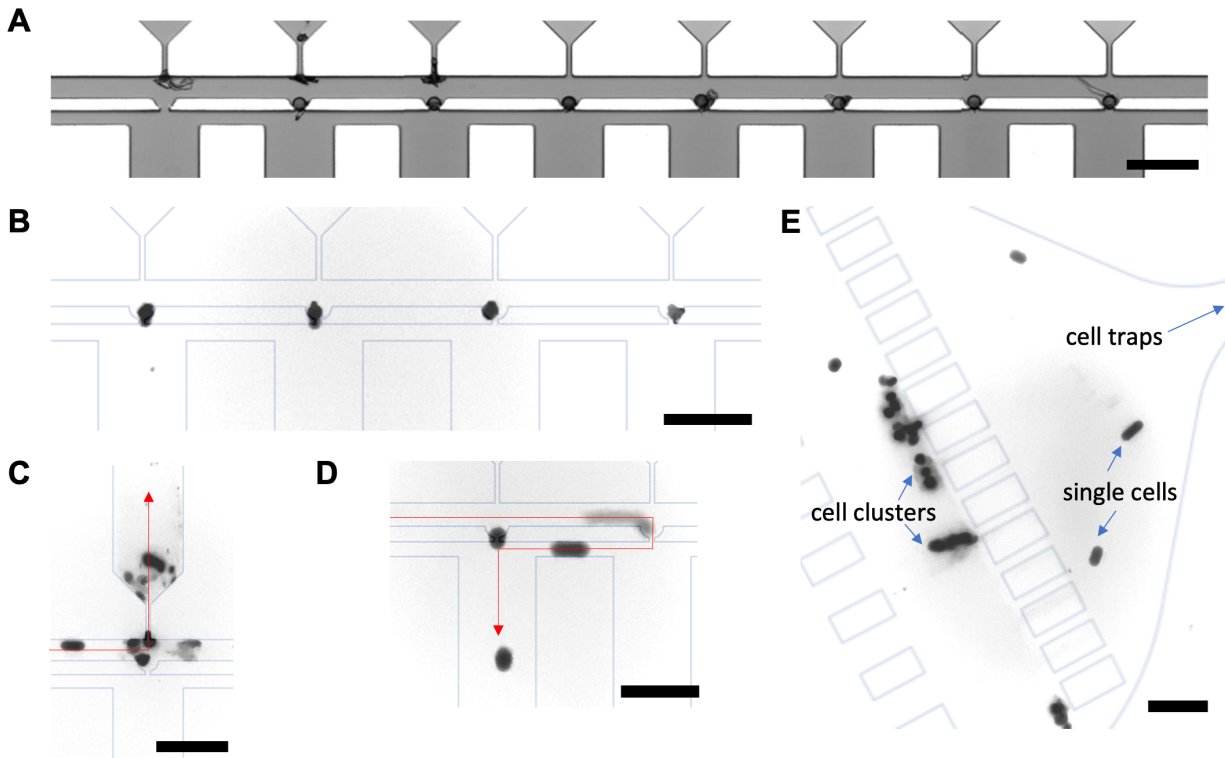


Figure 5.5: Experimental results of hydrodynamic trapping. (A) Hydrodynamic trapping of 20- μm polystyrene beads results in single bead occupancy per trap ($n = 1$ device). (B) Hydrodynamic trapping of K562-LifeAct-GFP cells results in ~ 1 -3 cell occupancy per trap. (C) Cell trapping failure mode where gel membrane is compromised allowing for cell escape instead of trapping cells in the appropriate cell traps. (D) Similar failure mode as in (C) with a compromised gel membrane and additionally demonstrating cell escape through trap gap. (E) Cell filter blocks cell clusters from entering cell trapping region. (B-E) Inverted fluorescence micrographs with PDMS boundaries depicted in blue outline. Red arrow shows the general path for cells. Micrographs have different brightness and contrast for better visualization. (B-E) are representative examples from $n = 5$ devices. Scale bar is 100 μm for all.

cells escaping through the trap gap, as shown in Figure 5.5D. We conducted cell trapping experiments using both MCF7-GFP cells ($\sim 15\text{-}17\ \mu\text{m}$ diameter) and K562-LifeAct-GFP cells ($\sim 22\ \mu\text{m}$ diameter). Both cell types demonstrated a similar tendency to squeeze through the $6.5\text{-}\mu\text{m}$ wide, $28\text{-}\mu\text{m}$ tall trap gap. The starting cell trap dimensions for this device were selected based on a prior design optimized for trapping MCF7 cells ($6.0\text{-}\mu\text{m}$ wide trap gap)[22]. When performing hydrodynamic flow simulations, we found that a $6.5\text{-}\mu\text{m}$ wide trap gap improved R_{flow} compared to a $6.0\text{-}\mu\text{m}$ wide trap gap ($R_{\text{flow}} = 1.07$ for $6.0\text{-}\mu\text{m}$ wide trap gap versus $R_{\text{flow}} = 1.24$ with $6.5\text{-}\mu\text{m}$ wide trap gap). We optimized our photolithography protocol to achieve the $6.5\text{-}\mu\text{m}$ wide feature in our SU-8 mold ($6.495\ \mu\text{m}$, $\text{SD} \pm 0.064\ \mu\text{m}$ for $n = 4$ SU-8 molds measured using optical profilometry). We hypothesize that the $0.5\text{-}\mu\text{m}$ or 8.3% increase in trap gap width in our device compared to Frimat et al. could have contributed to the cell escape failure mode[22].

A less frequently observed failure mode involved the accumulation of cells in the cell trapping region, leading to blockages. We attribute the mitigation of this failure mode to the following factors: Firstly, we maintained the cell suspension in 1% w/v Pluronic F-127 to discourage cell clumping[30]. Secondly, we hypothesize that the increased viscosity resulting from the 1% agarose aided in preventing cell clumping and settling in both the syringe and the device. Lastly, we incorporated an online cell filter[31] at the cell inlet to further mitigate the risk of blockages (Figure 5.5E). The filter acted as a safeguard, preventing any large cell clusters from entering the narrow channels essential for achieving a favorable flow ratio, R_{flow} , which is crucial for successful hydrodynamic cell trapping (Table 5.1). Overall, the careful consideration of cell clumping played a vital role in preventing blockages in the system, especially in the narrow channels necessary for efficient hydrodynamic cell trapping.

The hydrodynamic cell traps presented in this chapter did not achieve the high cell settling efficiencies ($>70\%$) accomplished by similar hydrodynamic cell trapping devices[17]. Comparing our device with a published device by Deng et al.[26] that features a similar linear cell trap arrangement (cell settling efficiencies of $>95\%$), two key differences likely resulted in the diminished cell trapping capabilities of our device (cell settling efficiency of $\sim 1\%$). First, the increased trap gap cross-sectional area in our device ($182\ \mu\text{m}^2$) versus Deng et al. ($50\ \mu\text{m}^2$)[26] resulted in cell escape through the trap gaps. To reduce the trap gap cross-sectional area in our device, we could utilize two-layer SU-8 mold fabrication to create a trap gap with reduced width and height, as was performed in Deng et al.[26]. Second, inclusion of PA gel membranes that are susceptible to tearing resulted in cell escape into the anode and cathode reservoirs. In future steps, several strategies could be employed to further mitigate the gel tearing failure mode. These include further enhancing the integrity of the gel membrane (e.g., by using a strengthening additive such as Rhinohide), reducing the initial pressure burst from the cell delivery tubing, or incorporating a built-in pressure release valve[32]. Implementing the aforementioned modifications in the present device could potentially minimize cell escape events, thus improving the overall performance of the cell trapping system.

Theory and simulation of electrical field strength

The hydrodynamic cell traps, in addition to providing a mechanism to isolate and hold single cells, also provide an electrical cell lysis mechanism. Moreover, we sought to design a device where the applied voltage potential driving electrical cell lysis simultaneously induces protein electrophoresis for lysate analysis.

Cells are sensitive to external electric fields due to the dielectric properties of cell membranes. Reversible electroporation is a process often used to temporarily compromise a cell membrane so that cargo (i.e., genes), can be introduced into a cell[33]. Above a certain electric field threshold, E_{th} , electroporation becomes irreversible. In this irreversible electroporation or cell lysis regime, the cell membrane is sufficiently disrupted that osmotic shock causes the cell to burst[34]. Previous work has found that irreversible electroporation of mammalian cells occurs with a continuously applied electric field of $\sim 10^5$ V/m[34–36]. One method to accomplish electrical cell lysis in a microfluidic device is to tune the device geometry to create a region of high electric field[36], which is the method we employed in our device.

In our device, the hydrodynamic cell traps double as a microfluidic resistor to create a region of high electric field within the trap gap (Figure 5.6A). The placement of the electrodes allows for simultaneous electrical lysis of all cells within the device. Our device consists of identical repeating units for each single-cell analysis (Figure 5.6B). From an electrical perspective, the identical repeating units can be modeled as parallel resistors since the units are connected across the same two points (anode and cathode reservoirs), creating multiple equivalent paths for current to flow (Figure 5.6A). The electrical properties of each repeating unit are the same, so we performed electric field simulations of only one single-cell analysis unit (Figure 5.6B-D). Since the features in our device are all the same height with variable widths, the electric field strength at each of the four main regions of the device (labeled in Figure 5.6A-B) is proportional to the relative resistance of each region via the following relationships[36]:

$$E_1 = I \frac{R_1}{l_1}; E_2 = I \frac{R_2}{l_2}, E_3 = I \frac{R_3}{l_3}, E_4 = I \frac{R_4}{l_4}, I = \frac{V}{R_t} \quad (5.2)$$

where E_{1-4} are the electric field strengths (V/m) in each of the 4 regions labeled in Figure 5.6A-B, R_{1-4} are the resistances in each region (Ω) proportional to the width (m) of the region, l_{1-4} is the length (m) of each region, I is the current (A), V is the operational voltage (V), and R_t is the sum of the resistances in all regions (Ω).

Using numerical simulations, we modulated the applied electric potential across the device electrodes to find the necessary potential to generate the high electric field strength, $\sim 10^5$ V/m, for cell lysis in the trap gap, as well as the moderate electric field strength, $\sim 10^3$ V/m to 10^4 V/m, for electrophoresis of proteins within the microchannel. For reference, 4×10^3 V/m is the typical electrical field strength employed for single-cell western blotting in an open microfluidic format[6], while typical electric field strengths for western blotting[37] and isoelectric focusing[38] in an enclosed, microchannel-based format range from 5×10^3 V/m to 3.5×10^4 V/m. We find that an electric potential of 200 V produces the target field strength for electrical lysis, 3.3×10^5 V/m, and electrophoresis, 2.5×10^4 V/m (Figure 5.6B-D). An

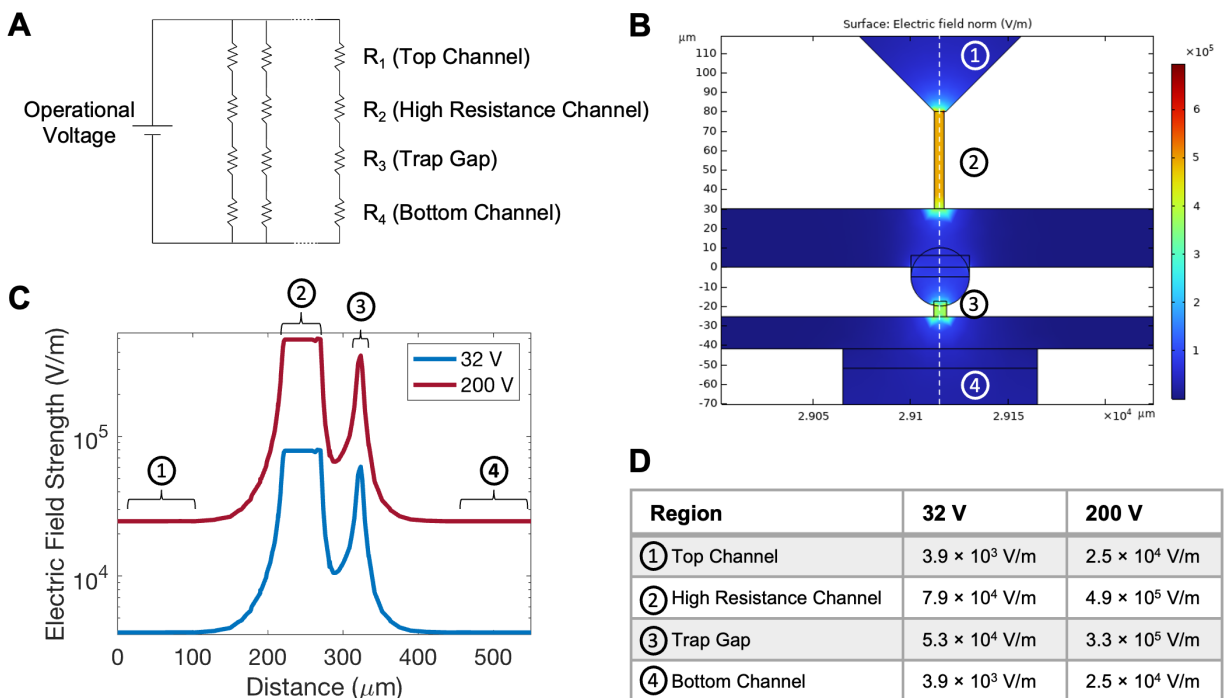


Figure 5.6: Simulation of electric field in cell trapping region and microchannels. (A) Schematic of series of resistors in parallel to represent voltage drop across various microfluidic components. (B) Numerical simulation of the electric field strength in the cell trap (200 V operational voltage). (C) Plot of electric field strength (on a log scale) in trap gap and microchannels across dotted white line in (B). (D) Average electric field strength across 4 regions highlighted in (B) and (C).

electric potential of 32 V provides a similar electric field strength for electrophoresis as is used for single-cell western blotting, 3.9×10^3 V/m, but the electric field strength in the trap gap, 5.3×10^4 V/m, was potentially in the reversible electroporation range ($<10^5$ V/m) instead of the irreversible electroporation range ($>10^5$ V/m)[34] (Figure 5.6D). However, previous research on the electrical lysis of acute myeloid leukemia (AML) cells has shown that when subjected to both a continuously applied electric field of 3×10^4 V/m and additional mechanical stress, a lower electric field strength is required for cell lysis compared to using a pulsed electric field alone[35, 39]. The cells in our device will also experience mechanical compression as the trap contracts from $30 \mu\text{m}$ diameter to $6.4 \mu\text{m}$. Based on this evidence, we decided to test whether an electric field of 5.3×10^4 V/m in the trap gap, with an applied potential of 32 V, could be sufficient for cell lysis (results discussed in the next section).

Electric potential induces electrical cell lysis and electrophoresis simultaneously

We have shown with a small fraction of our starting cell samples that hydrodynamic cell trapping can, in a few cases, position cells in the cell traps, which are designed to induce electrical cell lysis upon application of an electric field. Once a cell is trapped, a portion of the cell protrudes partially into the trap gap (Figure 5.5B and 5.5D). Upon application of an electric potential, the trap gap produces a high local electric field strength (Figure 5.6B-D). Cells in the high electric field area are lysed simultaneously in less than 1 second (Figure 5.7A).

When prototyping the device, we first used a cell suspension containing only MCF7-GFP cells and PBS. However, we observed that cell contents from electrically lysed cells rarely inject directly into the intended separation channel (Figure 5.7B), as would be predicted if electrophoretic force alone governed the transport of the cell lysate, but would instead flow into the channels used for hydrodynamic cell trapping (Figure 5.7D). We hypothesized that this cross-talk of cell contents between neighboring microchannels was due to residual flow from hydrodynamic cell trapping. We suspected there remained residual flow in our device, since small ($\sim 1 \mu\text{m}$) cell debris could be observed moving through the device, even after the tubing for cell delivery was removed. Residual flow arises as the pressure inside the microdevice can take some time to stabilize[40, 41].

To ensure we have a true single-cell electrophoresis assay, it is important to significantly reduce or eliminate cross-talk between neighboring microchannels. We turned to the use of a biologically compatible, thermoresponsive hydrogel (agarose) to eliminate residual flow in the device during electrical cell lysis and electrophoresis through gelation. The cell suspension contains 1% ultra-low gelling agarose and starts off in fluid form. We chose ultra-low gelling agarose since it has a gelling point of 8 - 17 $^{\circ}\text{C}$, which allows for easy hydrodynamic cell trapping at room temperature. Once hydrodynamic cell trapping is complete, the entire device is placed on ice and the agarose transitions from fluid form to gel form, with the goal of eliminating residual flow. The elimination of residual flow using agarose was confirmed by observing the cessation of all movement in the cell trapping region, including cell debris. Furthermore, syringes loaded with the cell/agarose suspension were detached from the device and placed alongside the device on ice to visually verify the gelation of the cell/agarose suspension. After agarose gelation, electrical cell lysis and electrophoresis is performed. In some instances, elimination of cross-talk using agarose-embedded cells was achieved (Figure 5.7C).

However, eliminating residual flow with agarose did not eliminate cross-talk of cell contents due to electrophoretic forces. As seen in Figure 5.7E, GFP released from lysed cells traveled in three directions, which would not be characteristic of residual flow. Residual flow was eliminated as the primary source of cross-talk in Figure 5.7E by observing that the three protein bands ceased to advance after the applied electric potential was stopped (data not shown). This observation indicated that electrophoretic force is the main cause of cross-talk in Figure 5.7E. While we can eliminate residual flow using gelation of the entire cell trapping region with agarose, the agarose does not prevent this “electrophoretic cross-talk”. One potential strategy to eliminate electrophoretic cross-talk would be to increase the resistivity between neighboring microchannels (i.e., by increasing microchannel-to-microchannel

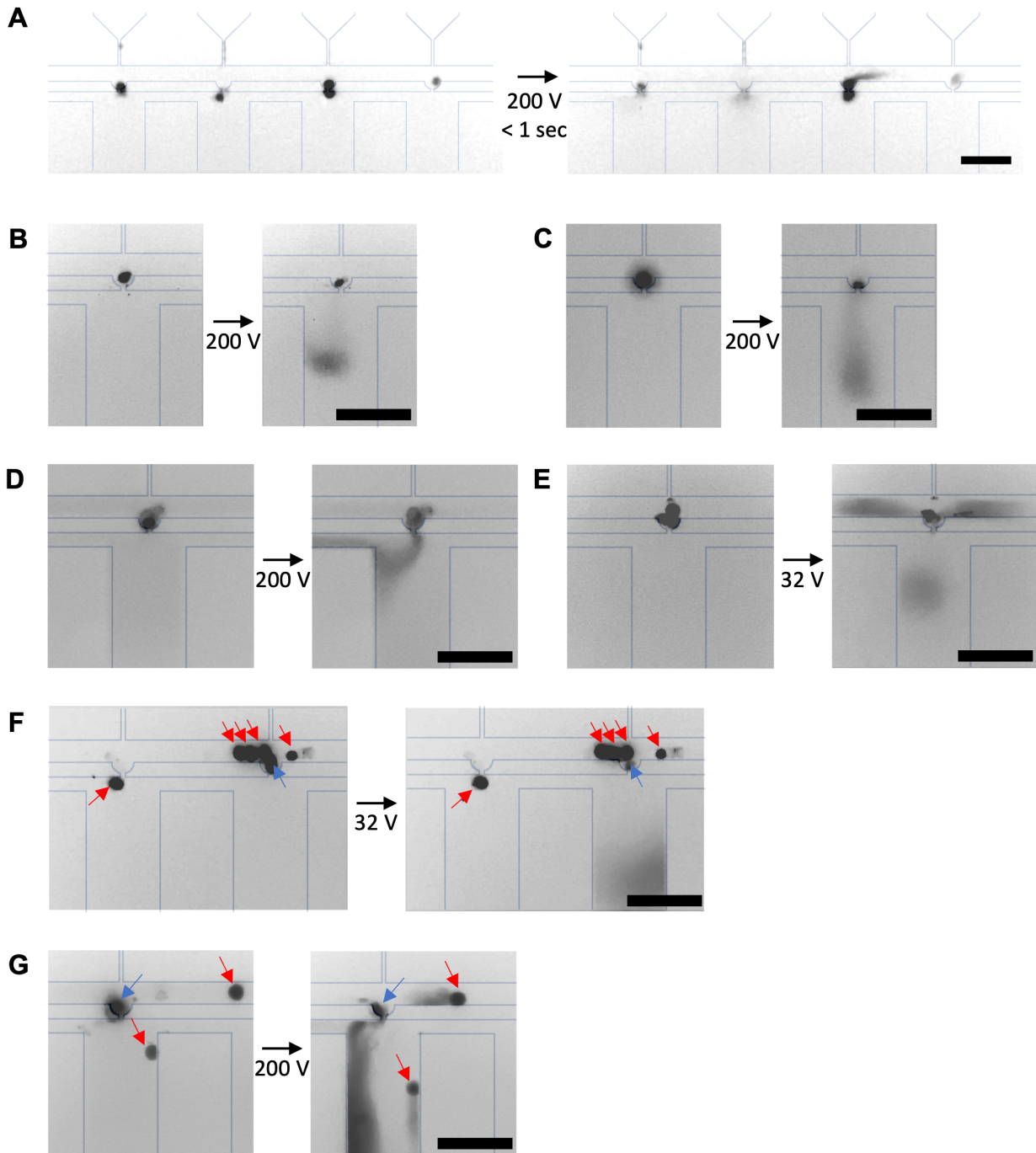


Figure 5.7: Variability in electrical cell lysis behavior in hydrodynamic cell traps. (A) Simultaneous cell lysis of 4 cells (cell suspension: MCF7-GFP, 0.5 million cells/mL, 0% agarose). (B-C) Cell lysis and injection of cell contents into microchannel. (B) Cell suspension: MCF7-GFP, 0.5 million cells/mL, 0% agarose. (C) Cell suspension: MCF7-GFP, 0.5 million cells/mL, 1% agarose. (D-E) Cell lysis and injection of cell contents into microchannel with cross-talk into neighboring microchannels. (D) Cell suspension: MCF7-GFP, 0.5 million cells/mL, 0% agarose. (E) Cell suspension: K562-LifeAct-GFP, 0.5 million cells/mL, 1% agarose). (F-G) Blue arrows point to cells expected to lyse and red arrows point to cells not expected to lyse. (F) Cell suspension: K562-LifeAct-GFP, 0.5 million cells/mL, 1% agarose. (G) Cell suspension: MCF7-GFP, 0.5 million cells/mL, 1% agarose. Micrographs have the same acquisition settings, brightness, and contrast within each panel, but not between panels for better visualization. Scale bar is 100 μm for all.

distance). Another potential strategy could be to introduce a non-conductive barrier in between microchannels after hydrodynamic cell trapping is complete (i.e., by the use of PDMS valves[42]).

We next sought to evaluate whether simulations (Figure 5.6) accurately described the cell lysis behavior in our device. As shown in Figure 5.7F, an applied electric potential of 32 V caused only the cells in contact with the trap gap (blue arrow) to undergo cell lysis, while cells not in contact with the trap gap (red arrows) did not undergo electrical cell lysis. On the other hand, an applied electric potential of 200 V caused all cells to lyse, even if not in contact with the trap gap (Figure 5.7G). This result is not unexpected as the minimum electric field strength we calculated in the cell trapping region for 200 V is $\sim 10^4$ V/m, which is an electric field strength capable of irreversible electroporation of mammalian cells[39]. While more controlled analysis of the cell lysis behavior is needed, these preliminary results point to the need to optimize the applied electric potential for both cell lysis and downstream electrophoresis, as the electric field strength will have effects on both protein state[43, 44] and protein separation resolution[45].

After electrical cell lysis, cell contents, including proteins, inject into the microchannel via electrophoresis. The PA gel in the separation channel serves as a sieving matrix to resolve proteins based on molecular mass and charge. A time lapse of migration of GFP under an electric field is presented in Figure 5.8. Importantly, the GFP maintains its fluorescence after electrical cell lysis and electrophoresis, indicating that GFP maintains its tertiary structure in our device, since GFP derives its fluorescence from its beta barrel structure protecting an internal chromophore[46]. Since GFP remains non-denatured, we hypothesize that electrical cell lysis is an appropriate cell lysis technique for native protein gel electrophoresis.

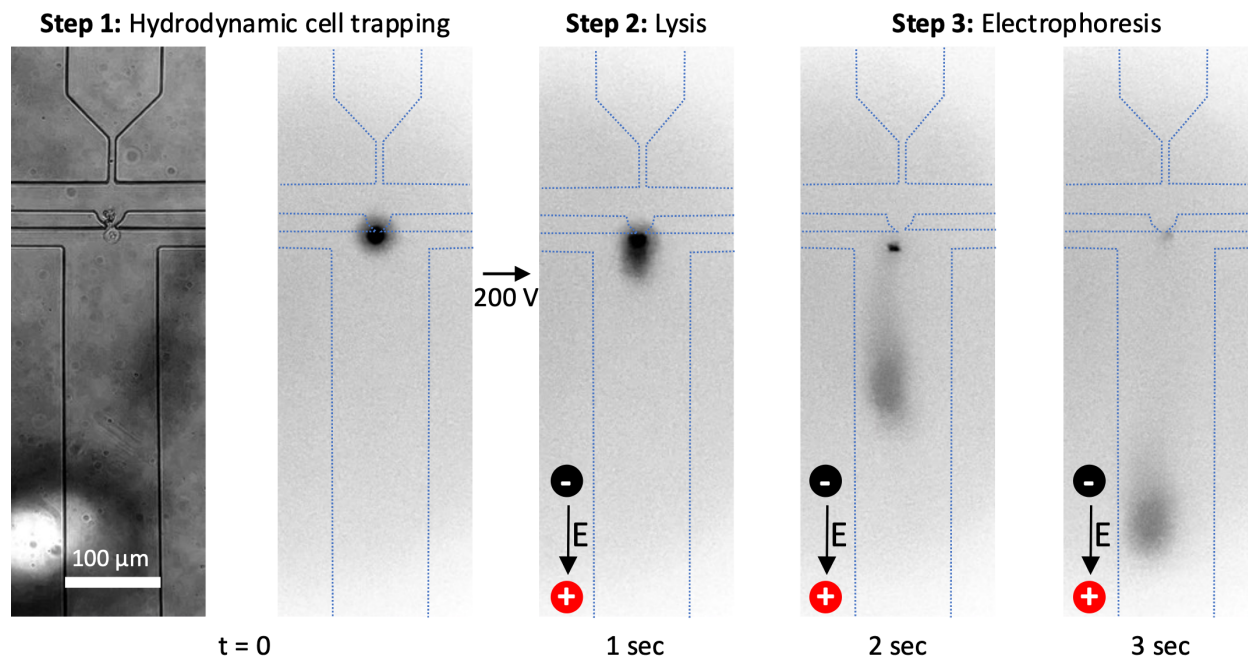


Figure 5.8: Time lapse of electrical lysis and electrophoresis after hydrodynamic trapping of GFP-expressing MCF7 cell.

5.5 Conclusions

In this chapter, we have presented proof-of-concept of a novel microfluidic device combining hydrodynamic cell trapping and electrical cell lysis for single-cell electrophoresis. The hydrodynamic trapping allows for positioning of cells ($\sim 1\%$ cell settling efficiency), while electrical lysis allows for the disruption of cell membranes, facilitating the release of intact biomolecules for native electrophoresis of cell lysate. While we provide a demonstration of enclosed scEP in this study, there remain substantial challenges for full integration of scEP with an enclosed microfluidic format. Key improvements to the present device include improving single-cell settling efficiency, maintaining gel integrity during hydrodynamic cell trapping, and eliminating cross-talk between microchannels during electrical cell lysis. Future research should be particularly mindful of the potential pitfalls of integrating hydrodynamic flow with delicate hydrogel membranes, which exacerbate the leaking phenomenon not uncommon in microfluidics[47]. Additionally, the electrophoretic cross-talk should be carefully addressed, potentially through re-design of the device to separate adjacent cell traps using PDMS valves[42] after hydrodynamic cell trapping but before electrical lysis.

To add protein identification and quantification capabilities to the enclosed scEP device presented in this chapter, the proteins could be immobilized in the PA gel and the PDMS

could be delaminated from the glass slide for immunostaining of the PA gel, as previously described[48]. Moreover, the enclosed design makes the device presented here compatible with other PDMS-based microfluidic devices, facilitating the prepending of a cell sorting[49] or cell measurement[50] assay to single-cell electrophoresis. In summary, our study underscores the significance of integrating hydrodynamic trapping and electrical lysis for single-cell analysis, which could add to the arsenal of tools to investigate cellular heterogeneity at the individual cell level.

References

- (1) Li, M.; Zuo, J.; Yang, K.; Wang, P.; Zhou, S. *Mass Spectrometry Reviews*, *n/a*, 1–22.
- (2) *Nature Methods* **2023**, *20*, 317–318.
- (3) Specht, H.; Slavov, N. *Journal of Proteome Research* **2018**, *17*, 2565–2571.
- (4) Levy, E.; Slavov, N. *Essays in Biochemistry* **2018**, *62*, 595–605.
- (5) Hughes, A. J.; Spelke, D. P.; Xu, Z.; Kang, C.-C.; Schaffer, D. V.; Herr, A. E. *Nature Methods* **2014**, *11*, 749–755.
- (6) Kang, C.-C.; Yamauchi, K. A.; Vlassakis, J.; Sinkala, E.; Duncombe, T. A.; Herr, A. E. *Nature Protocols* **2016**, *11*, 1508–1530.
- (7) Tentori, A. M.; Yamauchi, K. A.; Herr, A. E. *Angewandte Chemie International Edition* **2016**, *55*, 12431–12435.
- (8) Kang, C.-C.; Ward, T. M.; Bockhorn, J.; Schiffman, C.; Huang, H.; Pegram, M. D.; Herr, A. E. *npj Precision Oncology* **2018**, *2*, 1–10.
- (9) Kim, J. J.; Liang, W.; Kang, C.-C.; Pegram, M. D.; Herr, A. E. *PLOS ONE* **2021**, *16*, e0254783.
- (10) Hansen, L. L.; Lomeli, G.; Vlassakis, J.; Herr, A. E. In *Single Cell ‘Omics of Neuronal Cells*, Sweedler, J. V., Eberwine, J., Fraser, S. E., Eds.; Neuromethods; Springer US: New York, NY, 2022, pp 165–192.
- (11) Grist, S. M.; Mourdoukoutas, A. P.; Herr, A. E. *Nature Communications* **2020**, *11*, 6237.
- (12) Tentori, A. M.; Hughes, A. J.; Herr, A. E. *Analytical Chemistry* **2013**, *85*, 4538–4545.
- (13) Jung, B.; Bharadwaj, R.; Santiago, J. G. *Analytical Chemistry* **2006**, *78*, 2319–2327.
- (14) Kim, J. J.; Sinkala, E.; Herr, A. E. *Lab on a Chip* **2017**, *17*, 855–863.
- (15) Rosàs-Canyelles, E.; Modzelewski, A. J.; Geldert, A.; He, L.; Herr, A. E. *Science Advances* **2020**, *6*, eaay1751–eaay1751.
- (16) Narayanamurthy, V.; Nagarajan, S.; Khan, A. Y. F.; Samsuri, F.; M. Sridhar, T. *Analytical Methods* **2017**, *9*, 3751–3772.

- (17) Luan, Q.; Macaraniag, C.; Zhou, J.; Papautsky, I. *Biomicrofluidics* **2020**, *14*, 031502.
- (18) Tan, W.-H.; Takeuchi, S. *Proceedings of the National Academy of Sciences* **2007**, *104*, 1146–1151.
- (19) Shehadul Islam, M.; Aryasomayajula, A.; Selvaganapathy, P. R. *Micromachines* **2017**, *8*, 83.
- (20) Man Lee, L.; P. Liu, A. *Lab on a Chip* **2015**, *15*, 264–273.
- (21) Lawrenz, A.; Nason, F.; Cooper-White, J. J. *Biomicrofluidics* **2012**, *6*, 024112–024112–17.
- (22) Frimat, J.-P.; Becker, M.; Chiang, Y.-Y.; Marggraf, U.; Janasek, D.; G. Hengstler, J.; Franzke, J.; West, J. *Lab on a Chip* **2011**, *11*, 231–237.
- (23) Kobel, S.; Valero, A.; Latt, J.; Renaud, P.; Lutolf, M. *Lab on a Chip* **2010**, *10*, 857–863.
- (24) Tang, Y.; Shi, J.; Li, S.; Wang, L.; Cayre, Y. E.; Chen, Y. *Scientific Reports* **2014**, *4*, 6052.
- (25) Li, Y.; Motschman, J. D.; Kelly, S. T.; Yellen, B. B. *Analytical Chemistry* **2020**, *92*, 2794–2801.
- (26) Deng, B.; Li, X. F.; Chen, D. Y.; You, L. D.; Wang, J. B.; Chen, J. *The Scientific World Journal* **2014**, *2014*, e929163.
- (27) Yezek, L. P.; van Leeuwen, H. P. *Journal of Colloid and Interface Science* **2004**, *278*, 243–250.
- (28) Peters, A. J.; Zhang, H.; Davison, W. *Analytica Chimica Acta* **2003**, *478*, 237–244.
- (29) Tse, J. R.; Engler, A. J. *Current Protocols in Cell Biology* **2010**, *47*, 10.16.1–10.16.16.
- (30) Chai, H.; Feng, Y.; Liang, F.; Wang, W. *Lab on a Chip* **2021**, *21*, 2486–2494.
- (31) Brouzes, E. In *Single-Cell Analysis: Methods and Protocols*, Lindström, S., Andersson-Svahn, H., Eds.; Methods in Molecular Biology; Humana Press: Totowa, NJ, 2012, pp 105–139.
- (32) Wang, X.; Phan, D. T. T.; Zhao, D.; George, S. C.; Hughes, C. C. W.; Lee, A. P. *Lab on a Chip* **2016**, *16*, 868–876.
- (33) Garcia, P. A.; Ge, Z.; Moran, J. L.; Buie, C. R. *Scientific Reports* **2016**, *6*, 21238.
- (34) Lee, S.-W.; Tai, Y.-C. *Sensors and Actuators A: Physical* **1999**, *73*, 74–79.
- (35) Lo, Y.-J.; Lei, U. *Micromachines* **2019**, *10*, 247.
- (36) Lee, D. W.; Cho, Y.-H. *Sensors and Actuators B: Chemical* **2007**, *124*, 84–89.
- (37) Hughes, A. J.; Lin, R. K. C.; Peehl, D. M.; Herr, A. E. *Proceedings of the National Academy of Sciences* **2012**, *109*, 5972–5977.

- (38) Tia, S. Q.; Brown, K.; Chen, D.; Herr, A. E. *Analytical Chemistry* **2013**, *85*, 2882–2890.
- (39) Munce, N. R.; Li, J.; Herman, P. R.; Lilge, L. *Analytical Chemistry* **2004**, *76*, 4983–4989.
- (40) Tonin, M.; Deschames, N.; Houdré, R. *Lab on a Chip* **2016**, *16*, 465–470.
- (41) Nowbahar, A.; Whitaker, K. A.; Schmitt, A. K.; Kuo, T.-C. *Energy & Fuels* **2017**, *31*, 10555–10565.
- (42) Thorsen, T.; Maerkl, S. J.; Quake, S. R. *Science* **2002**, *298*, 580–584.
- (43) Freedman, K. J.; Jürgens, M.; Prabhu, A.; Ahn, C. W.; Jemth, P.; Edel, J. B.; Kim, M. J. *Analytical Chemistry* **2011**, *83*, 5137–5144.
- (44) Hekstra, D. R.; White, K. I.; Socolich, M. A.; Henning, R. W.; Šrajcar, V.; Ranganathan, R. *Nature* **2016**, *540*, 400–405.
- (45) Heller, C. *ELECTROPHORESIS* **2000**, *21*, 593–602.
- (46) Chalfie, M.; Kain, S. R., *Green Fluorescent Protein: Properties, Applications and Protocols*; John Wiley & Sons: 2005.
- (47) Silverio, V.; Guha, S.; Keiser, A.; Natu, R.; Reyes, D. R.; van Heeren, H.; Verplanck, N.; Herbertson, L. H. *Frontiers in Bioengineering and Biotechnology* **2022**, *10*.
- (48) Abdel-Sayed, P.; Yamauchi, K. A.; Gerver, R. E.; Herr, A. E. *Analytical Chemistry* **2017**, *89*, 9643–9648.
- (49) Mazutis, L.; Gilbert, J.; Ung, W. L.; Weitz, D. A.; Griffiths, A. D.; Heyman, J. A. *Nature protocols* **2013**, *8*, 870–891.
- (50) Zhou, Y.; Basu, S.; Laue, E. D.; Seshia, A. A. *Biomedical Microdevices* **2016**, *18*, 56.

Chapter 6

Conclusions and Future Directions

In this dissertation, we developed tools and materials to advance single-cell proteoform analysis. We integrated single-cell immunoblotting (scIB) with multiplexed ion beam imaging (MIBI) and miniaturized immobilized pH gradient (IPG) isoelectric focusing in a PDMS-based device. Additionally, we fabricated a gradient pore-size hydrogel for 3D projection electrophoresis and demonstrated a proof-of-concept of combining hydrodynamic cell trapping with electrical lysis for single-cell protein electrophoresis in an enclosed microfluidic device.

Chapter 2 builds upon the previously published single-cell isoelectric focusing (scIEF) assay[1] and, for the first time, demonstrates multiplexed ion beam imaging of a single-cell immunoblot[2]. The scIEF assay has some avenues for improvement, including enhancing sensitivity (currently limited to proteins with $\sim 42,000$ copies or more[1]) and throughput (currently only 10 cells analyzed on a single scIEF chip with 2.5 hours of hands-on time per run[1, 3]). Compared to its counterpart, the single-cell western blot (scWB), scIEF lags in terms of throughput (scWB can perform thousands of single-cell separations on a single chip[4]). The scWB has only been demonstrated to separate proteoforms differing by 4 kDa[5]. However, many proteoforms differ by only a few Da (i.e., due to phosphorylation), making the scWB unsuitable for analysis of small post-translational modifications (PTMs). Enclosed microfluidic designs, such as the one presented in Chapter 5, may offer an avenue to increase the sensitivity and throughput of scIEF. Additionally, performing scIEF with an immobilized pH gradient gel, as presented in Chapter 3, could lead to a more robust pH gradient, allowing for longer focusing times before cathodic drift[6] degrades the separation.

One limitation of single-cell immunoblotting is that it is, by definition, an immunoassay. While the protein separation relaxes the need for proteoform-specific antibodies, antibodies are expensive, and high affinity antibodies are not available for all targets. Label-free protein assays, such as mass spectrometry, eliminate the need for antibodies and can achieve single-cell resolution[7–9]. However, current instruments lack the sensitivity to perform intact protein readout of single-cell electrophoresis due to the significantly higher protein sample dilution ($>3,000$ -fold) compared to intact cells. Nevertheless, further sensitivity improvements in mass spectrometry instruments may enable 2D electrophoresis of single cells, combining

isoelectric focusing in a hydrogel in the first dimension with mass spectrometry imaging (e.g., by matrix-assisted laser desorption/ionization) of intact proteins in the second dimension. This virtual 2D electrophoresis[10] could enhance multiplexing capability over current single-cell immunoblots, as single cells would produce 2D maps enabling the identification of proteoforms.

Finally, although single-cell immunoblotting has been predominantly applied to the analysis of proteoforms from cell cultures[1], tumors[11, 12], and other biological specimens[13] to gain insights into each sample's nature, the technique holds potential in the protein engineering field as well. Microfluidic tools for protein engineering have already seen commercial success at companies such as Berkeley Lights and AbCellera, which used a microfluidic platform to develop the first COVID-19 antibody therapeutic. However, current methods are largely blind to the PTM-state(s) of the proteins being produced during protein selection. The fundamental rule of directed evolution of proteins is “You get what you screen for,”[14] and single-cell immunoblotting could provide that PTM screen, enabling the engineering of chemically sophisticated proteins by purposefully tuning PTMs.

Ultimately, the single cell is the most basic form of life, yet it is more complex than any man-made machine. As our analytical tools become more sophisticated, we unravel this complexity that forms the basis of who we are.

References

- (1) Tentori, A. M.; Yamauchi, K. A.; Herr, A. E. *Angewandte Chemie International Edition* **2016**, *55*, 12431–12435.
- (2) Lomeli, G.; Bosse, M.; Bendall, S. C.; Angelo, M.; Herr, A. E. *Analytical Chemistry* **2021**, *93*, 8517–8525.
- (3) Hansen, L. L.; Lomeli, G.; Vlassakis, J.; Herr, A. E. In *Single Cell ‘Omics of Neuronal Cells*, Sweedler, J. V., Eberwine, J., Fraser, S. E., Eds.; Neuromethods; Springer US: New York, NY, 2022, pp 165–192.
- (4) Kang, C.-C.; Yamauchi, K. A.; Vlassakis, J.; Sinkala, E.; Duncombe, T. A.; Herr, A. E. *Nature Protocols* **2016**, *11*, 1508–1530.
- (5) Vlassakis, J.; Herr, A. E. *Analytical Chemistry* **2017**, *89*, 12787–12796.
- (6) Yamauchi, K. A.; Tentori, A. M.; Herr, A. E. *ELECTROPHORESIS* **2018**, *39*, 1040–1047.
- (7) Kempa, E. E.; Smith, C. A.; Li, X.; Bellina, B.; Richardson, K.; Pringle, S.; Galman, J. L.; Turner, N. J.; Barran, P. E. *Analytical Chemistry* **2020**, *92*, 12605–12612.
- (8) Budnik, B.; Levy, E.; Harmange, G.; Slavov, N. *Genome Biology* **2018**, *19*, 161.
- (9) Slavov, N. *Current Opinion in Chemical Biology* **2021**, *60*, 1–9.
- (10) Lohnes, K.; Quebbemann, N. R.; Liu, K.; Kobzeff, F.; Loo, J. A.; Ogorzalek Loo, R. R. *Methods* **2016**, *104*, 163–169.

- (11) Kang, C.-C.; Ward, T. M.; Bockhorn, J.; Schiffman, C.; Huang, H.; Pegram, M. D.; Herr, A. E. *npj Precision Oncology* **2018**, *2*, 1–10.
- (12) Kim, J. J.; Liang, W.; Kang, C.-C.; Pegram, M. D.; Herr, A. E. *PLOS ONE* **2021**, *16*, e0254783.
- (13) Rosàs-Canyelles, E.; Modzelewski, A. J.; Geldert, A.; He, L.; Herr, A. E. *Science Advances* **2020**, *6*, eaay1751–eaay1751.
- (14) Arnold, F. H. *Angewandte Chemie International Edition* **2019**, *58*, 14420–14426.